Stony Brook University

Structurally Integrated, Damage Tolerant Thermal Spray Coatings: Processing Effects on Surface and System Functionalities

A Dissertation Presented

by

Andrew Vackel

to

The Graduate School

in Partial Fulfillment of the

Requirements

for the Degree of

Doctor of Philosophy

in

Materials Science and Engineering

Stony Brook University

December 2015

Stony Brook University

The Graduate School

Andrew Vackel

We, the dissertation committee for the above candidate for the

Doctor of Philosophy degree, hereby recommend

acceptance of this dissertation.

Prof. Sanjay Sampath – Dissertation Advisor
Distinguished Professor, Materials Science and Engineering

Prof. Herbert Herman - Chairperson of Defense
Distinguished Professor Emeritus, Materials Science and Engineering

Prof. Curt Johnson
Adjunct Professor, Materials Science and Engineering

Prof. Toshio Nakamura
Professor, Department of Mechanical Engineering
Stony Brook University

This dissertation is accepted by the Graduate School

Charles Taber
Dean of the Graduate School

Abstract of the Dissertation

Structurally Integrated, Damage Tolerant Thermal Spray Coatings:

Processing Effects on Surface and System Functionalities

by

Andrew Vackel

Doctor of Philosophy

in

Materials Science and Engineering

Stony Brook University

2015

Thermal Spray (TS) coatings have seen extensive application as protective surfaces to enhance the service life of substrates prone to damage in their operating environment (wear, corrosion, heat etc.). With the advent of high velocity TS processes, the ability to deposit highly dense (>99%) metallic and cermet coatings has further enhanced the protective ability of these coatings. In addition to surface functionality, the influence of the coating application on the mechanical performance of a coated component is of great concern when such a component will experience either static or cyclic loading during service.

Using a process mapping methodology, the processing-property interplay between coating materials meant to provide damage tolerant surface or for structural restoration are explored in terms of relevant mechanical properties. Most importantly, the residual stresses inherent in TS deposited coatings are shown to play a significant role in the integrated mechanical performance of these coatings. Unique to high velocity TS processes is the ability to

produce compressive stresses within the deposit from the cold working induced by the high kinetic energy particles upon impact. The extent of these formation stresses are explored with different coating materials, as well as processing influence.

The ability of dense TS coatings to carry significant structural load and synergistically strengthen coated tensile specimens is demonstrated as a function of coating material, processing, and thickness. The sharing of load between the substrate and otherwise brittle coating enables higher loads before yield for the bi-material specimens, offering a methodology to improve the tensile performance of coated components for structural repair or multi-functionality (surface and structure).

The concern of cyclic fatigue damage in coated components is explored, since the majority of service application are designed for loading to be well below the yield point. The role of coating properties and residual stress, processing effects, and substrate choice on the changes in specimen fatigue life is explored, with a mechanism for failure postulated.

Table of Contents

List of Figures

List of Tables

Acknowledgments

I would like to acknowledge the support of the many people I have worked and interacted with over the years that helped the formation of this dissertation

First and foremost, I would like to acknowledge my defense committee – Prof. Sanjay Sampath, Prof. Herbert Herman, Prof. Curt Johnson, and Prof. Toshio Nakamura – for taking the time to read and note my dissertation, as well as all the time that they have each spent with me these past years. A particular thank you to Prof. Herman who graciously helped me edit this work while retired from the lab and Prof. Johnson for making the journey from Niskayuna to take part in my defense committee. The countless conversations and discussions with each of them has been instrumental in the development of my academic and scientific abilities, which I am sure will continue to shape and contribute to my future career for years to come.

I would also like to acknowledge the funding support I have received and used for this work, with support from Messier-Bugatti-Dowty - a division of Safran Corporation (sponsors Roger Eybel and Dr. Francis Monerie-Moulin), the Transportation Research Board of the National Academy of Sciences under the Innovations Deserving Exploratory Analysis (IDEA) program managed by Dr. I. Jawed (NCHRP IDEA 155), and the general support to the Center for Thermal Spray Research through Industrial Consortium for Thermal Spray Program. In addition, there are many industrial partners and colleagues through the Consortium whom I am indebted to for their time, expertise, and technical support including Dave Lee (Kennametal-Stellite), Dr. Dan Sordelet (Caterpillar), Jon Gutleber (Oerlikon-Metco), Marc Froning and Dr. Arash Ghabchi (Boeing Company), and Bob Palladino (Hayden Corporation). I would also like to thank the international collaborators of the Center for Thermal Spray Research including Dr. Tomi Suhonen and Dr. Tommi Varris of VTT Finland, Dr. Per Nylen and Steffan Bjorkland of PTC

Sweden, Ing. Radek Musalek, Ph.D. of IPP Czech Republic, and Ing. Ondrej Kovarik, Ph.D. of Czech Technical University. Additional thanks goes to Dr. Phuong Vo and Dr. Rogerio Lima of CNRC Canada for the collaborative work shown in Section 4.3.2.3 and Prof. Dr.–Ing. Matthias Oechsner, Prof Dr.-Ing. Britta Pyttel, and Dipl-Ing. Norbert Schneider of Technical University at Darmstadt for the fatigue testing in Section 5.3.1.1.

Finally, I would like to acknowledge the support of the various lab-mates and co-workers, both current and former, I have learned from, worked with, and have aided both in producing this work and the comradery of working together in the Center for Thermal Spray Research including Dr. Gopal Dwivedi, Dr. Alfredo Valarezo, Vaishak Viswanathan, Dr. Katherine Flynn, Dr. Ram Seshardi, Dr. Yikai Chen, Dr. Dimitris Zois, Dr. Biran Choi, Chris Jensen, Travis Wentz, Anthony Mariano, Sal Marino, Riston Rocchio, Gregory Smith, Hwasoo Lee, Dr. Su Jung Han, Albert Mariniec, Mike Resnick, Edward Gildersleeves, Ari Sagiv, Mike Inglima, Joey Nowak, Ayodeji Balogun, Glenn Banke, Steve Baader, Mike Flynn, Mike Miller, Murilo Lamana, Igor Felipe, and Sarena Romano, as well as Chandrani Roy, Debbi Michienzi, and Shaunte Smith from the Materials Science and Engineering Department at Stony Brook University.

1 Introduction

Background

In the design of an engineering component and the subsequent material selection process, there is often the need for multiple properties and characteristics that one single material may not be able to provide or be economically feasible. Thus arises the need for composite or multi-layered materials, incorporating two or more materials that synergistically combine to provide the necessary component properties enabling a desired performance. In cases where the surface properties of a component are not met by a material that is otherwise favorable in the design, coating overlays or diffusion based alterations may be used to provide the required surface properties. In the case of coatings or overlays, an independent material is mechanically or chemically bonded to the base substrate, allowing a diverse flexibility of coating and substrate combinations through processes such as plating, chemical or physical vapor deposition, sputtering, and thermal spray. Examples and classification of some coating technologies is shown in Figure 1-1. Thus, the proper coating of a component offers an effective and economical way to provide the surface characteristics needed to mitigate degradation mechanisms in service life (e.g., excessive heating, tribological wear, corrosion), provide a change in surface functionality from the substrate (e.g., thermal or electrical conductivity, wetting) or to repair/restore damaged substrates.

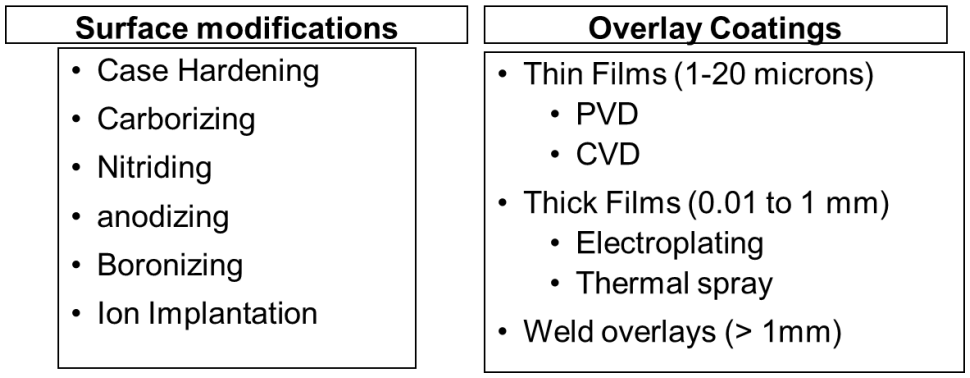

Figure 1-1 Examples of common coating and surface technologies

In choosing a coating process for particular surface characteristics, there is first a primary constraint of the deposition materials i.e., the desired coating materials must be able to be synthesized in the desired form onto a substrate. Secondary constraints, such as substrate temperature, line-of-sight processing, or thickness needs may also guide the designer's consideration of coating processes. In addition to technical factors, economic feasibility will also need to be taken into consideration when a coating process is considered. It is with the assessment of all these criteria wherein a coating process is selected for use surface modification of an engineering component.

Introduction to Thermal Spray

One such coating technology, Thermal Spray (TS), has found extensive use in several industrial sectors. The basis of TS coating processing is the use of a heat source, such as plasma, oxy-fuel combustion, or electric arc, to melt and propel feedstock material (commonly powder or wire) at high speeds towards a surface, where the molten droplets solidify and cool upon impact to mechanically bond with a substrate surface. Such deposited molten droplets are referred to as "splats", with the repeated deposition and buildup of these splats forming a thick coating. TS

coatings are normally in the thickness range of 10s to 100s of microns and in some cases yield free-standing forms centimeters thick [1]. With a large flexibility of commercially available feedstock materials and TS processes, a wide variety of TS coatings are used in industry, such as thermal barriers, electrical insulators, sacrificial and barrier type corrosion control, friction control/wear resistance, and repair of worn substrates. Thermal spray is used extensively in aerospace, power generation, heavy machinery, oil and gas, paper/pulp, and biomedical implants.

The Unique aspects and Classifications of TS

The basis of TS coating formation is through splat-by-splat bonding and buildup. Thus, the behavior of individual splats' impact and solidification from a molten state has a strong influence on the properties of the coating. The thermal and kinetic energy of these splats at the moment before impact, referred to as "particle state", is determined by the transfer of thermal and kinetic energy from the torch plume to the particles. Thus, the experience of the particle from introduction into a TS torch plume, acceleration and heating (with exposure to the surrounding atmosphere), and the deposition onto a surface are all factors in determining the coating microstructure, with varying degrees of control over the microstructure and resulting properties.

Over the past few decades, many different TS torches have become commercially available. These can be classified by the thermal source and general design. TS torch designs range from simple to complex, but more importantly have a large role in determining what particle states are achievable for a given feedstock. This is due to variations in plume enthalpy and velocity. An overview of TS processes and the expected relative thermal and kinetic energy expected is shown schematically in Figure 1-2

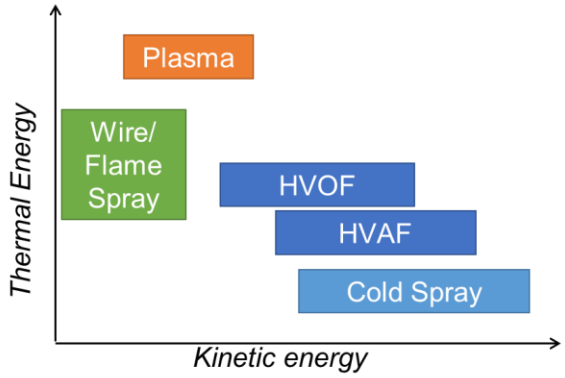

Figure 1-2 Schematic of typical Thermal and Kinetic energy for a given feedstock in different TS processes

High Velocity torch descriptions

High Velocity TS processes are well known to produce dense and well-adhered coatings and work on the principle of directing a combustion reaction through a de Laval type nozzle, producing plume exit gases at supersonic velocities [2]. A schematic of the relative particle states from the various high velocity TS process in shown in Figure 1-3.

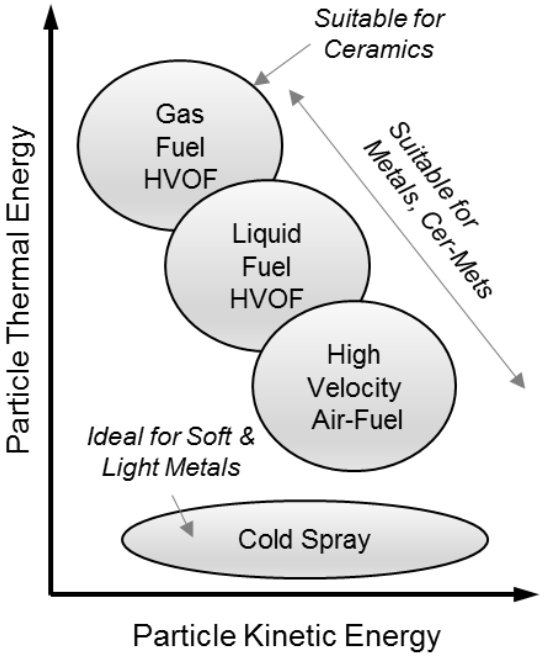

Figure 1-3 Thermal and kinetic energy process space for various types of high velocity TS processes and the commonly associated feedstock materials

Such processes include High Velocity Oxy-Fuel (HVOF) and High Velocity Air-Fuel (HVAF). HVOF torches can be further sub-divided into Gas Fuel (GF) and Liquid Fuel (LF), depending on the combusting fuel. Fuels for GF-HVOF commonly include hydrogen, propylene, or acetylene, whereas LF-HVOF generally uses kerosene. GF and LF-HVOF torches work on the same principle, yet the particle states of a feedstock are generally different due to these fuel differences and subsequent torch design. One key difference between GF and LF HVOF is the introduction of feedstock powder, shown in Figure 1-4.

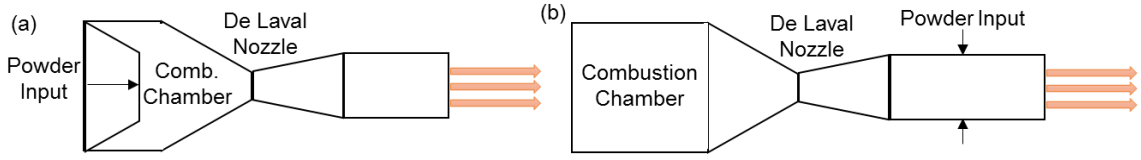

Figure 1-4 Powder Introduction relative to De Laval Nozzle for (a) GF-HVOF and (b) LF-HVOF

GF-HVOF torches generally introduce the powder axially into the plume before the nozzle's compression and expansion. LF-HVOF torches generally introduce the powder radially and after the combustion gas expansion, limiting thermal exposure. In addition to a shorter dwell time, the higher combustion pressure of the LF torches generally produces particles with higher velocities and lower temperature as compared to GF-HVOF. With HVAF the combustion temperature is reduced by the nitrogen present in the air, and further lowers the thermal exposure of the particles. Cold spray has cooler particle deposition by only using the expansion of highly compressed gas with no combustion (in general). Coating deposition relies principally on localized heating from adiabatic shearing upon particle impact for the bonding mechanism [3].

TS Stresses

As splats deposit and rapidly solidify on a substrate, the contraction of these droplets are constrained by the mechanical interlocking between the splat and typically roughened surfaces. This results in a net tensile stress within the splat, known as a "quenching stress". These stresses are a consequence of molten droplet deposition and are highly dependent on the thermal and kinetic energy of the particles, as well as deposition conditions (temperature, surface wettability) of the substrate. High stresses can be accommodated by micro-cracking in the case of more brittle materials, permanent deformation in more plastic materials, and interfacial sliding and de-bonding in both material types. With the invention of the high velocity deposition processes, the

high kinetic energy of the depositing particles impart solid-state cold working to the impacted surface [4]. This peening mechanism has the ability to produce compressive stresses within the impacted coating layer that can minimize, neutralize or even overcome the tensile stresses normally associated with the quenching of splats, as well as aid compaction and densification of the coating [5] The summation of the stresses from coating formation are termed *Deposition Stress* or *Evolving Stress* when only considering the coating formation during steady state deposition (i.e., not the first coating layer). In addition to the stresses involved in coating formation, thermal mismatch strains result from differences in the thermal expansion coefficients between the coating and substrate. This can induce thermal stresses as a coated part cools to ambient temperature after deposition termed *Thermal* Stress The summation of the quenching and peening stresses involved in coating formation and the thermal stress from cooling produces a residual stress profile within the coating, as well as a balancing stress within the substrate.

The ability to quantify the residual stresses of films and coatings was first demonstrated by Stoney in 1909 [6], where the radius of curvature of a coated beam is used to calculate the residual stress within the coating layer. The measurement of in-situ beam curvature during TS coating deposition was first demonstrated by Kuroda [7] and followed by detailed modeling of the layer-by-layer stress build-up process by Tsui and Clyne [8]. The technique was further expanded by Matijicek and Sampath [9] and correlated with X-ray and Neutron based techniques [10]. The ability to measure both the coating deposition and cooling gives insight into the coating formation stresses, as discussed above. This so called evolving stress, calculated by measuring the incremental change in curvature with deposition of each layer [11], quantifies the net contribution of peening and quenching stresses during coating deposition, which differ with feedstock, process selection, torch operating parameters, deposition rate, and substrate

temperature [12-14]. The use of such an in-situ beam curvature method and process knowledge offers the opportunity to tailor a desired residual stress. An example of curvature measurements for a sample of HVOF coating depositions is shown in Figure 1-5(a), along with the respective calculated stresses in Figure 1-5 (b)

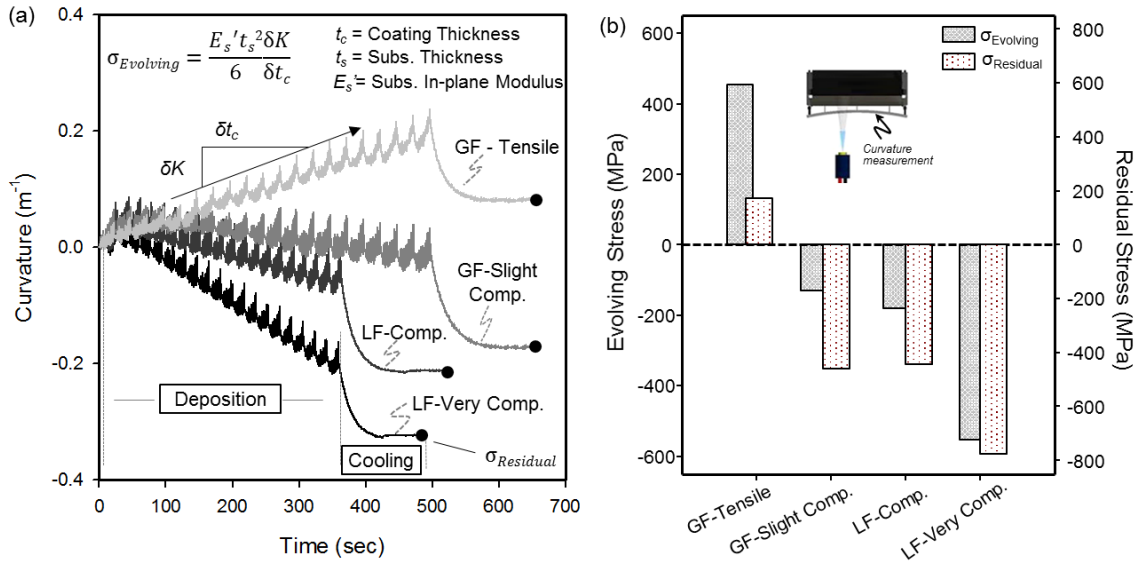

Figure 1-5 (a) Depiction of curvature evolution during layer-by-layer HVOF spray deposition of WC-CoCr measured using in situ beam displacement monitoring. The oscillations are due to rastering of the torch in front of the beam. The slope of the curvature-time graph is termed as evolving stress which is a result of particle solidification (quenching stress) and particle impact (peening stress). The $\sigma_{Evolving}$ value is obtained from Stoney formula. Detailed explanations of principles and operative mechanisms are available in the literature. The post-deposition cooling further incorporates thermal mismatch stresses between coating and substrate with the final curvature reporting the residual stress. (b) Shows values of evolving and residual stresses for the graphs in (a).

Feedstock Degradation

In addition to being able to produce dense and compressive coatings, the relatively short particle dwell times within the plume and surrounding atmosphere before impact allows high velocity TS processes to mitigate alterations occurring to the feedstock material in flight. This makes high

velocity TS processes more ideal for deposition of materials prone to oxidation or decarburizing, such as metals or carbide containing cermets, where possible phase changes considered undesirable for coating performance are significantly reduced compared to other TS processes. Further control of these feedstock alterations can be controlled by the selection of high velocity TS process, feedstock chemistry and morphology, and manipulation of torch parameters.

Role in Component Performance

It is the management of phase decomposition, tailorable formation stresses, high density, and bond strength that have allowed high velocity TS coatings to find a wide range of applications as wear resistant surfaces, corrosion barriers, and heavy machine element repairs. Such applications of metallic or cermet coatings include

-Oxidation-resistant bond coats for gas and aero turbines

-Wear-resistant surfaces for hydraulic cylinders and aero landing gears

-Friction-reducing surfaces for aero engine mating surfaces

-Corrosion and wear protection for paper rolls

-Repair of machine elements that have been degraded from prior services.

Most applications typically use these coatings in passive roles, where protection of the base substrate is achieved by the desired surface properties of the coating. The properties of these coatings, and thus performance, are highly dependent on coating processing, such as spray parameters and deposition conditions. As a consequence of TS processing, containing a large number of variables and lack of repeatability and robust processing, TS coatings are often delegated to a passive role and are not incorporated in the design of most prime reliant

engineering components. Along this theme, TS coatings for substrate repair have historically been considered primarily for cosmetic or dimensional repair, with little expectation in load sharing contribution.

Great strides in process control of TS hardware have been made over the last several decades. These advancements have enhanced the reliability of a highly stochastic process through feedstock control, automated process gas controls, and robotic torch manipulation. Additionally, TS process-specific sensors, such as in-flight particle state monitors and feedstock injection optimization, have added great value to process development, control and repeatability. Such controls and sensors have enabled TS to become a more reliable deposition process relative to the spray plume. However, the understanding of coating formation, properties, and performance are still emerging in the sensor and controller world. Such tools as in-situ beam curvature monitoring have provided a great deal of information for coating repeatability, as well as scientific insight into coating formation and residual stresses. As these tools and controls benefit TS processing, opportunities exist for enhanced component performance through scientific guidance.

In order to consider TS coatings as part of the prime reliant design of an engineering component, an understanding of the process-property-performance relationships within TS coatings is essential. Using a process map approach, the variations in particle and deposition states during the TS process and the resultant coating properties and performance can be mapped-out so that more rapid optimization of a specific coating function can be assessed. Such mapping requires the use of specialized tools for assessing the TS process, such as particle diagnostics sensors, and property measurements. Linking coating processing to properties to performance through

processes mapping has been successfully employed through previous studies [11, 13], where keys properties can be mapped out for a particular material and TS process.

Multifunctional Requirements

It is often the case that materials or coatings are required to be multi-functional, where many performance attributes are demanded from them. TS coatings are no exception. Though the coatings may be implemented for a single primary purpose, there are often numerous roles that a coating fulfills in protecting the substrate from undue damage during operation, or at the very least cause no significant detriments in other performance criteria. Influences such as chemical environment, mating surface, or thermal exposure will often drive the material selection for individual components. In the case of damage tolerant coatings, the system requirements are many, including wear resistance, corrosion protection, and fatigue endurance. These performance attributes will be uniquely affected by TS processing in ways highlighted in Figure 1-6, with subsequent discussion.

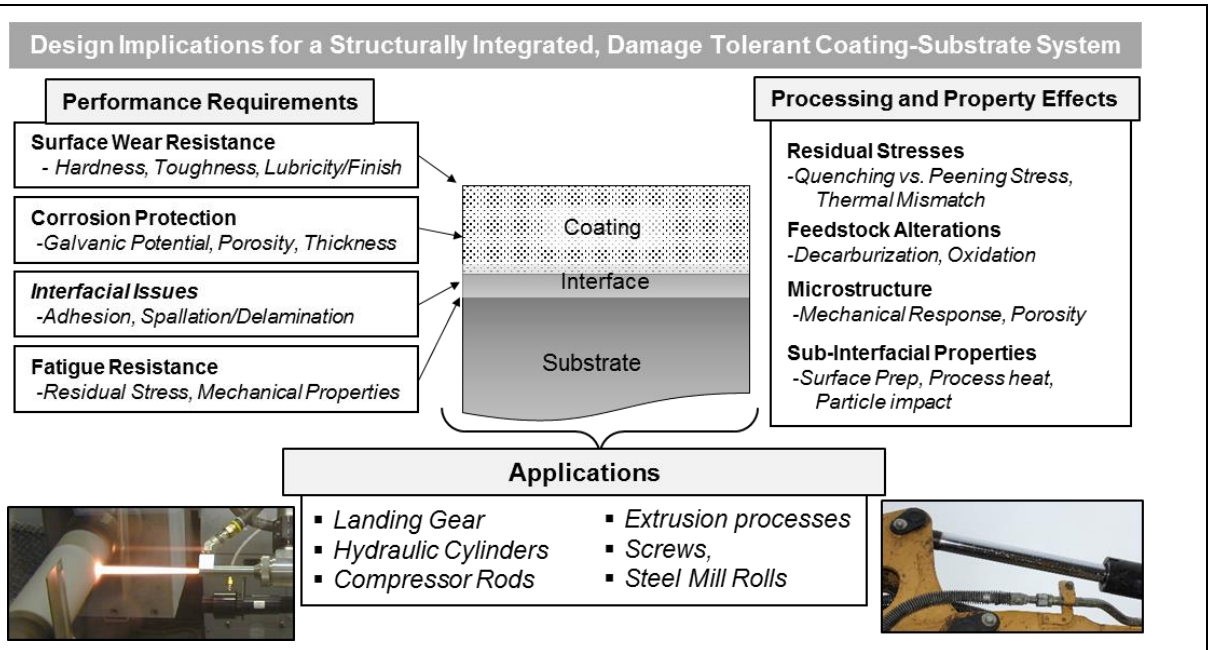

Figure 1-6 : Key performance and processing factors that affect design and manufacturing of structurally integrated coating systems.

Wear

One of the most widely used applications for high velocity TS coatings is for wear resistance. Depending on the component's design and purpose, wear scenarios can include three-body abrasion, erosion, impact, sliding/adhesive wear, fretting wear, cavitation, or contact fatigue. Numerous compositions and material types are employed for such surface protection, including WC-CoCr, WC-Co, CrC-NiCr, Tribaloys and other hard facing alloys, as well as ceramics such as Alumina or Chromia [15-20]. As discussed above, the properties of the TS deposited coating, such as residual stress, hardness, and toughness, will be different from that of the bulk materials [21]. This will require TS processing control and knowledge in order to produce the optimal coating surface for a wear scenario.

Corrosion

Similar to providing a wear protection surface, TS coatings for corrosion protection require the consideration of a combination of both the intrinsic property of the feedstock material and the TS processing influence on microstructure for proper coating design. With the proper feedstock composition for an operating environment, TS processing becomes the key factor in the performance of the coating. Typical corrosion control through TS coatings is achieved by providing a more active surface (Zinc, Al) than the substrate [22]. In the case of dense coatings produced via high velocity TS processes, corrosion protection is achieved by providing an adequate barrier between corrosive media and the substrate [23-26]. Such properties as residual stress, porosity, and thickness are critical for corrosion protection by preventing the infiltration of the electrolyte solution to the substrate. Additionally, galvanic coupling between the coating and substrate must be considered in order to prevent unexpected attack of the substrate due to the coating.

Fatigue/Load Endurance

In the case of load bearing components, such as aero landing gear, hydraulic cylinders, and drive shafts, the changes in static and cyclical mechanical behavior due to the processing and presence of a TS coating is critical. The variations in residual stresses and coating properties that arise from TS processing will have implications on the fatigue life of a coated component [27]. The superposition of applied stress and residual stress offer a different loading experience than for the uncoated substrate. In the case of component repair, having load recovery and structure stabilization with proper coating application offers considerable benefit to be gained in the remanufacture of expensive machine elements. Restored or enhanced mechanical properties vs the substrate material can be achieved through applied knowledge of the process-property relationships in TS coatings.

2 Statement of the problem

TS coatings are clearly able to provide life extension for many engineering components by providing surface protection to damage-prone surfaces or as a repair to restore damaged base materials. With the advent of high velocity deposition processes, the ability to synthesize nearly fully dense metallic and cermet coatings has been achieved, displaying excellent surface hardness for wear resistance applications and electrolyte barriers for corrosion protection. Many processing factors can influence the ability of these coatings to have to desired properties and performances. However, further complications arise from the many TS coating processes and feedstock choices available for different service environments. Various service environments often demand that the coating has a multi-functional role, thus making the processing critical.

When considering the prospect of treating the coating as a prime reliant contributor to the component's life and performance, rather than just life extension layer, one needs to tally up the key requirements that the TS coatings provide to a similar level of confidence as the structural component. Coating adhesion, cohesion, relevant properties (hardness, stiffness, and toughness), wear and corrosion resistance, and fatigue-life of the coated component are all important factors in design consideration. Process-induced effects on the substrate (e.g., formation and residual stresses, thermal input) are also important parameters that will depend on materials, process conditions and deposition conditions (e.g., cooling, surface speed). The last two decades have seen significant advancements in TS processing hardware and feedstock materials that have

enhanced the capability of the technology to meet the stringent design requirements for the proposed class of structurally integrated, damage tolerant coatings. In terms of process hardware advancements, the industry has developed a number of spray torches which allow manipulation of the particle streams, imparting a range of particle thermal and kinetic energies. Advanced mass flow based control consoles have enabled greater precision in managing/manipulating gas flows and feedstock input, enhancing the reproducibility and control of the spray stream. Integration of robotics has allowed enhanced process precision and application repeatability. A number of suppliers now offer various feedstock powders with well controlled particle size, composition, and morphology. These are necessary advances but not always sufficient to meet the goals of prime-reliant design and manufacturing of advanced coatings.

Perhaps the most important development in TS technology is enhanced scientific understanding along with user-friendly diagnostic and characterization sensors. Optical sensors that monitor thermal and kinetic energies of particle in-flight, including their spatial distribution, is now common place in most advanced facilities. Combined with sophisticated control systems, they allow day-to-day process repeatability. In recent years, the use of in-situ beam curvature measurements during deposition is prevalent in advanced laboratories and is being adopted in manufacturing. This provides real time measurement of coating formation dynamics through extraction of layer-by-layer stress evolution, as well as elastic properties of the coating. All of these sensors have enabled a greater insight into the processing-property-performance correlation, by allowing an understanding of the relations between hardware, feedstock selection, and the final coating properties and expected performance. Such a methodology, termed "process mapping", has been a useful tool for rapid optimization of coating properties and enables the design for damage-tolerant coatings in a systematic fashion as opposed to empirical-

based optimization. Coupling the demands for damage-tolerant surfaces with the need for the coating to be structurally integrated in a finished component make for a significant opportunity to produce optimized processing and coatings for high performance engineering components.

To date, there is limited understanding of the interplay between TS processing and the effective role of the coating's structural integration beyond that of a simple adhesion test. Fatigue testing of TS-coated components are often constrained to a single coating process and lack a mechanistic explanation of coating processing and the relevant effects on fatigue life. This lack of understanding could potential result in premature failure due to mechanical loading of the part instead of surface damage that the coating was put in place to protect. With advancements in process control and TS-specific sensors, there is the opportunity to develop the knowledge for optimizing TS coating structural integration, in conjunction with surface functionality. Therefore, this work is directed at identifying the key processing-property interactions of high velocity TS processing that allow for a multi-functional, structurally integrated coating to be produced. This will aid in yielding the desired surface characteristics as well as a neutral or beneficial effect on the static and cyclic load endurance of a coated component.

3 Process-Property-Performance relationships in Damage Tolerant Coatings: Surface Functionality

3.1 Introduction

The last two decades of thermal spray technology have seen the emergence of torches and processes, such as High Velocity Oxy-Fuel (HVOF), that are capable of imparting high kinetic energy to the spray particles. One of the most prominent applications of HVOF coatings is in aggressive wear environments, where materials such as WC-Co, WC-CoCr, and CrC-NiCr are deposited onto components, such as landing gear, hydraulic cylinders, gate valves, and paper rolls, in order to provide protection against wear/corrosion damage and imparting component life extension [28, 29]. In cases where only corrosion protection is required, barrier-type corrosion coatings of more noble metals are often deposited by HVOF, either directly for corrosion protection of the base material or for repair functions. Feedstock selection of such protective coatings are dependent upon the base material in order to avoid galvanic coupling of the coating and substrate, but a wide array of metallic feedstock is often suitable for such purposes, including Ni, Ni alloys, and Stainless Steels.

In addition to a large variety of feedstock chemistry, there exist different configurations of commercially available HVOF torches that are designed to uniquely facilitate thermal and kinetic energy transfer onto depositing particles, thus enabling large process windows,

particularly in terms of particle kinetic energies. Historically, the trend of high velocity torch design has pursued higher particle velocity. The general premise is that the higher the impact velocity, the greater the density of the coating, and thus yielding enhanced performance against wear and corrosion. One important design difference is the type of fuel used, such as gas fuel (GF) using Hydrogen or Propylene, or liquid fuel (LF), which is commonly Kerosene [30]. The thermal exposure and kinetic energy coupling of these two different types of HVOF torches can thus be significantly different based upon torch design. Other fuel variants are also possible, further expanding the potential application methods.

The key properties of interest with HVOF coatings (e.g., hardness, density, bond strength) are a function of coating chemistry and microstructure, both of which are processing sensitive [11]. In addition, besides the intrinsic hardness of WC-CoCr cermets or relative nobility of Nickel, the high kinetic energy contributes to a peening mechanism that can occur with HVOF particle impact. The depositing particles are thus able to work harden the previously deposited layer, imparting a compressive residual stress into the coating and also aid in coating densification [4]. This peening stress generation, unique to high velocity TS processes, can help neutralize or even over-compensate the quenching stress associated with rapid quenching and solidification of molten particles on the substrate [4, 11].

In order to examine the effect of torch selection, processing parameters, deposition conditions and feedstock selection of HVOF deposited coatings for wear and/or corrosion resistance, a process-mapping methodology is employed. The interactions between the torch plume and feedstock particles are measured using in-flight particle diagnostic sensors, allowing the construction of a first-order process map [11, 13, 31, 32]. Deliberate variations of in-flight particle states through operating parameters, as well as deposition conditions, will affect the

coating formation dynamics, including microstructure and coating formation stress, referred to as "evolving stress" [11, 13]. These, in turn, will facilitate the determination of the coating properties, such as hardness and modulus and related performance measures of wear and corrosion. The association between coating formation and subsequent properties are captured in the form of second-order process maps [11, 31, 32]. An illustration of the overall TS process chart is shown in Figure 3-1. In this chapter, a methodology for HVOF deposited WC-CoCr, CrC-NiCr, and Ni are presented, also allowing consideration of a range of thermal spray materials and processes. As will be shown, the availability of both in-flight process diagnostics and the monitoring of in-situ coating stresses enables these strategies to be used for coating optimization for specific applications [32]

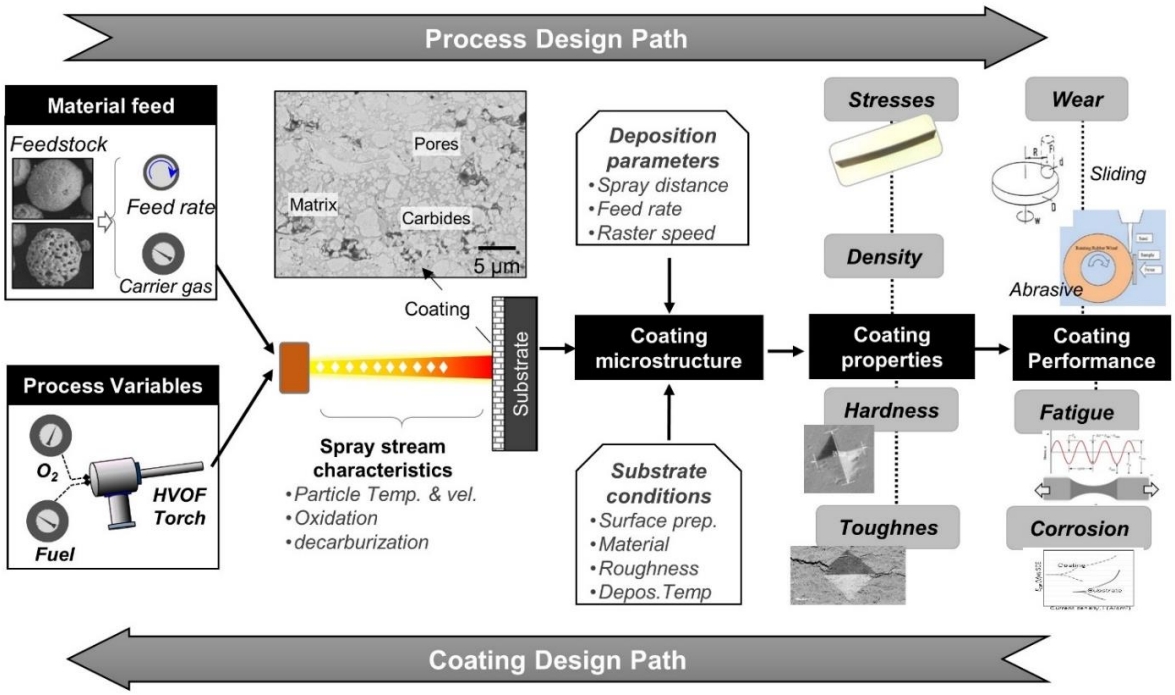

Figure 3-1 Illustrative flow chart depicting various process, property and performance elements that govern process and coating design properties.

3.2 Experimental Methods

3.2.1 Feedstock powders

Numerous feedstock powders including WC-CoCr, CrC-NiCr, and Nickel were sprayed under different conditions in a series of design-of-experiments. All powders are commercially available with composition and powder size listed in Table 3-1

Name	Composition	Size	Manufacturing Method	Carbide Size
JK120H	86WC 10Co 4Cr	-45+5μm	Agglomerated, Sintered, and Densified	1-10μm
SX178	86WC 10Co 4Cr	-44 +10μm	Densified Spherical	1-10μm
Amperit 556.059	86WC 10Co 4Cr	-30 +5μm	Agglomerated and Sintered	<1μm
WOKA 3652	86WC 10Co 4Cr	-45 +15μm	Spherical, Agglomerated and Sintered	1-10μm
SX195	75CrC 25NiCr	-44 +10μm	Densified Spherical	1-10μm
Ni 914-3	>99% Ni	-45 +16μm	Atomized	N/A

Table 3-1 Feedstock powders for Chapter 3

3.2.2 Spray Parameters

All coatings were sprayed with one of two torches- a Hydrogen-fueled Diamond Jet (DJ) 2260 by Oerlikon Metco, Westbury, NY, USA and a Kerosene-fueled JP 5220 (JP) by Praxair Surface Technologies, Indianapolis, IN, USA. All experiments were conducted using torch dedicated gas flow control systems and robotics for torch manipulation to aid in repeatable operation. A series of design-of-experiments (DOE) were used to provide variations in the spray stream.

3.2.2.1 DOE 1

The first design of experiment utilized a WC-CoCr powder (JK 120H, size range -45+5μm) from Kennametal Stellite, Goshen, IN, USA. For the DJ torch studies, an orthogonal Taguchi- 4 parameter and 3 level design-of-experiment was employed [33], varying the total gas flow, stoichiometric O_2/H_2 ratio (λ), spray distance, and feed rate. Air was used as the shroud gas (an internal design feature of the DJ torch).The O_2/H_2 flow ratio is calculated including combustion of the O_2 from the shroud air. The N_2 contribution from the shroud air is kept at a constant volumetric ratio of 0.23 N_2/total gas flow. For the JP torch studies, a single oxygen and

fuel parameter is used, with three varying spray distances. The Taguchi developed spray conditions for DJ and the conditions for JP are described in Table 3-2 and Table 3-3, respectively

Sample	Total Gas Flow [SLPM]	Stoich. Ratio λ	Spray Distance [mm]	Feed Rate [g/min]	Coating Thickness [µm]
D1	1158	0.81	254	30.4	230
D2	1158	0.90	229	38.0	290
D3	1158	0.99	203	45.6	310
D4	1286	0.81	229	45.6	260
D5	1286	0.90	203	30.4	220
D6	1286	0.99	254	38.0	270
D7	1415	0.81	203	38.0	220
D8	1415	0.90	254	45.6	250
D9	1415	0.99	229	30.4	200

Table 3-2 Taguchi design of experiment for Diamond Jet conditions with JK120H powder in DOE 1

Sample	O_2 Flow [SLPM]	Fuel Flow [SLPM]	Barrel [mm]	Comb Press [Bar]	Stoich. Ratio λ	Spray Distance [mm]	Feed Rate [g/min]	Coating Thickness [µm]
J1	944	0.41	152	7.23	1.12	279	65	70
J2	944	0.41	152	7.23	1.12	330	65	140
J3	944	0.41	152	7.23	1.12	381	65	150

Table 3-3 Spray conditions for JP torch with JK120H powder in DOE 1

In order to maintain similar coating thickness per pass, the increment between each stroke during spraying is 3mm and 5mm for Diamond Jet and JP, respectively, due to the difference in spot size and feed rate between the torches. A 1m/s raster speed is used for all spray runs.

3.2.2.2 DOE 2

Three feedstock powders were used for DOE 2, all of them WC-CoCr. An orthogonal Taguchi- 4 parameter and 3 level design-of-experiment was employed for both the DJ and JP torches. The parameters varied for the DJ torch were total volumetric gas flow, stoichiometric O_2/H_2 ratio (λ), spray distance, and the N_2/Total gas flow (from air). The parameters varied for the JP torch were combustion pressure, stoichiometric O_2/Fuel ratio (λ), spray distance, and barrel length. The levels for the parameters of the DJ and JP torch are shown in Table 3-4 and Table 3-5, respectively.

Parameter	Level 1	Level 2	Level 3
Total Flow [SCFH]	2500	2800	3100
O_2/Fuel Ratio	0.75	0.9	1.05
N_2/Total Flow	0.25	0.22	0.19
Spray Dist. [mm]	254	229	203

Table 3-4 Parameter levels for Taguchi test matrix for the DJ torch in DOE 2

Parameter	Level 1	Level 2	Level 3
Barrel Length [mm]	102	152	203
Comb. Press. [MPa]	0.52	0.62	0.72
O_2/Fuel Ratio	1.0	1.15	1.3
Spray Distance [mm]	381	330	279

Table 3-5 Parameter levels for Taguchi test matrix for the JP torch in DOE 2

Matching of the parameter order and effective torch condition is changed between feedstock powders in order to increase variability of spray parameters and is shown in Table 3-6 and Table 3-7 for DJ and JP, respectively.

Powder	P1	P2	P3	P4
SX 178	N_2/Total	S.D.	Total Flow	O_2/F
Amperit 556	S.D.	Total Flow	O_2/F	N_2/Total
WOKA 3652	Total Flow	O_2/F	N_2/Total	S.D.

Table 3-6 Parameter arrangement per each feed stock for the DJ spraying in DOE 2

Powder	P1	P2	P3	P4
SX 178	Comb Press	O_2/F	S.D.	Barrel
Amperit 556	Barrel	Comb Press	O_2/F	S.D.
WOKA 3652	S.D.	Barrel	Comb Press	O_2/F

Table 3-7 Parameter arrangement per each feed stock for the JP spraying in DOE 2

In an effort to maintain uniform coating application, the increment between each stroke during spraying is 3mm and 5mm for Diamond Jet and JP, respectively, due to the difference in spot size and feed rate between the torches. A 1m/s raster speed is used for all spray runs. A feed rate of 30g/min and 65g/min were used for the DJ and JP, respectively

For deposition condition studies, a single parameter for the JP was used, shown in Table 3-8

O_2 Flow [SLPM]	Fuel Flow [SLPM]	Barrel [mm]	Comb Press [MPa]	Stoich. Ratio λ	Spray Distance [mm]	Feed Rate [g/min]
944	0.41	152	0.72	1.12	330	65

Table 3-8 Center JP parameter used in testing deposition conditions in DOE 2

3.2.2.3 DOE 3

The third design of experiment utilized CrC-NiCr feedstock powder being sprayed by the LF-HVOF JP Torch. Torch conditions are shown in Table 3-9 with a feed rate of 65g/min and a spray distance of 16 inches. Raster speed for all conditions was 500mm/s. Parameters were designed to attempt three combustion pressure level and the range of stoichiometry the torch can provide.

Condition	Kerosene [lpm]	Oxygen [lpm]	O_2/Fuel	Chamber Pressure [Mpa]	Coating Thickness [µm]
1	.28	453	1.2 (O)	0.41 (L)	160
2	.25	519	1.0 (s)	0.39 (L)	260
3	.22	576	0.8 (F)	0.37 (L)	150
4	.35	564	1.3 (O)	0.52 (M)	210
5	.32	649	1.0 (S)	0.52 (M)	280
6	.27	722	0.8 (F)	0.50 (M)	330
7	.49	788	1.3 (O)	0.79 (H)	250
8	.44	909	1.0 (S)	0.77 (H)	260
9	.38	1010	0.8 (F)	0.72 (H)	240

Table 3-9 Test matrix for CrC-NiCr sprayed by the JP torch, where the ratios and levels of Fuel and Oxygen flow were changed in order to achieve plume stoichiometry of Oxygen Rich (O), Stoichiometric (S), and Fuel Rich (F). The resulting combustion pressures where classified as Low (L), Medium (M), and High (H)

3.2.2.4 DOE 4

The fourth experimental design utilized Nickel feedstock powder, with only two torch conditions shown in Table 3-10 for the LF-HVOF JP Torch. A Feed rate of 65g/min and a raster speed of 1000mm/s was used for coating deposition

Condition	Kerosene [L/hr]	Oxygen [SLPM]	O_2/Fuel	Chamber Pressure [MPa]
High	25	943	1.09	0.75
Low	19	849	1.28	0.63

Table 3-10 Test conditions used by the JP torch to spray Nickel in DOE 4

3.2.3 Particle State Measurement

In-flight particle properties (temperature and velocity) were measured using an Accuraspray G3 ™ (Tecnar Automation LTEE, St-Bruno, QC, Canada) with a low emission measurement sensor head. Measurements were made prior to coating deposition at the stand-off distance, with the average of more than 10 seconds of recorded data used for reported values. Particle state measurements for DOE 2 were taken at a reduced feed rate in an effort to conserve powder.

3.2.4 Coating Stress Analysis

Coatings were deposited onto 25.4 x 228.6 x 2.3 mm grit blasted low carbon steel substrates with concurrent monitoring of their curvature changes and substrate temperatures during deposition using the in-situ coating property (ICP) sensor [7, 13]. The details of the measurement procedure are provided in reference [12, 34]. Layer-by-layer stress evolution in the coatings are then calculated via Stoney's formula [6]. Evolving stress, defined as the stress during the formation of each layer, is calculated using the incremental curvature change for each

spray pass, after the substrate temperature reaches a steady state (i.e., after a few initial coating passes). The final residual stress is obtained using the net curvature change in the substrate at the end of the cooling [11, 12, 34, 35]. Details of the stress descriptions and the methodologies for their extraction are provided in References [7, 13, 34]. Further explanation of stress calculation from curvature is shown in Chapter 10

To define the terminology used with regards to coating stress measured by beam curvature:

Residual Stress: The calculated stress value using the *initial* and *final* curvature measurements of the beam using Stoney formula. It is assumed to be equivalent in-plane (x and y), with an assumption of no stress difference in the through thickness direction (z). The residual stress value contains two constituent parts, the Thermal and Deposition stress.

Thermal Stress: The calculated stress value using the curvature at the *beginning of cooling* (after spraying) to the *end of cooling*. This is the magnitude of in-plane stress the coating has due to the thermal mismatch between the coating and substrate as the specimen cools from the deposition to ambient temperature (assuming no delamination or spallation during cooling).

Deposition Stress: The calculated stress value using *initial* curvature and the curvature immediately *after spraying*. This curvature point is the same as the beginning of cooling for the thermal stress calculation. The deposition stress takes into account all of the formation stresses within the coating, including the first adhesion layer, quenching stresses from splat bonding, peening stress from high kinetic energy impact, and any stress relaxation that may occur in the coating during the deposition process.

Evolving Stress: This uses an adaptation of the Stoney formula where the change in curvature with coating deposition is used to calculate the evolving stress. It is similar in value to the

Deposition stress, but uses the steady state deposition regime of curvature change once the coating process has reached steady state i.e., excluding the adhesion and the passes prior to steady state temperature of the beam. The evolving stress examines the character of the layer by layer deposition of a particular coating process, with the summation of quenching stresses, peening stresses, and any stress relaxation.

3.2.5 Coating Characterization

3.2.5.1 Micrographs

Cross-sectional micrographs were obtained on metallographic polished coating cross-sections using a scanning electron microscope, Hitachi TM3000 (Angstrom Scientific Inc., Ramsey, NY, USA) under electron back-scattered diffraction mode.

3.2.5.2 X-Ray Diffraction

X-ray diffraction spectra for coatings and the feedstock powder are collected under ambient conditions, using Philips diffractometer type PW 1729 (Philips Analytical Systems, Mahwah, NJ, USA) at rate of 1.2 degree/minute.

3.2.5.3 Microhardness

Cross-sectional Vickers hardness of coatings was measured on their polished cross-sections at 0.3 Kg load with a 15 second hold period. Indent size was measured by optical microscopy. For each coating at least ten measurements were made and their average values are reported.

3.2.5.4 Micro-Indentation

Indentation modulus measurements were taken on the top surfaces of polished coatings using an instrumented indenter with a Berkovich tip (Micro-Materials Limited, Wrexham Technology Park, Wrexham, UK). Elastic recovery of the coating upon unloading was used to calculate the indentation modulus, as described by Oliver and Pharr [36]

3.2.6 Coating Performance

All coating surfaces were ground and polished, with a final polishing step using 1µm diamond solution for a mirror finish prior to all coating performance tests.

3.2.6.1 Abrasion Wear Testing

Abrasive wear studies were conducted using the standard ASTM G65 method on select coatings under a load of 5kg for the stated periods of time. Sample were weighed before and after testing to determine weight loss

3.2.6.2 Sliding Wear Testing

A 6.35mm diameter alumina ball was used for a pin on disk wear test, done in lab air. Surfaces were cleaned with alcohol and dried prior to testing. Load, tangential speed, and total distance for the wear tests are shown in Table 3-11

Load [N]	Distance [m]	Ang. Speed [mm/s]
10	700	49
20	630	44

Table 3-11 Sliding Wear test conditions for WC CoCr samples

3.2.6.3 Corrosion testing

Corrosion performance was evaluated on their polished surface using electro-chemical test setup (Gamry 3000 potentiostat, Warminster, PA, USA) in a 3.5 wt% neutral NaCl solution. For each specimen, the setup is stabilized for two hours to obtain an open circuit potential (OCP) with reference to a standard calomel electrode. The potentiodynamic measurements were then conducted with a -0.3 to +1V scan with reference to the OCP at 5 mV/sec scan rate. The corrosion performance were benchmarked against uncoated and polished carbon steel.

3.3 Results

3.3.1 WC-CoCr – Single Feedstock Process Map: A Case Study

3.3.1.1 Particle State Manipulation

The in-flight particle temperature and velocity measurements of the spray conditions of gas and liquid fuel HVOF for JK120H powder are shown in Figure 3-2 as a 1st order process map from DOE 1 and the conditions given in Table 3-2 and Table 3-3. As expected the two torches produce particle states that occupy different zones of the temperature and velocity map, with the gas fuel DJ torch occupying a generally higher particle temperature and lower particle velocity regime than that of the liquid fuel JP torch. Such temperature and velocity regimes for different torches have been reported before, and can be attributed to the differences in torch designs, particularly in the manner in which particles are injected into the plume. The gas fuel DJ has the powder introduced axially into the combustion chamber, prior to the convergent-divergent nozzle. This is used to achieve supersonic gas velocities in HVOF torches, which allows a longer dwell time to particles within the hot gases. The liquid fuel JP torch has the powder introduced radially after the convergent-divergent nozzle, where the hot gases have already expanded to supersonic speed, providing a more immediate acceleration of the particles and thus reducing the dwell time of the particles in the hot gas. The exit velocity of the combusted gases from the

respective torches also contribute to the differences in particle velocity as there is a momentum transfer from gases to particles.

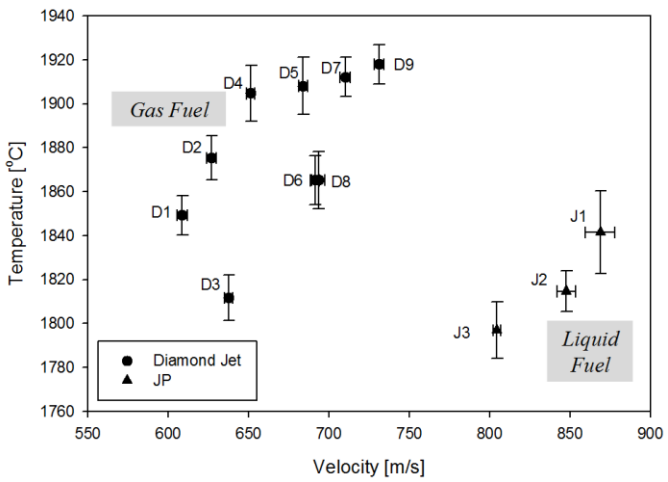

Figure 3-2 A particle temperature –velocity map for gas and liquid fuel sprayed WC-CoCr subjected to deliberate variations in process conditions identified in Table 3-2 and Table 3-3

Coating conditions for the DJ torch were selected in order to fit into a Taguchi design of the experimental matrix. Analysis of the particle temperature and velocity data for the coating conditions for the DJ is conducted using signal-to-noise Taguchi array analysis. The temperature and velocity values from this analysis for each spray parameter are shown in Figure 3-2 and Figure 3-3

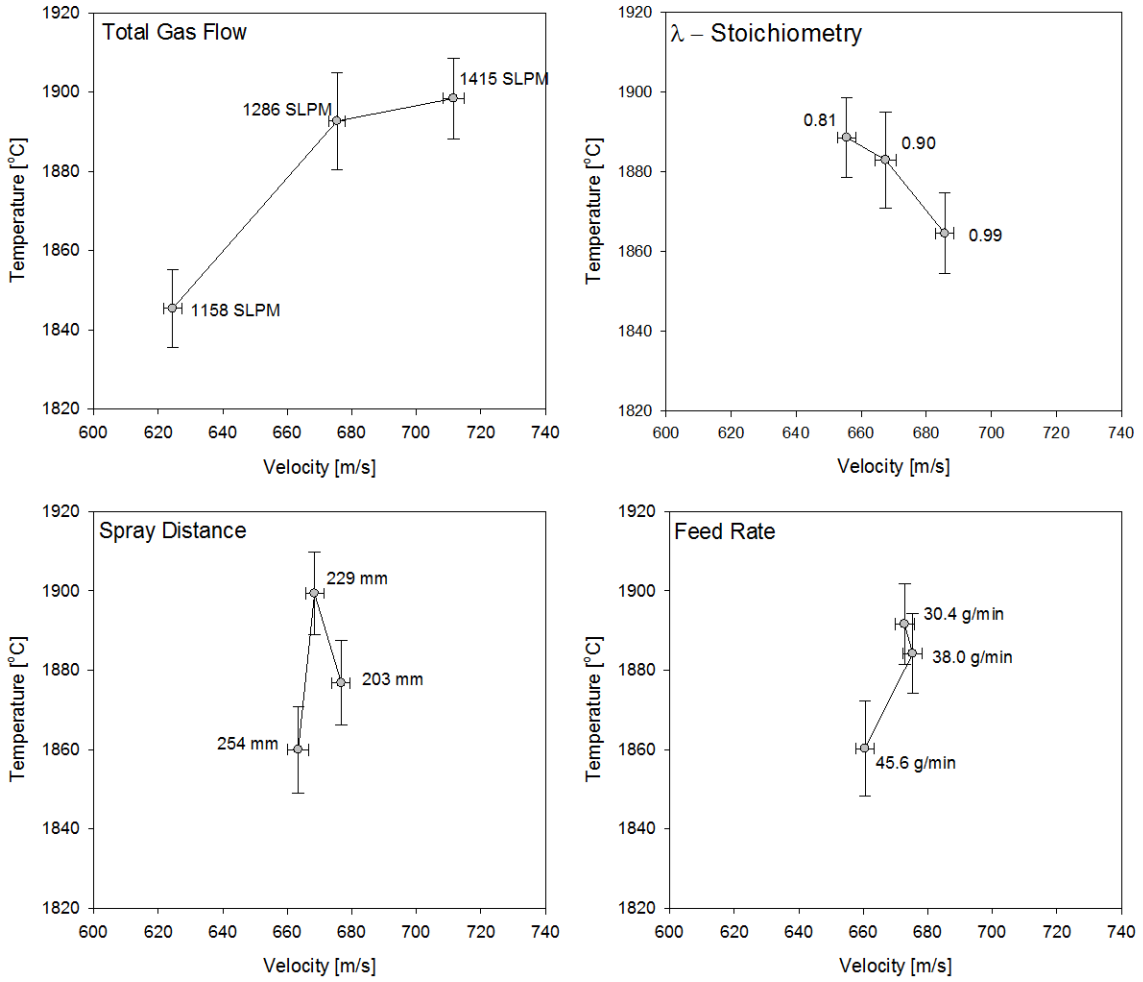

Figure 3-3 Signal to Noise ratio of Diamond Jet operating parameters of Total Gas Flow, Plume Stoichiometry (λ), Spray Distance, and Powder Feed Rate on particle temperature and velocity

Within these considered parameters for the DJ torch, it can be observed that the total gas flow has the widest relative influence on particle state, with higher flow producing hotter and faster particles. The stoichiometric O_2/H_2 ratio (λ) also has a large influence on particle states, with a more fuel rich flame having hotter and slower particles. Spray distance shows some variation with particle temperature, though there is relatively little influence on the particle velocity. On the other hand, powder feed rate shows minimal effect on particle state. However a

drop in both temperature and velocity at the highest feed rate level can be noticed, which is likely due to the quenching of the plume at those higher feed rates.

It should be noted that the Taguchi design of experiment used has limitations in describing the influence of parameter selection on particle state influence, since individual parameters are not varied independently of other parameters. Additionally, the extrapolation of parameter influence beyond the explored ranges cannot be used with a large degree of confidence. There exist more robust design of experiments that could be used for particle state exploration, but Taguchi was used for its limited use of resources as compared to other experimental designs.

The change in particle state for the JP-5220 conditions can be observed in Figure 3-2, where only the spray distance of the particles was changed. Unlike the spray distance behavior for the DJ's signal-to-noise ratio analysis, both particle temperature and velocity drop as the spray distance of the JP-5220 increases.

3.3.1.2 Feedstock phase changes/decomposition

The rapid melting of particles within a TS plume and quenching upon impact is a unique aspect of TS processing, where metastable feedstock material can be deposited with the proper process selection and operating parameters. The relatively short thermal dwell time of particles in high velocity TS processes offer an advantage over low velocity TS process having a longer thermal soaking time, such as plasma spray. The minimizing of phase changes and/or decomposition within the feedstock powder can be achieved and offers tighter control of phase-based defects that may have deleterious effects on the desired coating performance. Each

feedstock material is a unique case in the chemical changes it can be prone to, such as decarburization or oxidation, with direct implications for the processing parameters

WC is often considered a metastable phase, where with a high enough temperature (~450°C), the preferred carbide phase is W_2C. This phase is hard like WC, but is often associated with a higher degree of brittleness [37-40]. The excess carbon is generally thought it oxidize with excess oxygen in the spray plume and atmosphere. When WC is within a Co or CoCr matrix, as in the case of thermal spray powder, tertiary phases of W, C, Co, and Cr can form during thermal spraying as carbon may also diffuse into the matrix material [37-40], which may also be detrimental to intended wear performance of a WC-CoCr coating. Thus, the presence of W_2C and other unintended phases within a WC-CoCr coating are considered undesirable and are kept to a minimal level. The degree of WC to W_2C, referred to as decarburization, is easily observable in X-ray diffraction measurement of coating surfaces.

To illustrate the degree of decarburization of WC-CoCr associated with process selection and torch operating parameters, XRD measurements of select coatings using the torch operating parameters shown in Section 3.3.1.1 for both GF and LF HVOF were carried out. The results, as well as the calculated peak intensity ratio between W_2C and WC, are shown in Figure 3-4

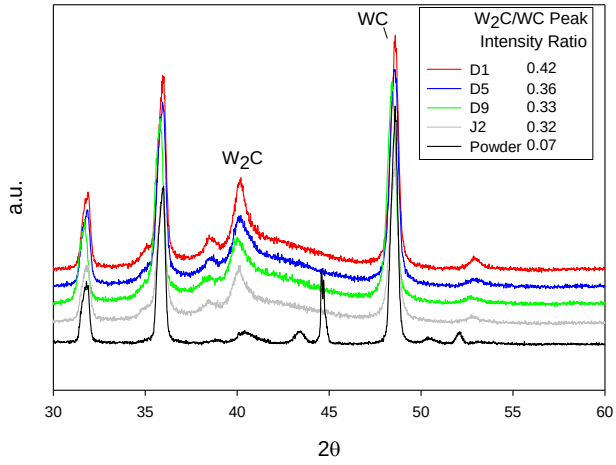

Figure 3-4 X-Ray diffraction patterns and the ratio of the W_2C and WC peak intensities of the as-received powder, D1, D5, D9 and J2 coatings

The relatively low level of W_2C detected in the as-received powder indicates that a significant degree of decarburization occurs during the particle's thermal soaking time. The GF DJ2600 torch, with generally higher particle temperatures, displayed a higher ratio of W_2C:WC in the sprayed coatings, while the LF JP5220 coating had a slightly lower degree of decarburization.

3.3.1.3 Process Induced Stress – Formation and Residual

The generation of residual stresses are inherent to the TS process, based upon with the rapid quenching of molten droplets which induce tensile stresses during deposit formation. As discussed in the Introduction, high velocity TS processes have the ability to induce cold working as particles with high kinetic energy impact the surface, inducing compressive stresses into the previously deposited layers. Thermal mismatch strain between the coating and substrate produces thermal stresses within the coating and substrate, with the ability to induce either compressive or tensile stresses within the coating, depending on the sign of the CTE difference.

The combination of all of these factors control the residual stress within TS coatings, with significant differences possible with TS process selection, feedstock, torch parameters, and deposition conditions.

The evolving stress as a coating is deposited gives an insight into the concurrent quenching and peening stresses that occur within high velocity TS coatings, offering a valuable tool for assessing coating integrity. Through the use of *in-situ* beam curvature monitoring, evolving and residual stresses can be calculated based on the Stoney formula for quantitative assessment of coating formation dynamics [6].

An example of such curvature measurement is shown in Figure 3-5, which are of the WC-CoCr coatings produced using the coating conditions in Table 3-2 with measured particle temperature and velocities shown in Figure 3-2

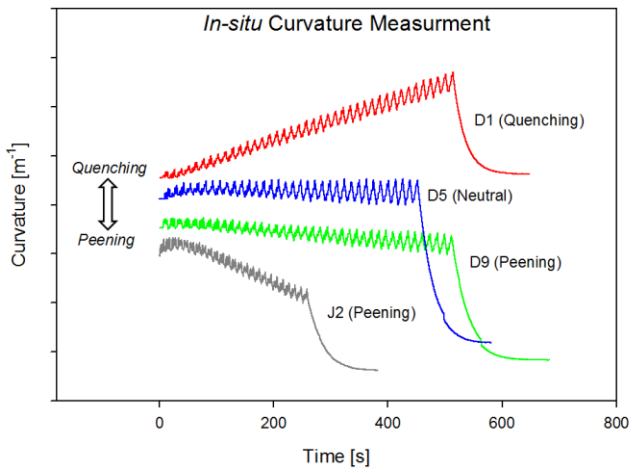

Figure 3-5 Examples of in-situ curvature evolution results during HVOF spraying for selected spray conditions exhibiting quenching, neutral, and peening evolving stress.

The change in curvature with coating addition clearly shows the nature of the evolving stress within these coatings, with an increase in curvature indicating net quenching stresses and a negative curvature growth indicating a net peening stress. The undulations within the coating deposition are from the torch rastering over the substrate. Curvature induced after coating deposition is a result of the thermal mismatch strain upon cooling, with all samples accumulating negative curvature (compressive stress) for the coating-substrate system of WC-CoCr on steel in Figure 3-5.

Using the measured velocity of the in-flight particles and a theoretical mass of the particles (using the d50 of the powder size distribution), the kinetic energy was calculated and plotted against the calculated evolving stress for all the DJ and JP conditions of JK120H and are shown in Figure 3-6

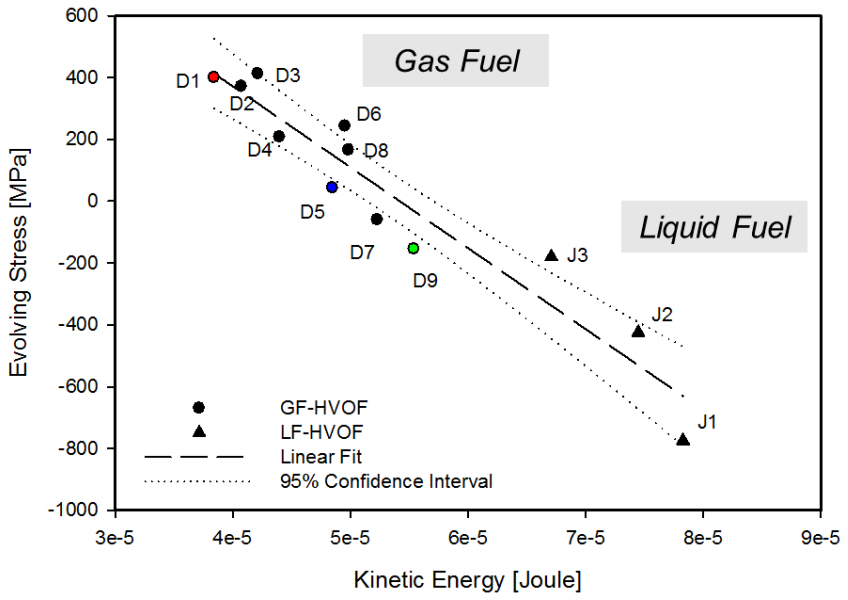

Figure 3-6 Correlation between evolving stress and particle kinetic energy for the various deposited samples indicating a linear trend (with confidence 95% confidence interval) between particle kinetic energy and the dominant formation stress

The results suggest a linear dependency between the two measured values with all the data nearly enveloped within a 95% confidence interval band. As anticipated, the greater the kinetic energy, the more compressive is the evolving stress. Coatings with larger thermal exposure (e.g., D1, D2, D3) experience greater thermal soaking due to the lower velocity (longer dwell time). These coatings result in quenching dominated tensile residual stress, classifying D1, D2 and D3 as low peening intensity conditions. Particles with lower temperatures (due to shorter dwell time at higher kinetic energies) display primarily a peening (compressive) contribution, and hence belong to high peening intensity conditions, such as all the JP conditions and D9 for DJ. The remarkable feature of this result is the ability of the HVOF process to modulate the deposition stresses through parametric control.

The representative coating microstructures from different regions of the peening intensity plot are shown in Figure 3-7, with insets of optical micrographs for measured porosity.

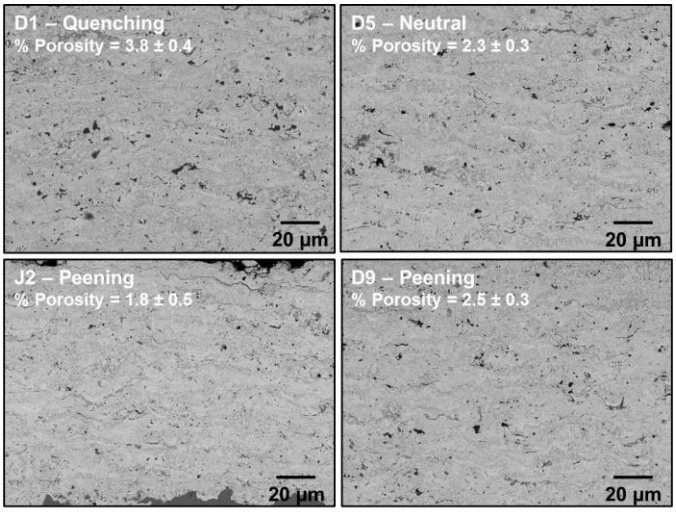

Figure 3-7 Representative scanning electron micrographs and apparent porosity values of the D9, D1, D5and J2 coatings, corresponding to the various stress states shown in Figure 3-5

These microstructures at first glance do not reveal a significant difference among the coatings. The JP coating shows lowest porosity attributed to the high impact velocities. The results of DJ samples are subtle but present a pattern. Here, the coatings produced at higher temperatures and higher velocities (e.g., D9) shows marginally lower porosity, while the coating produced under the quenching condition displays somewhat larger porosity. Both the neutral and compressive condition coating show similar apparent porosity.

3.3.1.4 Properties

As a damage-tolerant surface, where often the primary goal of coating application is to protect against undue component wear, WC-CoCr coating hardness has been considered a critical property. Though WC-CoCr has a high hardness as a bulk sintered material, splat-to-splat

bonding, phase decomposition/decarburization, and evolving and residual stresses all play a role in the hardness value of high velocity TS deposited WC-CoCr.

The measured Vickers hardness of the coatings produced by JK120H using the DJ2600 and JP5220 conditions in Table 3-2 and Table 3-3 are shown in Figure 3-8 with a graphical correlation between processing induced coating residual stress and hardness.

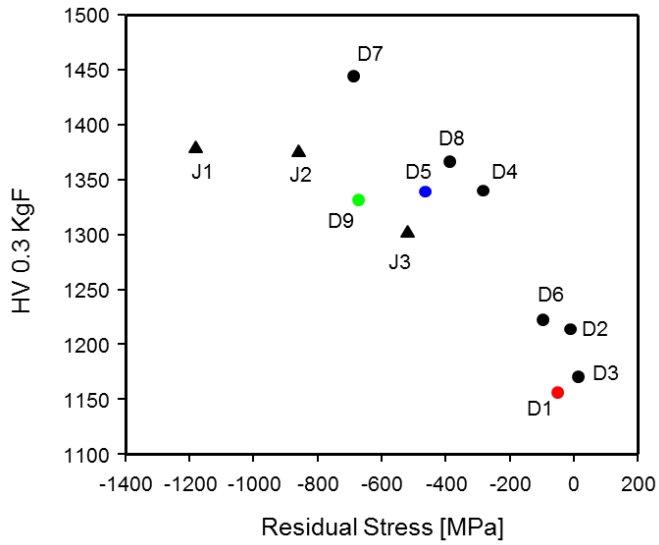

Figure 3-8 Graphical correlation between cross-section Vickers hardness of the various coatings and process induced residual stresses among the various coatings. The results generally point to increased hardness with increasing compressive residual stress state in the coatings.

The results of Figure 3-8 suggest that, in general, coatings with more compressive residual stresses exhibit higher hardness values. This is observed for both DJ and JP torches. This relationship can be explained based on the particle peening intensity and coatings residual stresses. The successive peening of the particles densifies the coating structure beneath and imparts the compressive residual stress. In addition, the peening phenomenon can work-harden the metal binder matrix, resulting in extrinsic hardening benefits. Particularly in WC-CoCr, other mechanisms may also contribute, for instance, the phenomena of decarburization which is likely

prevalent in the case of the DJ coatings. Formation of W_2C in the coating can potentially result in increased hardness due to the harder intermetallic phase as well as increased dissolution of carbon in the binder. This may be an explanation for higher hardness of D7 coating compared to D9, despite having similar residual stresses.

Additionally, it can be noted that the hardness values appear to reach a plateau at a hardness of around 1400 Hv. This can be attributed to the limitation of WC-CoCr's intrinsic hardness, and also to the processing limitations to provide a denser and more compressive coating. It is clear that interplay between microstructure, residual stress, and feedstock decarburization as a result of processing hardware and parameters have a tailorable effect on coating hardness.

3.3.1.5 Performance

As a predominantly wear resistant coating, the damage tolerance of WC-CoCr is of critical importance to the protection of a substrate that is incapable of withstanding harsh service environments. With variations in processing, the properties of TS sprayed WC-CoCr have considerable breadth. As would be expected, the wear performance of such coatings would vary as well. Abrasive wear performance was conducted on three of the DJ coatings with tensile (D1), neutral (D5) and compressive (D9) stress states from Figure 3-5 and are shown in Figure 3-9(a). The JP coatings from the same study were not sufficiently thick for testing and as such the data is not included.

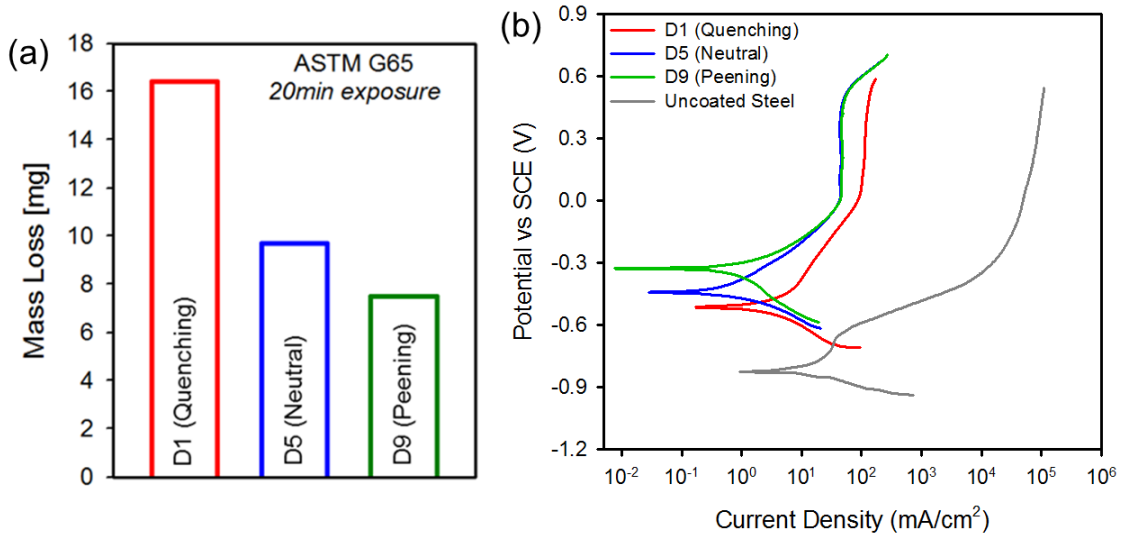

Figure 3-9 (a) Abrasive wear results obtained from the ASTM G65 test for three selected DJ coatings displaying tensile, neutral and compressive stress states. (b) Effect of evolving stress on coating performance evaluated via potentiodynamic polarization curves for three of the DJ samples displaying tensile, neutral and compressive stresses. Similar to the wear performance coatings subjected to greater degree of peening show improved corrosion protection.

Not surprisingly, the mass loss (or wear rate) correlates well with the evolving stress state and coating hardness. These results demonstrate not only the efficacy of HVOF process optimization for functional coating performance, but also the ability of controlling particle state and understanding stress evolution dynamics for efficient coating design and performance prediction.

Since many service environments for wear resistant coatings also have the potential for corrosion damage, whether from chemical or atmospheric moisture, corrosion response of these coatings are also of interest. Potentiodynamic corrosion test results of the selected DJ coatings (D1, D5 and D9) are shown in Figure 3-9(b). The selection criteria for these coatings were described in an earlier section and were of equivalent thickness. Figure 3-9(b) shows both the corrosion potential as well as the corrosion current density. Samples with higher corrosion

potential and lower current density represent superior corrosion resistance. All of the data is benchmarked against a plain carbon steel and indicates that all of the three WC-CoCr coatings provide a measure of protection to the steel.

Figure 3-9 also points to a strong correlation between the evolving stress state (peening vs quenching) and corrosion potential of the coatings. The corrosion potential (E_{corr}) D9 coatings was higher than D5 followed by D1 coatings, suggesting a systematic improvement in coatings' corrosion performance with evolving stress state changing from quenching to peening. These observations can be attributed to the larger peening and residual stresses present in coating D9, which result in a denser microstructure than the other two coatings. This densification would thus decrease the permeability of corrosive solution to penetrate deeper into the coating, possibly to the substrate. All of the coatings offer very good protection to the underlying steel substrate, with D9 offering the best protection, implying that complete penetration of solution to the substrate was not likely. The results again point to the coupling of process-property relationships in driving engineering performance of this class of HVOF spray coatings.

3.3.2 WC CoCr – Multiple Feedstocks, Torch Parameters, and Deposition conditions

3.3.2.1 Particle State Manipulation

With the wide variety of commercial feedstocks available for the same nominal composition of 86WC-10Co 4Cr, it is important to understand how different particle sizes and morphologies will interact across the parametric operating space of both GF and LF HVOF. The particle state of three different powders and a Taguchi arrangement of parameter selection for both the DJ2600 and JP5220 from Table 3-6 and Table 3-7 were measured, with the results shown in Figure 3-10

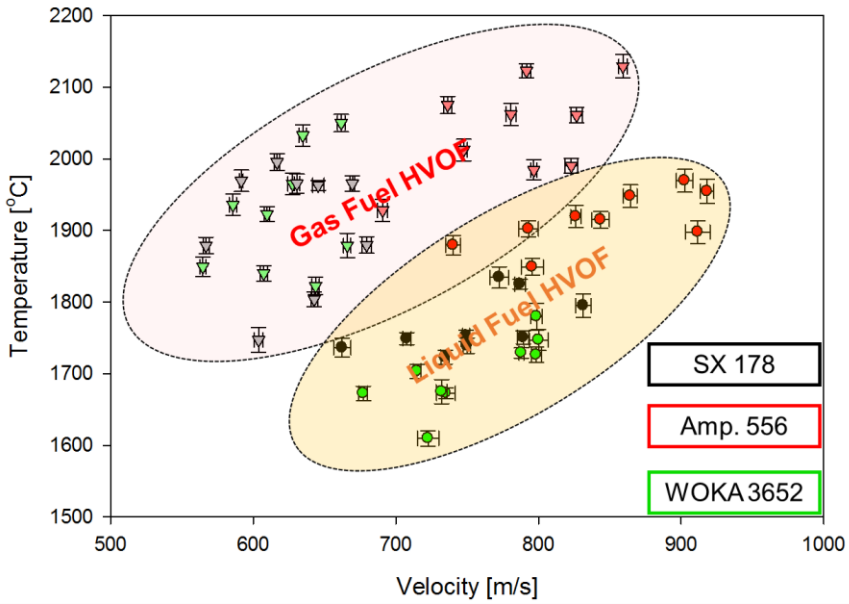

Figure 3-10 Measured particle velocity and temperature for three different WC CoCr powders sprayed by both GF and LF HVOF. SX178 and WOKA 3652 had similar particle size and WC grain size whereas Amperit 556 was a smaller particle size with finer WC grains.

Again, it is clear to see that the GF-HVOF DJ2600 produces a particle state with on average higher particle temperatures and lower particle velocities for the same reasons as described in the experiment of a single feedstock powder. Both torches have the same general trend where higher particle temperature and higher particle velocity occur concurrently. It is also clear that the Amperit 556 powder experiences higher particle temperatures and velocities than the other two powder. The two differences in the feedstock powder include the powder's smaller particle size and smaller carbide size. It is likely that the smaller particle size accounts for faster heating rates, with a larger surface area able to be heated at the same volumetric feed rate, while being lighter would account for the quicker acceleration of the particles within the plume.

The analyzed signal-to-noise ratios for the GF-HVOF particle temperature and velocity, with a different selection of parameters, are shown in Figure 3-11. A reduced and constant feed rate among the different powders was used for particle state measurement.

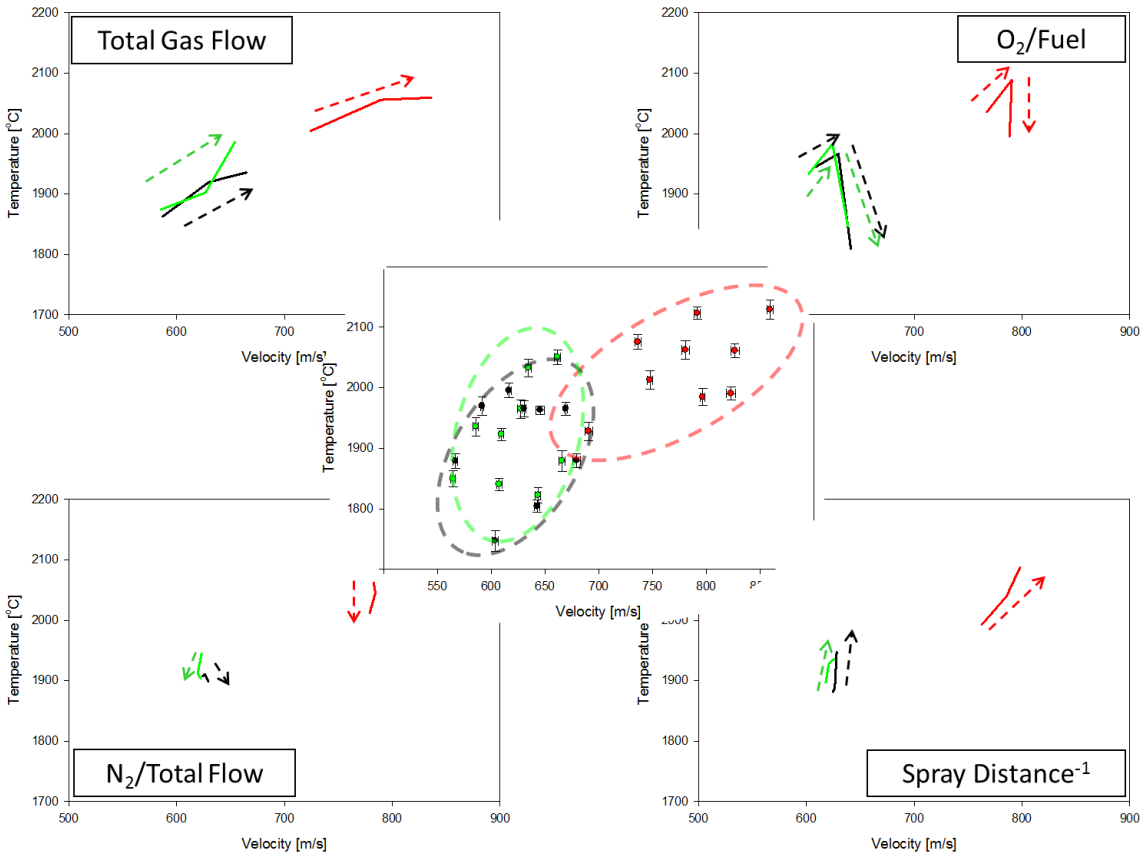

Figure 3-11 Signal to Noise ratio of Diamond Jet operating parameters on particle temperature and velocity for three WC-CoCr feedstocks

It is seen in Figure 3-11 that the total gas flow is again a dominant factor in the particle temperature and velocity, where increasing total gas flow increases both temperature and velocity for all three powders. The stoichiometric ratio shows a different behavior than the signal-to-noise analysis for the JK120H powder for the most fuel-rich conditions, but displays a similar trend for more oxygen-rich conditions. Again, spray distance does not appear to have a

large influence on particle velocity again, expect with the smaller size feedstock powder. The total nitrogen flow, accounted for by the air being used as a shroud gas within the DJ torch, has the smallest effect on particle state, with only marginal drop in particle temperature being the only observable phenomena.

With a design of experiment involving more than spray distance for the JP5220, the spread of achievable particle states within the LF-HVOF regime is more easily observable in Figure 3-10. Analysis of the Taguchi design of experiments for the three WC-CoCr powders are shown in Figure 3-12

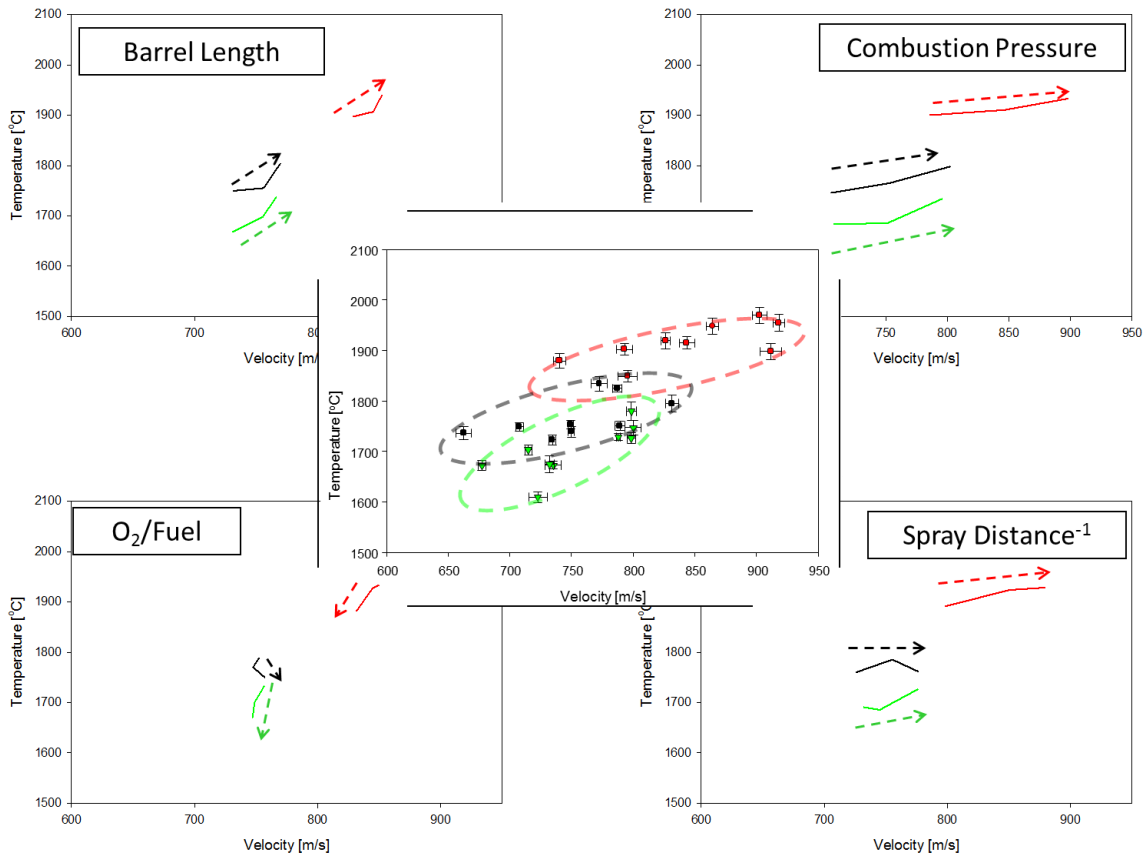

Figure 3-12 Signal to Noise ratio of JP5220 operating parameters on particle temperature and velocity for three different WC CoCr powders

Altering the physical hardware of the gun by changing the barrel length was a unique capability of the LF-HVOF torch, which shows an increase of both particle temperature and velocity with increasing barrel size. This can be attributed to the longer barrels entraining the particles within the exit gas plume for a longer period of time before reaching the atmosphere, allowing further transfer of thermal and kinetic energy of the gases onto the particles. The combustion pressure of the torch offered a large increase in particle velocity over the range selected, with some additional increase in particle temperature with increasing combustion pressure. The spray distance is shown to have more influence on the particle velocity as well, with some effect on particle temperature. Finally, the O_2/Fuel shows a small role in decreasing the particle temperature and velocity with a more oxygen-rich flame.

3.3.2.2 Feedstock decomposition

Since the onset of decarburization is thermally driven, it would seem intuitive that the amount of W_2C in a coating would be influenced by the thermal history of the particle during flight. This can vary largely with torch selection and operating parameters, as observed for the case of a single feedstock in Figure 3-4. In order to gain a wider perspective on the degree of decarburization across feedstock morphology and process, XRD measurements of select coatings produced by the processing conditions in Figure 3-10, along with quantitative W_2C:WC ratios vs. particle temperature, are shown in Figure 3-13(a) and (b), respectively.

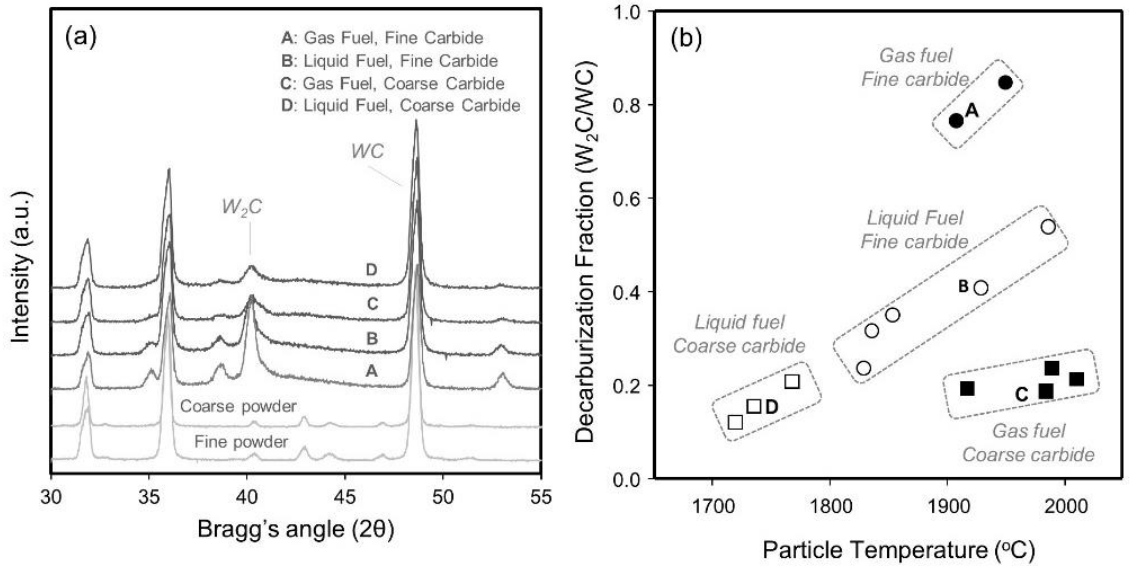

Figure 3-13 Analysis of the extent of decarburization in HVOF WC-CoCr for various processes and material types. (a) X-ray diffraction spectra show that significant presence of W_2C phase in fine (<1µm) and coarse (1-10µm) carbide material. The particle temperature is a contributing factor in the decarburization reaction exemplified through the process map of in Figure 1(b) where the ratio of W_2C/WC is plotted as a function of measured particle temperature (via optical pyrometry).

Varying amounts of W_2C are detected, depending on torch selection and carbide size, as seen in Figure 3-13(a), with the fine carbide powder morphology and GF-HVOF process showing the greatest amount of decarburization. The coarser carbide powder morphology has smaller amounts of W_2C and is largely independent of process selection. The fraction of W_2C:WC vs. particle temperature in Figure 3-13(b) gives an indication of the correlation between particle temperature and decarburization. As only a measurement of the particle's temperature upon impact, the thermal history of the particle will also include dwell time i.e., particle velocity. However, it is still clear to see the trend that a higher particle temperature for a single carbide morphology leads to higher decarburization. It is also very clear to see the sensitivity of carbide size and decarburization, as a higher specific surface area of a fine particle will increase the rate at which the reactions involved in producing W_2C will progress.

With the influence of in-flight thermal soaking of a particle and the associated decarburization with the coating established, the aspect of local deposition temperature is another factor that may have influence on W_2C formation. The X-Ray spectra was measured for the two coatings produced by the condition in Table 3-8 that were deposited at different substrate temperatures by manipulating time between coating strokes, thus allowing the substrate surface to cool to different temperatures. The XRD patterns for the two coatings compared to the feedstock powder are shown in Figure 3-14

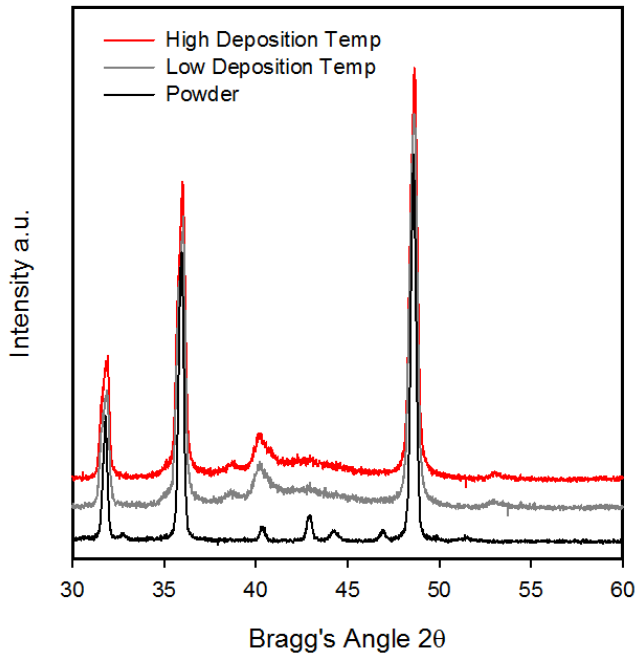

Figure 3-14 XRD spectra of WC CoCr coatings produced by a single LF-HVOF torch condition but different pause time between coating strokes, thus manipulating the substrate temperature

Very little difference is observed between the two coatings, indicating the local surface temperature upon particle impact did not significantly contribute to additional W_2C formation in this case. Overheating of the substrate surface by a very slow surface speed or close spray

distance may provide the amount of necessary heat, but is generally avoided to reduce the risk of overheating a sprayed part. Thus it can be said that the overwhelming portion of decarburization in WC-CoCr occurs in-flight.

3.3.2.3 Formation and Residual Stresses

In order to explore the sensitivity of different feedstock powders on the expected peening intensity of HVOF-deposited WC-CoCr, select conditions from Table 3-4 and Table 3-5 (with particle temperatures and velocities shown in Figure 3-10) were sprayed and evolving stresses were measured via *in-situ* beam curvature measurements. The curvature evolution during coating deposition for the WOKA 3652 and Amperit 556 powder are shown in Figure 3-15(a) and (b), respectively.

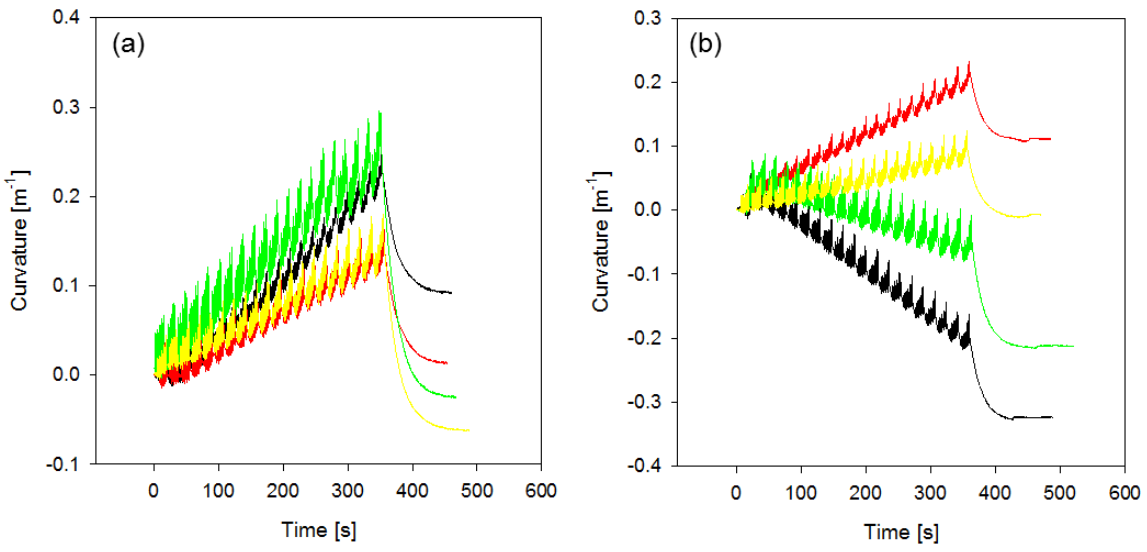

Figure 3-15 Curvature evolution of LF-HVOF deposited WC-CoCr at 65g/min with a raster speed of 1000mm/s for (a) WOKA 3652 showing tensile evolving stress and (b) Amperit 556 showing both tensile and compressive evolving stress.

Here it can be seen that different WC-CoCr feedstock powders with the same range of torch operating conditions behaves differently in the evolving stress of the coating during deposition. Though the measured particle state of the two powders were different, this trend is evident with GF-HVOF deposition as well. In the case of the WOKA 3652 powder, deposition results in tensile evolving stress for all four conditions sprayed. For the Amperit 556 powder, with a finer carbide size, the evolving stress easily span tensile and compressive through the manipulation of torch parameters alone.

In conjunction with particle start and powder morphology, the way in which the coating is deposited can significantly alter coating formation and residual stress. The multiple deposition parameters, including feed-rate, surface speed (rastering), pitch between successive torch passes, can be combined into the effective Deposition Rate Parameter (DRP) as Feed Rate x Raster Speed $^{-1}$ x Pitch $^{-1}$. Previous studies have indicated how the DRP can influence the evolving stress and even coating microstructure [14], primarily through the differences in local deposition temperature and the time between successive particle impact. In addition to feed-rate and deposition control, cooling air and the time between successive coating passes can also influence the coating residual stress, primarily through manipulation of the thermal stress by changing the average temperature of the coating-substrate system during deposition. An example of the measured in-situ beam curvature of a LF-HVOF WC-CoCr coating sprayed by a single torch parameter is shown in Figure 3-16(a), where feed rate and time between successive coating passes were altered.

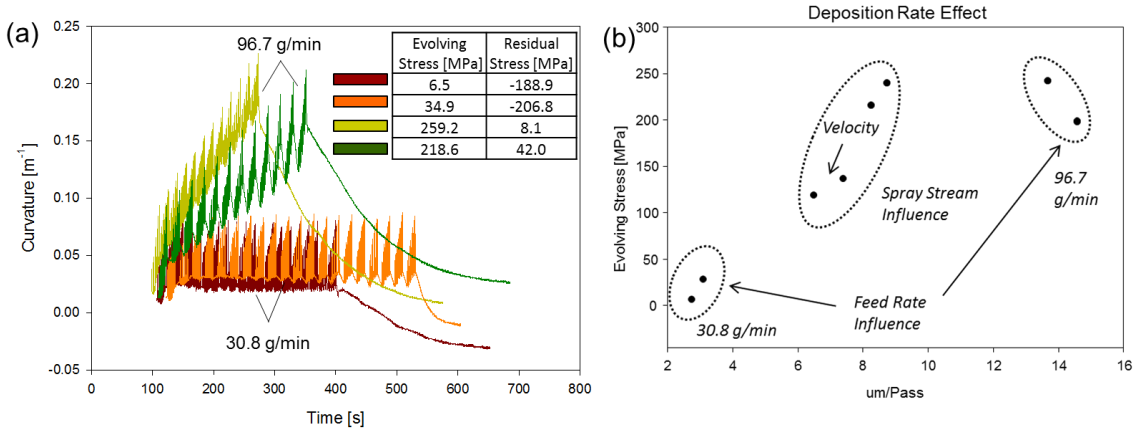

Figure 3-16(a) curvature evolution of a single troch parameters, with variations in feed rate and pass pause time. (b) The calculated evolving stress vs thickness per pass for the same feedstock, with the groupings of torch parameter variation and feed rate variations indicated

Though the coating deposition rate is significantly lower (perhaps to an economically prohibitive level), the curvature evolution of the coatings in Figure 3-16(a) have been significantly lowered with reduction in powder feed rate. Note, there is a small influence in particle temperature and velocity with changes in feed rate, but they can be assumed to be minor relative to torch operating parameters. The calculated evolving stress vs. thickness/pass in Figure 3-16(b) highlights the influence the powder feed rate (and thus deposition per pass) can have on coating formation stresses, especially with comparison to the studies that altered the torch operating parameters (and thus particle velocity) for this powder-torch combination. These operating parameters are those included in the particle state data shown in Figure 3-10 for powder A.

The coinciding residual stress of these coatings, which combine both the deposition stress and thermal stress, indicated that the lower evolving stress of the low feed rate conditions carry over into the final residual coating stress. It is interesting to note that the difference in pause time

between coating strokes produces a significant difference in the coating residual stress. With the higher average coating-substrate temperature that incurs from no pause time between successive coating layer depositions, a higher thermal stress ($\Delta\alpha\Delta T$) is accrued, driving the coating into a more compressive residual stress state upon cooling.

3.3.2.4 Implications on Properties and Performance

Further exploration of the effect of coating residual stress on hardness is shown in Figure 3-17, where a variety of selected coating hardness's from conditions outlined in Table 3-4 and Table 3-5 are shown vs. coating residual stress.

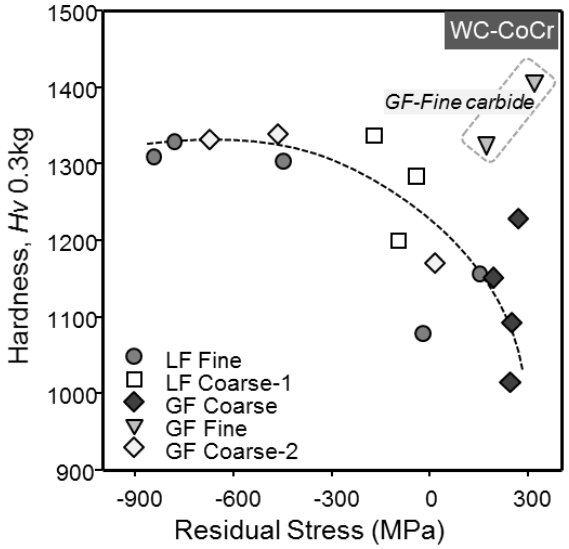

Figure 3-17 The relationship between residual stress and Vickers micro hardness for gas and liquid fuel HVOF WC-CoCr for fine and coarse carbide sizes

Again, there is a noticeable trend that with greater compressive residual stress, there is a higher coating hardness, demonstrated by several powders and torch parameters with similar deposition conditions. The main exception in this plot is the fine carbide feedstock deposited by GF-HVOF, which displays higher hardness. This can be attributed to greater degree of

decarburization and concomitant formation of the harder, though more brittle, W_2C phase. Such a phenomena for the propensity of W_2C formation in high temperature, fine carbide grain sized feed stock was also noted in Section 3.3.1.2

Similar to how evolving and residual stresses can be influenced by deposition conditions, coating properties of WC CoCr can also be effected. One such example is of the coatings produced with a single torch parameter with different pause time between coating strokes, where the top surface indentation modulus and cross section Vickers hardness for the substrate at Low Temperature (LT) and High Temperature (HT) coatings are shown in Figure 3-18

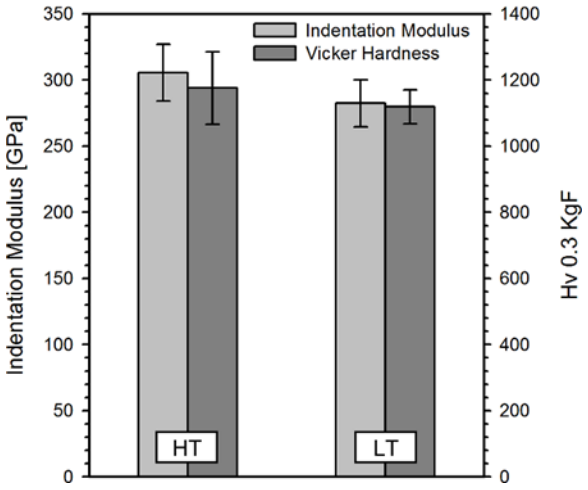

Figure 3-18 Indentation modulus and cross section hardness of the HT and LT WC CoCr coatings

A slight influence on the coating properties is observed, as the coating with higher deposition temperature has a slightly higher coating modulus and hardness, though the differences are within the standard deviation of the measurement. Thus it is more likely to influence coating properties via torch operating conditions and subsequent particle state in this case. SEM backscatter micrographs of the two coating are shown in Figure 3-19 indicating little

visual difference between the coatings' microstructures, though there is a large difference in the residual stress between them.

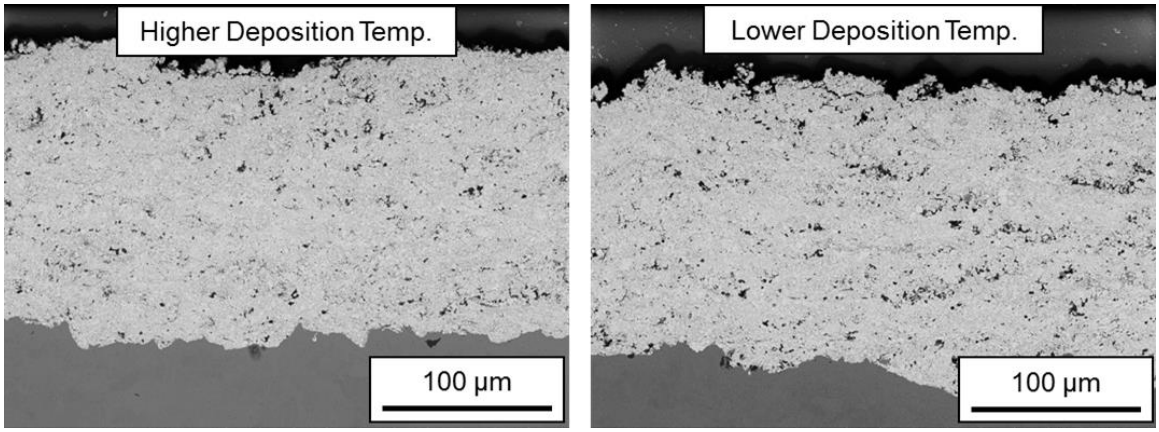

Figure 3-19 SEM micrographs of the WC-CoCr coatings deposited at different substrate temperatures by using difference in pause time between coating strokes

In order to assess the differences in wear and corrosion performance of a WC-CoCr coating based on deposition conditions and not particle state, sliding wear and corrosion tests were performed on the coatings shown in Figure 3-18. The measured wear track width under two different wear loads and the Tafel plots of the coating surface are shown in Figure 3-20(a) and (b), respectively.

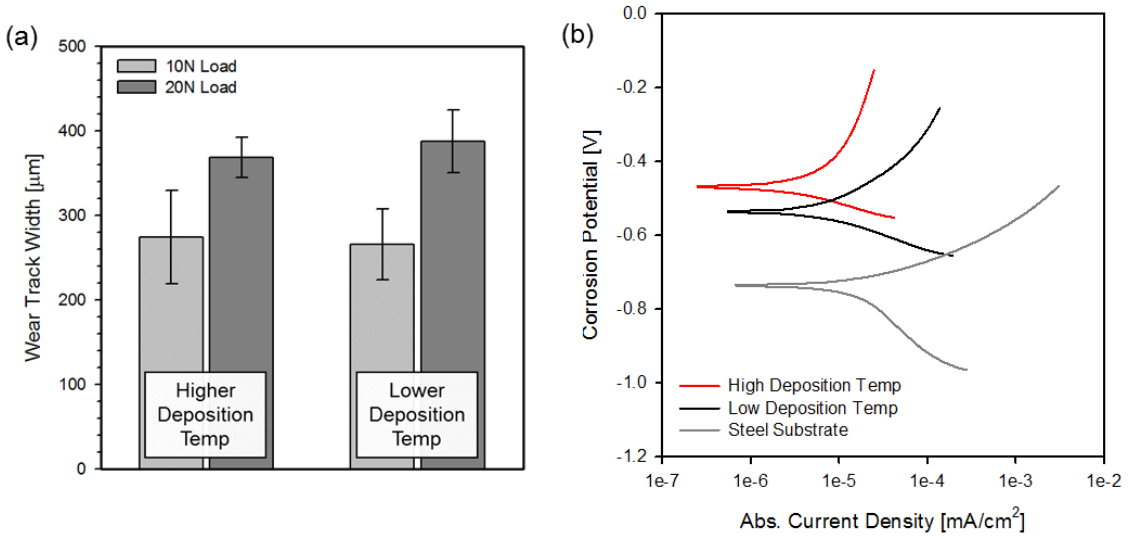

Figure 3-20 Performance Data for the high and low deposition temperature WC CoCr coatings (a) sliding wear track width measured by optical microscopy and (b) Tafel curves from an ASTM G61 type corrosion test.

Based on the wear track width of the sliding wear scar, little difference in the wear performance of these two coatings is observed, despite their largely different residual stresses. There is a slightly higher wear track at the higher load for the lower deposition coating, but the value is well within the standard deviation of the measurements.

A larger difference between the two coatings exist in their corrosion performance, where the higher deposition temperature coating provides a better corrosion barrier than the lower deposition temperature, though both coatings offer better corrosion resistance than the bare steel.

3.3.3 CrC-NiCr – Alternative Damage Tolerant Coating Feedstock

3.3.3.1 Particle State Manipulation

The spraying of a CrC-NiCr feedstock at a fixed spray distance with the LF JP5220 was performed using the conditions in Table 3-9, which emphasizes the influence of the combustion pressure and plume stoichiometry on the measured particle state of CrC-NiCr. Measured particle temperature and velocity are shown in Figure 3-21.

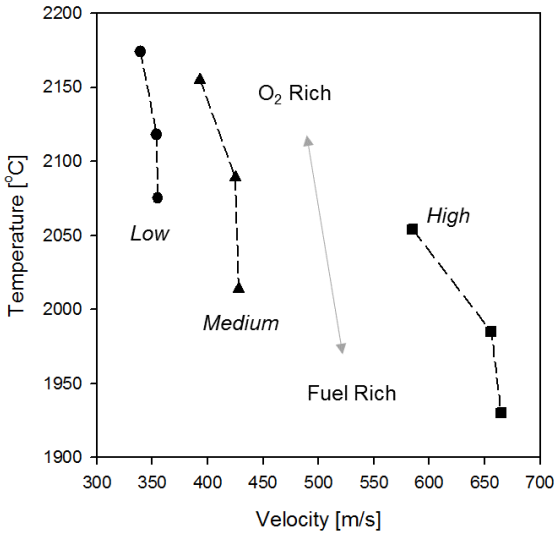

Figure 3-21 Measured particle velocity and temperature of LF-HVOF sprayed CrC-NiCr, with relative combustion pressure and plume stoichiometry indicated

The most striking difference from the measured particle temperature and velocity of the LF-HVOF CrC-NiCr and WC-CoCr is the general trend, where a higher particle velocity coincides with a lower particle temperature. It should be noted that this similar particle temperature between the two different feedstocks does not mean that equivalent states of melting are reached, since different powder size, morphology, dwell time, and intrinsic melting point and thermal conductivity will all determine how molten the particle is. This method of describing the thermal state of a particle is described as the *melting index* parameter [41, 42], but is beyond the scope of this work.

3.3.3.2 In-flight Oxidation and Decarburization

As expected, the higher combustion pressure results in a higher particle velocity and lower particle temperature. However, there is a wide variation in the measured particle temperature, as oxygen-rich torch plumes result in a much higher particle temperature, with the fuel-rich plumes reducing the temperature. This highlights the sensitivity of CrC-NiCr particles to exothermic oxidation. The reaction of particle temperature to an oxygen rich flame stoichiometry is indicative of in-flight particle oxidation occurring due to the presence of Cr. This behavior has also been observed in the case of pure NiCr sprayed by different TS processes [11]. In addition to binder material, the Cr_3C_2 phase can decarburize in different phases, including $Cr_{23}C_7$ and Cr_7C_3 [19, 43, 44]. The X-Ray diffraction patterns CrC NiCr coatings sprayed with LF and GF are shown in Figure 3-22.

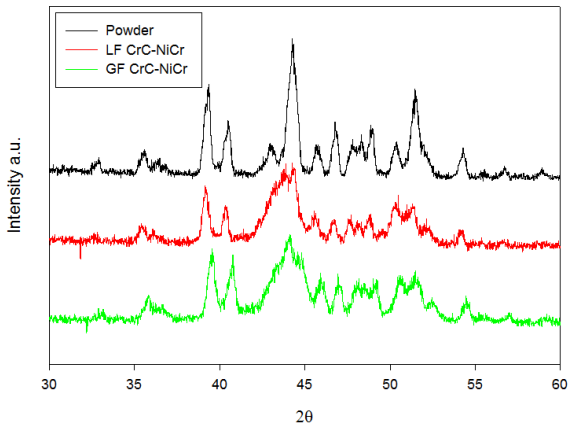

Figure 3-22 Examples of XRD spectra of CrC NiCr powder and coating produced via GF and LF HVOF

Though carbide decomposition and particle oxidation is also important in HVOF CrC-NiCr, X-Ray diffraction pattern of CrC-NiCr coating is not as clear to interpret as the case for WC-CoCr, due to considerable overlap of phase peaks of possible CrC (Cr_3C_2, $Cr_{23}C_7$, Cr_7C_3),

NiCr, and chrome oxide. Additionally, there is little difference in XRD patterns between GF and LF HVOF CrC-NiCr due to very fine distribution of the oxide phases and dissolved carbides. Mechanistically, the thermal exposure of the particle and carbide size will determine decarburization in a similar way to WC-CoCr. However, the oxidation of the Ni and Cr (present in a much higher abundance than in WC CoCr) will be more dependent on the flame stoichiometry, though difficult to quantify with XRD.

3.3.3.3 Peening Intensity and Evolving Stress

The particle state influence of alternative hard facing coating materials, such as CrC-NiCr, will also play a role in the formation and residual stresses present within high velocity TS deposited coatings. Using the measured velocity of the in-flight particles from Figure 3-21, the kinetic energy was calculated using the particle size d50 and density and plotted against the evolving stress of coatings produced using those measured particle temperatures and velocities under the same deposition conditions are shown in Figure 3-23.

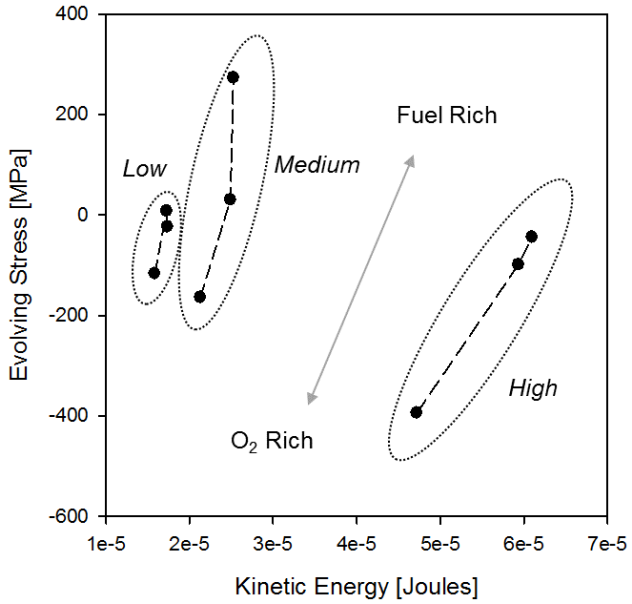

Figure 3-23 Relationship between particle kinetic energy and evolving stress, or peening intensity, with differences in combustion pressure and plume stoichiometry highlighted.

The higher torch combustion pressure clearly increases the kinetic energy of the particles, with some degree of correlation between particle kinetic energy and evolving stress. However, the large role of flame stoichiometry is still observable, where the coating produced with an oxygen-rich plume had greater compressive evolving stresses than those conditions with the same combustion pressure and a fuel-rich flame. This again points to the in-flight particle oxidation playing a large role in the formation stresses of HVOF deposited CrC-NiCr. This can likely be attributed to the oxide film on the particle developed in-flight inhibiting splat bonding upon impact. With reduced bonding, the stresses from splat quenching are reduced as limited force is transduced with splat shrinkage, making the peening stresses from particle impact more dominate in coating formation.

3.3.3.4 Properties and Performance

The hardness of TS sprayed CrC-NiCr is also of interest as an alternative hard facing candidate. Though the intrinsic hardness of CrC-NiCr is lower than WC-CoCr, significant influences on coating hardness from processing still make an assessment of CrC-NiCr processing necessary.

The hardness measurements vs. the residual stress of the LF-HVOF CrC NiCr samples from Table 3-1 are shown in Figure 3-24

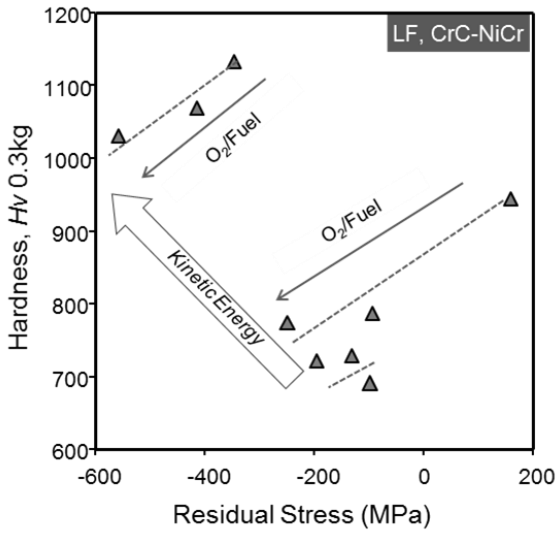

Figure 3-24 The relationship between residual stress and Vickers microhardness for liquid fuel HVOF CrC-NiCr deposited at various process conditions.

In the case of LF-HVOF deposited CrC-NiCr, a clearer trend between the coating residual stress and coating hardness is observable, with the particles with higher kinetic energy producing a harder coating. However, there is still a large role in the plume stoichiometry on the coating hardness. The effect of torch stoichiometry on measured particle temperature and

velocity was observed earlier in Figure 3-21, which carries through into differences in the coating hardness.

The LF-HVOF deposited CrC NiCr coatings shown in Figure 3-21 were subjected to an abrasive wear test, with the results plotted vs the measured coating hardness shown in Figure 3-25

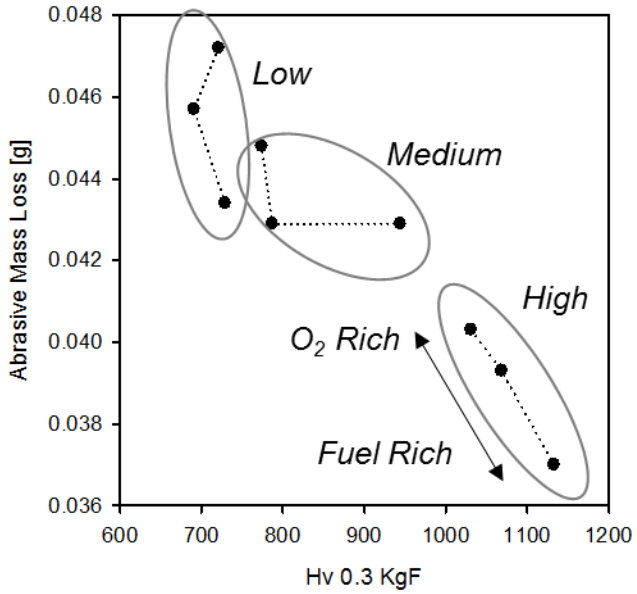

Figure 3-25 Sample mass loss vs. Coating hardness for a G65 type abrasive wear test, with combustion pressure and plume stoichiometry indicated

A clear correlation between the coating hardness and the mass loss of the coating subjected to wear testing shows that with higher CrC-NiCr coating hardness, the abrasion resistant of the coating increases. The groupings within Figure 3-25 indicate the combustion pressures of the torch conditions used to deposit the coatings, with higher combustion pressure generally leading to higher coating hardness. A secondary effect in processing evident from

Figure 3-25 is the influence of the plume stoichiometry, with fuel rich conditions generally having hardness and therefore more wear resistance.

The open circuit corrosion potential for the LF-HVOF deposited CrC NiCr coatings was measured and the results for those produced at the highest combustion pressure are shown in Figure 3-26. Little difference between other coating conditions and the bare steel was measured and are not shown.

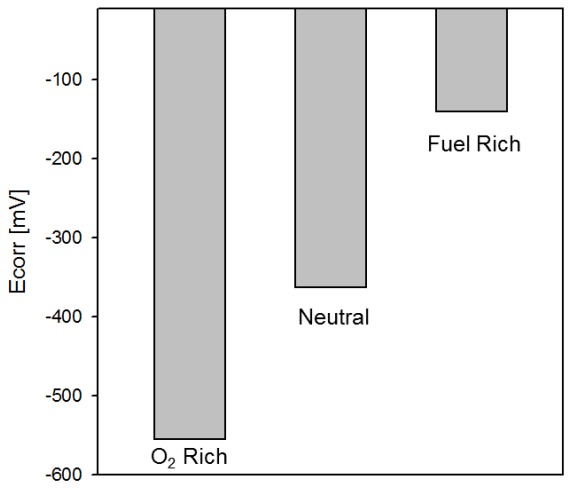

Figure 3-26 Corrosion potential of CrC-NiCr coatings on steel deposited at the highest combustion pressure from Figure 3-21

The corrosion potential for these three coatings produced at the same combustion pressure show a large influence from the torch plume stoichiometry. Here, the oxygen-rich flame offers little corrosion protection above that of the steel, whereas the fuel-rich flame offers excellent corrosion protection, with the neutral plume performing between them. This again gives indication that the properties and performance of TS CrC-NiCr coatings are strongly influenced by plume stoichiometry, resulting in in-flight particle oxidation altering splat bonding

mechanisms. Permeability of the coating microstructure to corrosive solution can also be visually observed, as seen in microstructures in Figure 3-27, where a higher degree of porosity exists in the oxygen rich sprayed condition as compared to the neutral or fuel rich condition.

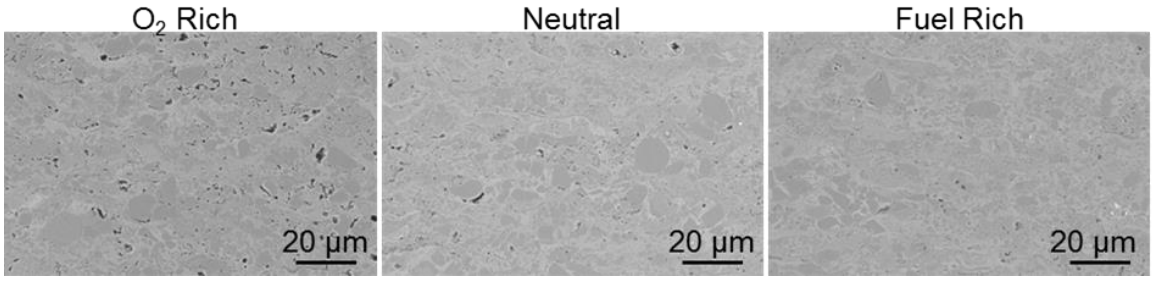

Figure 3-27 SEM micrographs of the CrC-NiCr coatings sprayed by the highest combustion pressure with varying plume stoichiometry. The Oxygen rich microstructure shows a higher degree of porosity as compared to the Neutral and Fuel rich conditions, indicating higher permeability of the microstructure to corrosive solution.

3.3.4 Nickel – Corrosion Resistance and Repair potential

3.3.4.1 Particle-Plume Interactions

As the main alloying element in a large array of superalloys and bond coat materials, as well in surface repair, the behavior of Nickel within a spray plume is of particular interest. The measured particle temperature and velocity of two spray conditions in Table 3-10, high and low, are shown in Figure 3-28, with variations in the spray distance.

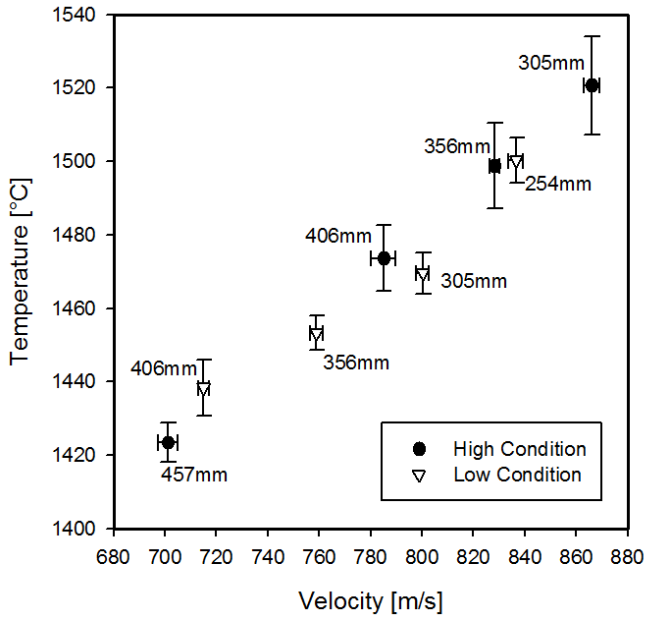

Figure 3-28 Measured particle velocity and temperature for LF-HVOF Nickel with two conditions at varying spray distances

The overlying trend is similar to WC-CoCr, where a higher particle temperature coincides with a higher particle velocity. The dissimilarity from the behavior of CrC-NiCr may indicate that no or limited exothermic in-flight particle oxidation is occurring. Similar trends in particle state were measured with the High and Low spray conditions, where spray distance can be used to closely match the article state between the two conditions, though this shouldn't be considered a universal phenomenon.

When pure metals are considered for high velocity TS, such as Nickel, the nobility and resistance of in-flight oxidation will largely determine the amount of oxides present within the final coating. The XRD spectra of the Ni coatings produced with the High and Low conditions at 406mm. and 305mm. spray distances, respectively, are shown in Figure 3-29 and show no significant difference in phase content.

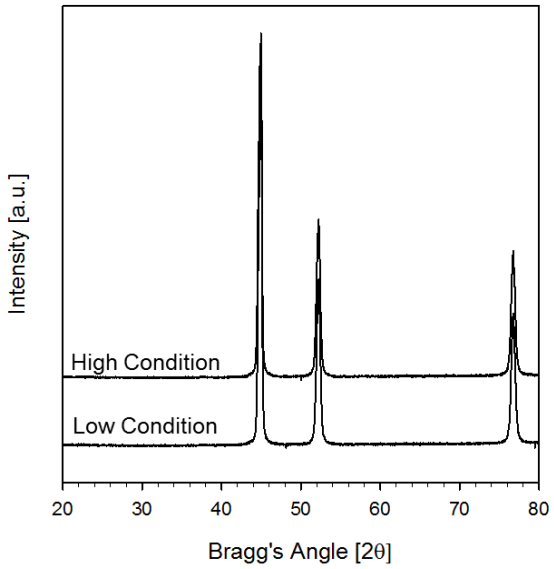

Figure 3-29 XRD spectra of LF-HVOF Nickel coatings, produced with the high and low condition at 406mm and 305mm spray distance, respectively

The phase stability of pure Nickel upon high velocity TS spraying is noticeably clear, as the only observable dominate peaks are of the Nickel, with no observed oxides. Depending upon the coating's functional purpose, small amounts of oxides may be beneficial, as finely dispersed oxides within a TS sprayed metal material may enhance coating strength. However, excessive particle oxidation, which could be experienced in plasma spraying, may inhibit splat bonding, degrading the coating's integrity.

3.3.4.2 Formation and Residual Stresses

Without a metastable hard phase within pure Nickel feed stock powder and limited in-flight oxidation, the formation stresses of high velocity TS sprayed Nickel is somewhat simplified. Coating curvature vs. deposition for the torch parameters of Figure 3-28 are shown in Figure 3-30(a), with the calculated stresses shown in Figure 3-30 (b). The measured particle

temperature and velocity and calculated stress values are very similar, even though these the torch spray conditions were largely different.

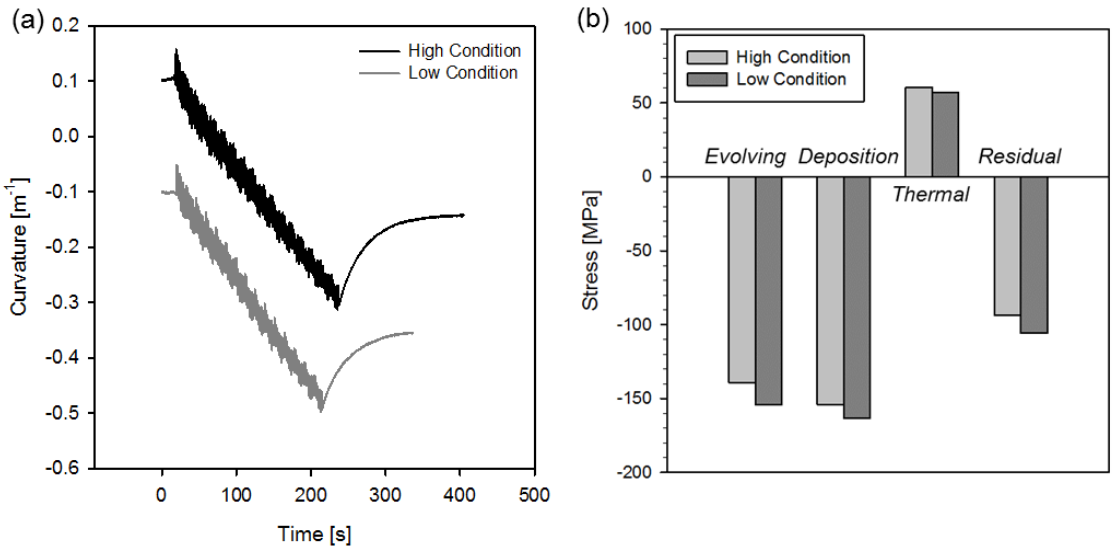

Figure 3-30(a) Curvature evolution for the Nickel coatings deposited at High and Low condition at 406.4mm and 304.8mm spray distances, respectively, with (b) calculated stress values derived from the curvature measurement using the Stoney formula.

With a similar particle state and controllable deposition conditions kept the same, these two Nickel coatings exhibit similar curvature evolution as well as similar stresses during coating formation and cooling. The Low condition has slightly more compressive evolving stress, which may come from a cooler substrate surface during deposition, as evident by the slightly lower degree of thermal stress calculated, or from a lower degree of quenching stress from splat bonding. Micrographs in Figure 3-31 show a slight difference in coating porosity, with the Low condition displaying a slightly more porosity than the coating spray with the High condition

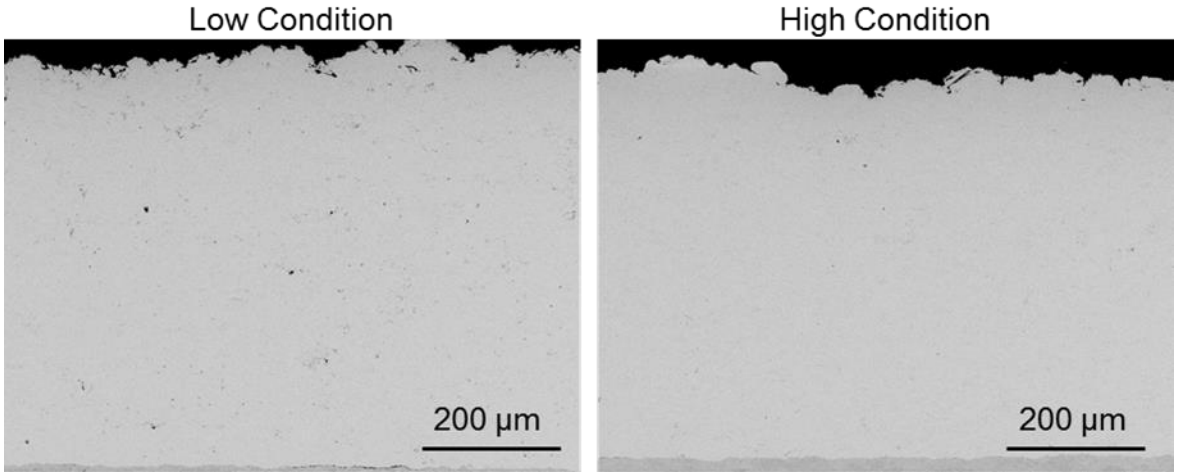

Figure 3-31 backscatter SEM micrographs of Nickel spray at the Low and High conditions

The curvature evolution for the two coatings of a single torch parameter (High condition) with variations in deposition conditions via substrate temperature being manipulated by pause-time between coating strokes is shown in Figure 3-32(a)

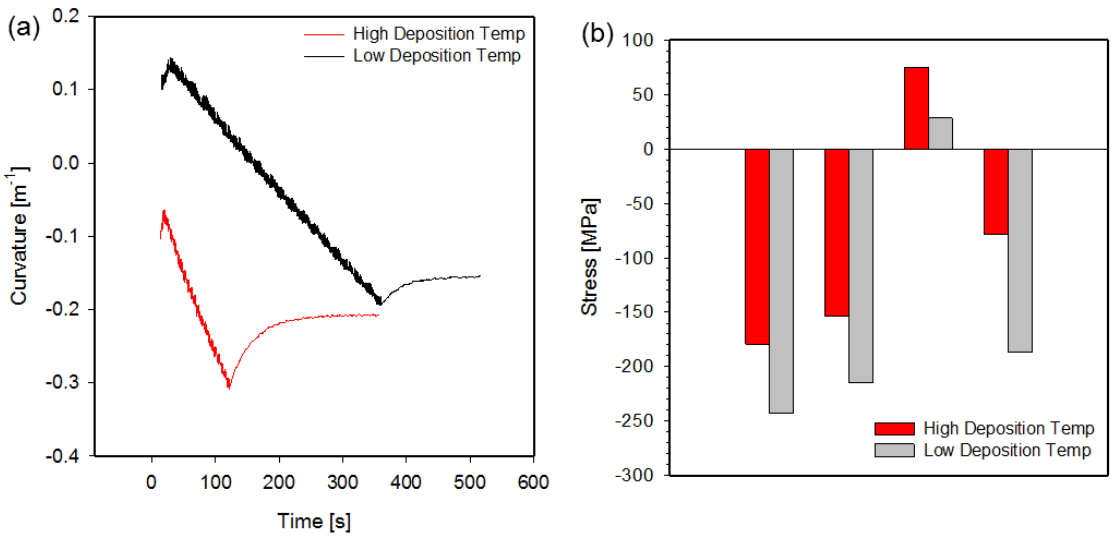

Figure 3-32(a) Curvature evolution of a single torch parameter for LF-HVOF Nickel with variation in pause time between strokes, producing higher and lower substrate temperatures and (b) the calculated stress values from the curvature using the Stoney formula

The difference in deposition rate between the two nickel coatings is clearly observed in the curvature evolution, though calculations of the stresses are required for proper comparison, as shown in Figure 3-32(b). Here it can be seen that there are significant differences in all contributions to the residual stress. As expected, the thermal stress is higher in the coating deposited at a higher temperature, even though there is a relatively small thermal mismatch between steel and nickel (~12 and 13 μm/m °C, respectively). More interesting is the difference in the evolving and deposition stress between the two coatings. The lower deposition temperature coatings have a higher degree of peening during the coating formation, which can be attributed to the impacting particles striking a cooler substrate surface that is more able to accommodate cold working. Micrographs of the two coatings in Figure 3-33 so little variation between the two microstructure, though the residual stresses of the two coatings are quite different.

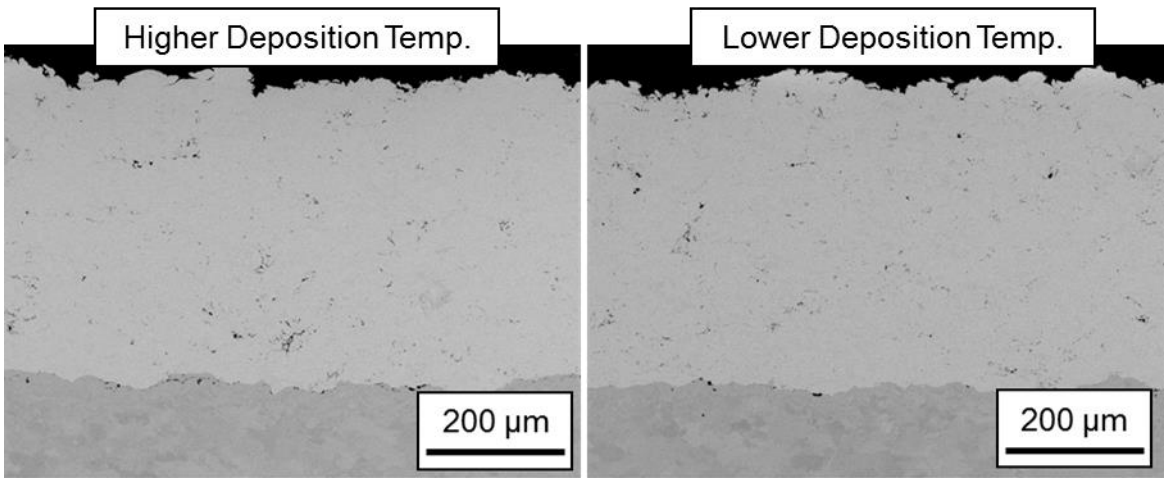

Figure 3-33 Backscatter SEM micrographs of Nickel deposited at the Higher and Lower deposition temperature

3.3.4.3 Properties and Performance

Since the use of a nickel coating is not primarily wear resistance, but is intended instead for corrosion protection or component repair, the hardness of TS Nickel coatings are generally not a great concern for designers. However, the splat-to-splat bonding, and thus the hardness of the coating for corrosion or repair applications, are instead more important. The Vickers hardness of the Nickel coating produced with the high and low torch conditions shown in Figure 3-30 are shown in Figure 3-34

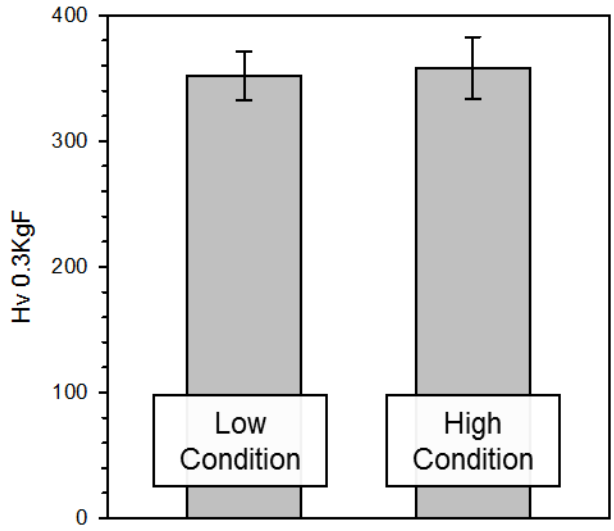

Figure 3-34 Vickers hardness of the Nickel coatings sprayed with the High and Low torch conditions at 406.4mm and 304.8mm spray distance, respectively.

Even with similar particle states and evolving and residual stress, the hardness of the two Nickel coatings made by the High and Low condition reveals little difference in the properties of these two coatings, with the High Condition producing a slightly harder coating than the coating produced by the Low condition, though within the scatter of measurement.

The hardness of the Nickel coatings produced with spray parameters of the High condition but with variable deposition conditions through stroke pause timing are shown in Figure 3-35

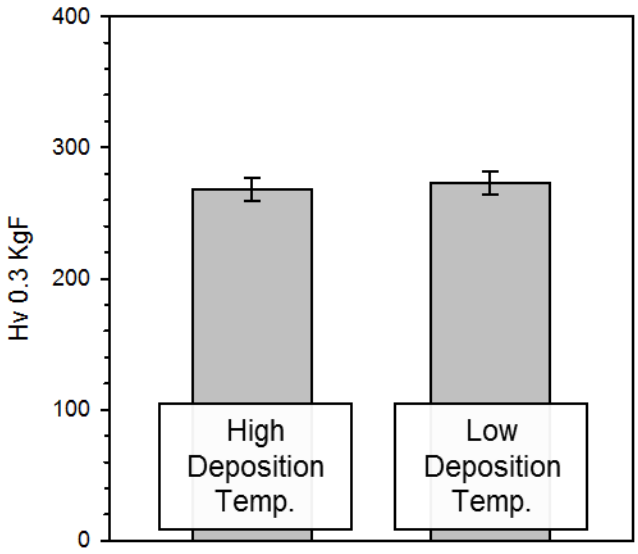

Figure 3-35 Vickers hardness of Nickel coatings produced by different deposition conditions (High and Low Deposition Temperature).

With these results, there is little influence of the deposition stroke timing in LF-HVOF deposited Nickel on the Vickers hardness. This observation could be explained by the balance between splat bonding and extrinsic hardening i.e., peening of the coating during deposition. With a higher surface temperature that comes from little pause time between deposition strokes, the splat-to-splat bonding is enhanced. Densification of the coating may also be enable by the high local temperature and the ease of peening. However, the higher net compressive deposition and residual stress in the low deposition temperature coating may contribute extrinsic hardening that compensates for possibly weaker splat to splat bonding.

As a metal that is intrinsically more noble than steel, Nickel can often be employed as a corrosion barrier coating, protecting carbon steel from infiltration of electrolyte media and reduce corrosion. In the case of a TS nickel coating being used to repair a damaged substrate, particularly if the initial damage mechanism was corrosive, the corrosion performance of the coating critical to the coating design. This performance can be influenced both with processing conditions and deposition parameters, as will be shown.

Tafel curves of the coatings, produced both by the High and Low processing parameters, as well as the variations in deposition temperature, are shown in Figure 3-36(a) and (b), respectively.

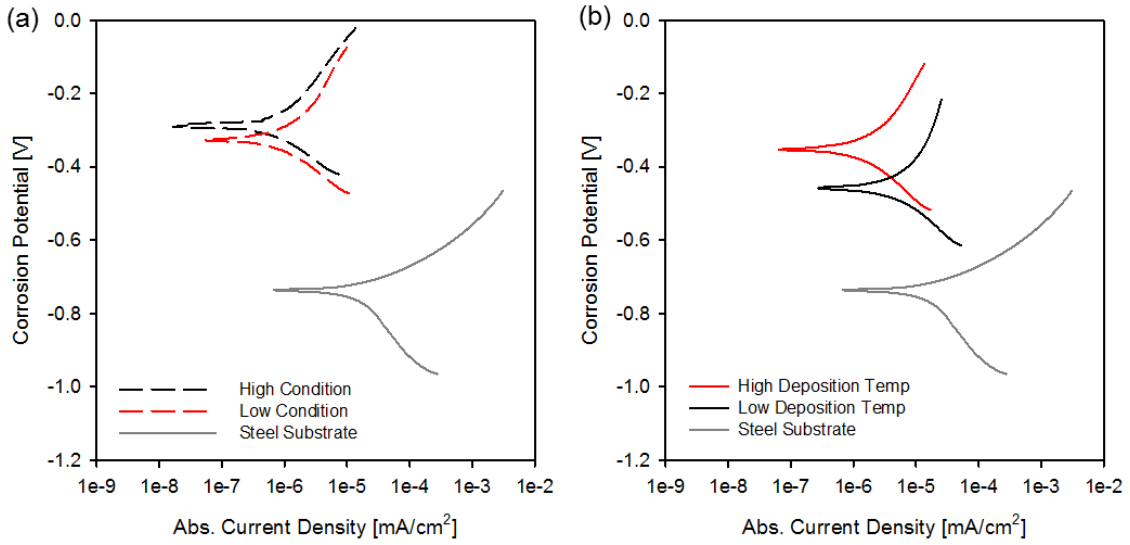

Figure 3-36 Tafel plots of Nickel coatings from a G61 type corrosion test compared to a steel substrate with (a) High and Low spray conditions with the same deposition conditions and (b) High and Low deposition temperatures with the same torch condition, with repeat measurements shown for the coatings.

Little difference in the corrosion performance of the High and Low nickel conditions are observed in Figure 3-36 (a). With a very similar particle state between the two conditions (via

manipulation of spray distance), as shown in Figure 3-28, it can be expected that similar coating performance for the same deposition conditions can be expected. In the case of changes in deposition parameters, it is seen that a higher deposition temperature increases the corrosion performance of the coating, as seen in Figure 3-36 (b). Since particle state is not different between these two coatings, it is the enhanced splat bonding and densification that occurs on a hotter surface that enables a better corrosion performance of the coating.

3.4 Discussion

3.4.1 Particle-Plume Interactions

With the presented results, it is clear that a single global behavior cannot describe the processing and subsequent properties of TS WC-CoCr, CrC-NiCr, and pure Nickel, where each material will interact with processing parameters in different ways and carry this history into the coating's properties. However, there are several governing principals that guide the process development of such coatings. These take into account the manipulation of particle state, deposition conditions, and feedstock decomposition that will determine the processing influence on coating properties.

The selection of TS processes is one of the primary influences in coating formation dynamics, due to the varying capabilities of a torch design to transfer thermal and kinetic energy to a given feedstock powder. As is evident in Figure 3-2 and Figure 3-10, the particle state regimes achievable with a single feedstock powder are significantly different based on GF and LF HVOF, with only marginal overlap achieved with the explored operating parameters. In general, torch design differences between the achievable particle states is responsible for these

differences. Overall torch enthalpy and exit gas velocity will be dependent on the combustion dynamics and process gas flows, changing the experience of the particle within the plume. With a GF HVOF torch, the thermal soaking of the feedstock material is larger than that of the LF-HVOF torch, as the powder is axially introduced into the combustion chamber prior to gas compression and expansion. The radial and downstream injection of powder into the plume of an LF-HVOF dramatically reduces the thermal soaking time of the powder. The LF-HVOF gun also has a larger exit gas velocity [2] than most GF-HVOF torches, propelling the particles to a higher velocity and further reducing the dwell time of the particles within the plume.

Within a given torch selection, significant control of the particle state can be achieved through the manipulation of torch operating variables. The influences of combustion pressure or total gas flow in LF and GF HVOF, respectively, plays a large role in the kinetic energy of the in-flight particles, as observed when torch operating parameters were altered (Figure 3-3,Figure 3-11,Figure 3-12,Figure 3-21, and Figure 3-28). Other torch parameters such as LF-HVOF barrel length or spray distance allow other methods of particle state manipulation, which changes the entrainment and path length of the particles, respectively. The example seen in Figure 3-28 shows how reduction of combustion energy was able to be compensated for by shortening the spray distance. A material such as Nickel experiences very little decomposition/phase changes during flight, as evident by the XRD spectra in Figure 3-29: thus shortening or lengthening flight time will not alter the final coating composition as in the cases of feedstock with carbides or oxidation-prone elements.

The measurement of particle temperature and velocity may also be influenced by factors other than thermal energy transfer from the combustion gases. As was observed for NiCr feedstock [11], in-flight particle oxidation can occur, as would be the case for the oxidation-

prone CrC-NiCr. The operational influence of flame stoichiometry on the measured particle state shown in Figure 3-21 indicates a higher particle temperature under oxygen-rich conditions. Exothermic oxidation of the Cr in the feedstock can give rise to either increased particle heat or may be an artifact of the measurement technique that used light spectra for measurement or both. Suffice to say, the integrity of the feedstock is more prone to degradation with oxygen-rich processing conditions. Though the addition of a hard phase (Cr_2O_3), produced by the oxidation of free Cr, may be considered beneficial for coating hardness, the inhibiting of splat bonding by an oxide skin on the particle has a likely more detrimental effect on the coating's structure and wear performance.

Decarburization, which occurs in both WC and CrC, will also occur during the in-flight travel of the particle. As Figure 3-13 shows, the degree of decarburization is dependent not only on the particle's thermal experience (i.e., particle temperature and time of flight), but also on the surface area of carbide that enablers faster decarburization rate. The fine WC grains in the HC Starck powders are thus more adversely effected by thermal decomposition of the carbides during flight. The formation of W_2C produces a harder coating, but is commonly known to be detrimental to the coating toughness [37]. Similar decarburization of CrC is thought to be detrimental for the coating's wear performance as well [45]. However, it is difficult to characterize the degree of CrC decarburization through XRD, such as the case of peak intensity of W_2C:WC, due to the number of nearby diffraction peaks in XRD for the expected phases within a CrC-NiCr coating.

3.4.2 Evolving and Residual Stresses

Production of residual stresses are innate to TS coating deposition and will be influenced by all aspects of processing, including material composition and morphology, particle state, and

deposition conditions. Being a highly effective indicator to the nature of the depositing coating, the evolving stress offers coating designers unique insight into the projected coating residual stress. It also offers knowledge of the primary formation mechanism involved during coating formation. As a coating property diagnostic, the evolving stress also allows isolated studies of the effects of particle state, powder morphology, and deposition conditions on coating formation: the key processing influences in TS sprayed coatings.

As shown in Figure 3-6 the evolving stresses of the JK120H WC-CoCr is directly correlated to the kinetic energy of the particles for both GF and LF HVOF processing. The high degree of compressive stress (on the order of 1 GPa) seems slightly unexpected, though previous residual stress measurements of splats deposited by high kinetic and thermal energy have indicated the same level of stress [46]. LF HVOF CrC-NiCr also shows a dependence on the kinetic energy of the particle and the associated evolving stress. Intuitively, it makes sense that particles with larger kinetic energies would also be able to induce the most work hardening within a deposit upon impact. Similar past studies have explored this, considering particle size and torch operating conditions on the kinetic energy of HVOF stainless steel [4]. Though increased kinetic energy will increase particle peening, such factors as powder size and morphology will determine the magnitude of such peening, as well as the relative responsiveness to processing changes. In the case of the HC Starck powder seen in Figure 3-15, the fine carbide and powder size shows a high sensitivity to torch operating parameters, being able to experience a compressive or tensile evolving stress. However, large/coarser feedstock, such as SX178 and WOKA 3652 generally have tensile evolving stresses during deposition.

Considering that the evolving stress is the *net* coating formation mechanism, with both quenching and peening forces occurring, such factors as particle oxidation or substrate surface

temperature will change the formation mechanisms of a coating. One such example is that of CrC-NiCr, where the oxidation prone conditions have a more compressive evolving stress, yet they have lower kinetic energies than the particles with the same combustion pressure in a fuel-rich plume have. With oxidation inhibiting the splat-to-splat bonding, the tensile portion of the evolving stress is reduced, allowing for peening to be more dominant. A lower substrate surface temperature, achievable by varying deposition conditions, will also affect how splats bond to the surface [47, 48]. One such example is that of the stress in Figure 3-32, where the coating made with a lower deposition temperature has a slightly more compressive evolving stress with the otherwise same particle state and feed rate. The influence of feed rate, or the effective Deposition Rate Parameter, can be more directly influential on the coating's evolving stress, as shown in Figure 3-16, where lowered thickness per pass drastically reduces the tensile stress during coating formation. However, this may be at the level that is economically unfeasible.

A second contributor to residual stress in a TS coating is the thermal stress. Largely independent of the deposition and evolving stresses of a TS coating, the thermal stress upon part cooling can either induce tensile or compressive stress, depending on the sign difference of the CTE mismatch between the coating and substrate. Higher deposition temperatures contribute to higher magnitudes of thermal stress, which can be alleviated by part cooling or pause time between successive coating passes or strokes. The source of the heat input to a component being coated comes from both the convective heat from the hot gas plume passing over the surface and the latent heat of solidifying particles. Thus, thermal stress is influenced by such aspects as particle temperature and the deposition rate, but is primarily controlled by other deposition controls as seen in Figure 3-32, where pause time between coating strokes effectively reduces the magnitude of the thermal stress.

3.4.3 Coating Properties

The properties of TS materials are considerably different than that of their bulk counterparts. Besides the residual stress induced from processing, in-flight phase changes and splat bonding behavior will dictate the properties of the coating. It is critical to understand the influence of processing on the coating properties in order to achieve a proper coating design for a particular service application.

In the case of damage-tolerant coatings such as WC-CoCr and CrC-NiCr, a combined effort of the coating's superior strength, hardness, and toughness relative to the substrate are all required for effective coating use. The use of these cermet materials rely upon both the hard phase (carbide) and ductile phase (binder) for these properties, but the microstructure, phase composition, and residual stress are all subject to TS processing changes. Coating hardness has long been used as an assessment measurement for the quality of HVOF deposited WC-CoCr. Figure 3-8 shows the hidden variable of residual stress, largely being driven by the evolving stress, correlating well to coating hardness. The successive peening of the particles densifies the coating structure beneath and imparts the compressive residual stress. In addition, the peening phenomenon can work-harden the metal binder matrix, resulting in extrinsic hardening benefits. Particularly in WC-CoCr, other mechanisms may also contribute, for instance, the phenomena of decarburization which is likely prevalent in the case of the DJ coatings. The formation of W_2C in the coating can potentially result in increased hardness due to the higher hardness of the intermetallic phase as well as increased dissolution of carbide in the binder [37, 38]. This may be an explanation for higher hardness of the D7 coating compared to the D9, despite having similar residual stresses.

The hardness of CrC-NiCr, shown in Figure 3-24, again indicates the plume stoichiometry and subsequent in-flight particle oxidation playing a large role in the coating hardness in conjunction with particle kinetic energy. With the deposit compaction that comes from higher particle kinetic energy, the splat-to-splat bonding can still be inhibited by the oxide film that occurs. Though the intrinsic hardness of the CrC NiCr may only be marginally different, the inability of splats to elastically carry load upon indentation due to a less dense microstructure leads to a lower coating hardness.

The local deposition temperature seen by impacting splats can be manipulated by allowing greater substrate cooling, allowing more peening to accrue in some cases, as seen in Figure 3-32 However, there can be implications of the splat bonding behavior, where a cooler substrate surface will have lower bonding of the splats to the surface. This influence is not as large as is particle state, with the measured hardness of Nickel sprayed this way (Figure 3-35) indicating little difference between the warmer and cooler substrate surfaces. This can be attributed to the possibly competing effects of higher wetting and lower quenching rate of the splat in the warmer substrate temperature, allowing a better bond to form, as well as the higher surface temperatures allowing easier densification. However, extrinsic hardening through greater peening intensity and compressive residual stress in the lower substrate temperature samples may compensate in hardness for the lower splat-to-splat bonding. Preliminary indentation modulus of the two coatings indicate a higher modulus of the warmer substrate coating, pointing to a better degree of splat-to-splat bonding.

3.4.4 Performance

In the validation of a TS coating, some performance test is often required in order to estimate the expected behavior of a coated material in service. Controlled exposure to the expected service wear or corrosive scenarios yields useful information to the designer and offers insight into the characteristics of the coating and the processing methods involved. Again, the linkage between TS coating processing, properties, and performance all need to be understood for the proper design of a coating for a specific purpose.

In the case of damage-tolerant coatings such CrC-NiCr and WC-CoCr, wear performance is critical in assessing the potential benefit that a coating may have. As Figure 3-9 (a) shows, parametric influence on the coating's abrasive wear mass loss is observable, as the higher kinetic energy and lower decarburization of coating D9 (as opposed to D1) tend towards denser microstructure and preserved feedstock composition, respectively. The similar hardness of D9 to D5 indicates little wear difference, but D9 still performs better due to the higher compressive stress induced during deposition. The influence of coating hardness on the wear behavior of CrC-NiCr is clearly observed in Figure 3-25, where a higher coating hardness resists abrasive wear mass loss. Artifacts of coating processing such as particle state and evolving stress are strong influencers in this performance data. The ability to manipulate residual stress through deposition conditions showed no great difference in the sliding wear test, shown in Figure 3-20(a). This is also indicated by the indentation modulus and hardness measurements for these experiments (Figure 3-18). Thus, it is largely the formation stresses arising from particle state and torch operating conditions that determine the coatings wear performance. With coating formation monitoring and process design capabilities outlined above, the ability to optimize a wear resistant coating for a giving feedstock material is readily achievable.

In addition to wear resistance, corrosion barrier protection is another key performance requirement of a damage tolerant or material repair coating. In the case of WC-CoCr, Figure 3-9(b) highlights the parametric influence of particle state on both the corrosion potential and corrosion current. Though all three coatings offer better corrosion protection compared to the steel, the different densities and stresses of the coatings differentiate the ability for the coating to protect the substrate. Additional compressive stresses induced by thermal stress also aids in the coating's corrosion resistance, as seen in Figure 3-20(b). The mechanism for this could be described as the compressive stress aiding in closing micro-cracks, inhibiting the penetration of electrolyte. However, it could also be the increase in splat bonding corresponding to a higher substrate temperature (and thus higher thermal stress) that is the mechanism for increased corrosion resistance in this sample.

In the case of CrC-NiCr, the results in Figure 3-26 show a high dependence on the plume stoichiometry, and thus inter-splat bonding, to ensure a dense coating that will hinder the infiltration of electrolyte solution. Past corrosion studies have shown that interconnected porosity and residual stresses will either hinder or allow the penetration of electrolyte solution to attack the base material [49]. Adequate coating thickness, coupled with dense and compressive coatings will ensure corrosion barrier protection of the substrate. Fortunately for coating designers, this similar qualities are the same properties one desires for wear resistance. Hence, corrosion and wear resistant coatings can be produced via proper processing that ensures dense microstructures with limited in-flight particle degradation, achievable through high kinetic energy deposition yielding compressive stresses.

In the case of a repair coating, corrosion resistance is both a galvanic coupling issue, as well as ensuring a proper barrier against corrosive media penetration, though there is not always

an explicit need for wear resistance. In the case of Nickel on steel, galvanic coupling is limited, and thus barrier-type corrosion protection is the necessary parameter that can be controlled via processing. The influence of particle state and deposition conditions are seen in Figure 3-36, as the denser and more cohesive coatings protect better against corrosion. Concerning deposition conditions, the coating sprayed at a higher deposition temperature (Figure 3-35) showed considerable improvement in the corrosion behavior as compared with the coating sprayed at a lower temperature. The coating also has a larger magnitude of compressive residual stress, resulting from the additional thermal stress. Thus, in this case, the slightly more compressive evolving stress of the low temperature deposition condition is dwarfed by the overall compressive residual stress. This indicates that within a single torch condition, manipulation of corrosion performance can be enhanced via deposition temperature. Thus, both particle state and deposition conditions are important to determining the corrosion behavior of HVOF Nickel coatings.

3.5 Conclusions

The ability to control and manipulate coating properties for desired surface performance in wear and corrosion through processing has been demonstrated for several feedstock materials using the HVOF process. The processing-induced effects on in-flight particles and their effects on coating properties have been demonstrated in systematic studies that determine the relevant influence of each processing parameters for different feedstocks.

-Particle state from processing parameters will depend on feedstock characteristics to some effect, though combustion pressure/gas flow is the predominate influence on particle kinetic energy

-Peening intensity through particle kinetic energy is one of the most dominant aspects of coating formation in high velocity TS coatings

-Evolving stress and resultant residual stress offers key insight into coating formation and expected properties and performance. Both particle state and deposition conditions determine evolving stress for single feedstock material/morphology

Factors such as kinetic and thermal energy transfer were found to be key in coating formation, with particle-plume interactions also occurring, such as particle oxidation. Extrinsic coating properties i.e., residual stresses, are inherent in the TS process and can also be used to tailor the properties and performances of coatings and are heavily dependent on the coating's evolving stress. The evolving stress is shown to be a direct result of particle state and deposition conditions, both being factors that are controllable by torch manipulation. Key properties to determine intended wear performance, such as hardness for wear resistance, reveal the manifestation of both intrinsic feed stock material properties and the processing-induced changes. Using the key concepts of damage tolerant and corrosion resistant coating formation, the optimization of coating processing for optimized coating performance is readily achievable.

4 Structural Integration of High Velocity Thermal Spray Coatings Part I: Static Tensile Behavior

4.1 Introduction

Most modern TS applications seek to enhance surface functionality of a wide variety of substrate materials. However, the roots of the technology lay in machine component repair, reclamation, and restoration. From its inception in the early 1900s to about the 1960s, worn out engineering components such as shafts, hydraulic cylinders, paper mill rolls, etc., have been restored using TS overlays followed by secondary finishing operations [50, 51] in order to restore a working function. However, the available TS deposition techniques of the time, such as arc and flame spray, were limited in their ability to produce very dense coatings, often with undesirable oxidation of the sprayed material. Given the porosity and defects inherent in these spray assembled materials, most regenerated surfaces were not considered to have the same mechanical integrity as bulk materials and treated as such in applications. As such, the primary duty of these restorative coatings were relegated to simple, low demanding applications such as refitting dimensional tolerance or cosmetic repair.

The last few decades have seen the introduction of advanced high velocity TS process including high velocity oxy-fuel (HVOF), high velocity air-fuel (HVAF) and even non-thermal cold spray based solid state consolidation [52-56]. In all of the above, the very high particle

kinetic energies allow for the synthesis of deposits with near full density. This enhancement in coating density, with considerably more sophisticated deposition and operating controls, has led to concomitant improvements in properties and performance and has led to expanded applications of TS coatings to meet stringent performance requirements. For instance, these advanced coatings offer excellent wear and corrosion resistance and even improved functionalities such as near bulk electrical properties [28, 54, 57, 58].

Increasingly, there is significant interest in considering TS for not just a protective barrier coating but enabling duality of function (structure and surface) through synergistic benefits arising from structurally integrated coatings [59]. Several examples embody this development, including aero landing gear (through replacement of electroplated Chromium), hydraulic cylinders in earth-moving machinery, and repair and reclamation of superalloy gas turbine engine components. More recently, TS has been considered as potential repair solutions for selective locations of infrastructures experiencing severe corrosion and material loss [60]. These new opportunities have pushed the requirement landscape of thermal sprayed layers from just surface modification to one involving system level functionalities. Today, advancements in TS technology may allow for their applications in true structural restoration and even additive manufacturing via layered spray-based assembly.

There has been a significant amount of past work producing near-bulk materials using a spray forming process, generally with low pressure plasma [1, 61-63]. Microstructural characteristics and defects were correlated to mechanical properties of the spray formed materials, often with post processing heat treatments for improved performance [63]. Materials formed ranged from ceramics and layered composites [1] to superalloy compositions for gas turbine applications [61]. Mechanical testing of these spray formed materials were assessed on

free standing coatings, using substrates only for collection of the deposited material and then removed mechanically or through chemical dissolution.

Traditionally, the design of structural members does not take into account any load bearing contributions of the sprayed layers. As new opportunities emerge for spray based structural reclamation and additive manufacturing, several questions arise as follow;

- Mechanical behavior/strength of the spray assembled materials.
- Adhesion with the parent metal and bonding at the restored/substrate interface.
- Changes, if any, to the characteristics of the remaining original structure, having been subject to impacting particles (peening) and thermal effects during processing.
- Fatigue and cyclic load performance of spray coated metallic composites.
- Corrosion response of the reclaimed system and potential galvanic issues.

In addition to microstructural integrity, residual stresses play an integral role in defining the properties and performance of a TS coating, including hardness, reclaiming strength, wear and corrosion behavior [64]. The evolution of these stresses are complex, arising from impact, thermal mismatch and phase changes. In processes involving melting and solidification, large tensile quenching stresses arise due to constrained shrinkage and cooling of impacting droplets [7]. Thermal mismatch stresses are imposed due to expansion mismatch between the depositing material and substrate. In high velocity spray processes, additional stress variants arise due to solid state peening, which results in local compressive stresses. All of the above stress variants and their intensities are affected by material, process condition, and parameters, as described in

Chapter 3. Impact and peening processes may offer the benefit of compaction of deposited layers, enhancing the characteristics of these coatings. Much progress has been achieved in understanding formation and quantification of residual stresses including process parameter effects to control such stresses [65]. The above attributes of substrate-deposit interaction, microstructural integrity, and state of stress in deposited material all affect the effective properties of the coating, and ultimately that of the substrate-coating system. The latter is of significance in structurally integrated coatings whose major role requires load bearing

4.2 Experimental Methods

4.2.1 Spray Coatings

4.2.1.1 Nickel Coatings

Commercially available nickel spray powder (NI 914-3 - Praxair Surface Technologies, Indianapolis, IN, USA) was sprayed using a liquid fuel HVOF thermal spray torch (JP 5220 - Praxair Surface Technologies, Indianapolis, IN, USA). Spray parameters are indicated in Table 4-1.

All nickel coatings were sprayed with a 102mm barrel and a standoff distance of 406mm. Nickel was chosen as the reclaiming material for various reasons as stated below

- When sprayed, nickel and nickel alloys experience limited in-flight oxidation compared to ferrous alloys during TS processing (steel powders were also tested but they were found to experience significant inflight oxidation resulting in poor consolidation).
- Relatively small thermal expansion mismatch with steel and ferrous alloys.

- Excellent ductility, enabling densification and peening during high velocity TS processing.
- Reasonable corrosion resistance.

4.2.1.2 Other Feedstock Materials

Other feedstock materials, including copper (Diamalloy 1007, Oerlikon Metco), WC-CoCr (WOKA 3652, Oerlikon Metco), Alumina (ALO 1110HP, Praxair), and Alumina + Nickel were deposited by the HVOF process to investigate the mechanical response of different coating materials with conditions listed in Table 4-1.

Material	Condition	Kerosene [L/hr]	Oxygen [SLPM]	Spray Distance [mm]	O_2/Fuel	Combustion Pressure [MPa]
Nickel	A	25.7	821	406	0.93	0.69
Nickel	B	25.4	943	406	1.09	0.71
Nickel	C	17.0	453	406	0.78	0.35
Copper		15.9	932	356	1.71	0.63
WC-CoCr		24.6	943	330	1.12	0.74

Table 4-1 Processing conditions for coatings produced with the LF-HVOF JP5220 torch

Deposition of Alumina and Alumina blended with Nickel powder by HVOF required the use of the HV2000 torch by Thermac Inc. in order to provide the necessary heat to melt the ceramic powders. The torch condition used is shown in Table 4-2

Hydrogen [slpm]	Oxygen [slpm]	Spray Distance [mm]
710	280	150

Table 4-2 Torch condition for HV2000 used to deposit Alumina coatings

Cold Spray and Arc Spray Aluminum were deposited onto Aluminum substrates in order to compare high and low velocity deposition processes for additive manufacturing. Arc spray and Cold spray were used to deposit aluminum coatings using a Thermion 500 and CGT 4000, respectively. Conditions used for the Thermion 500 are shown in Table 4-3

	Condition
1	Low Power, 152 mm Spray Distance
2	High Power, 152mm Spray Distance
3	High Power, 76mm Spray Distance, 2x raster speed

Table 4-3 Power, Spray Distance and relative raster speed of Aluminum sprayed by Thermion 500

Conditions for the CGT 4000 were kept consistent with a chamber pressure of 35bar and a gas temperature of 350°C. Deposition rate was changed by altering raster speed and feed rate, as seen in Table 4-4

	Condition
1	300mm/s Raster, 32 g/min Feed Rate
2	500mm/s Raster, 32g/min Feed Rate
3	500mm/s Raster, 16g/min Feed Rate

Table 4-4 Deposition conditions for Cold Sprayed Aluminum using the CGT 4000

Unless otherwise noted, coating thicknesses were attempted to be sprayed at ~10% of the corresponding substrate thickness

4.2.2 Particle State Measurements

In cases of comparing torch parameters for nickel coatings, inflight particle properties (average temperature and velocity) were measured using an Accuraspray G3 ™ (Tecnar Automation LTEE, St-Bruno, QC, Canada). Measurements were made prior to coating deposition at the stand-off distance of the would-be surface, with the average of more than 10 seconds of recorded data used for reported values.

4.2.3 Coating Stress Analysis

Coating stress calculations were made through the measurement of *in-situ* beam curvature, with stress values calculated using the Stoney Formula [6]. Substrate temperature was concurrently measured via contact thermocouple on the substrate back-side.

4.2.4 Coating Properties

4.2.4.1 Hardness

Vickers Hardness was measured using a 300g load for 15s on the polished top surface of coupons sprayed alongside the beam curvature monitoring, as well as the substrate material. Measurements of the indent diagonals were performed using optical microscopy.

4.2.4.2 Indentation Stress Strain

Indentation Stress Strain measurements of coating surfaces were achieved using WC-Co Brinell indenters at 6.4mm and 3.1mm dimeters at loads of 5, 10, 20, and 30kg force. The diameter of the indented surface was measured using white light optical profilometry (Zygo Corporation, Middlefield CT). Stress and Strain were calculated using the Taber method, described in ref [66]

4.2.5 Coating Deposition

To assess the mechanical behavior of the coating-substrate system, coatings were sprayed on both sides of the steel specimens as shown in Figure 4-1. To ensure good bonding during spraying, the tensile substrates were grit blasted with alumina grit on both sides, followed by air blowing away excess grit. They were then placed in an acetone ultrasonic bath to remove any embedded grit. For nickel coating application, the substrates were mounted on a disk and spun on a carousel with the torch rastering past the necked region with shielding to reduce over spray on the gripping portion of the dogbones. After coating one side, the specimens were flipped and coated to equal thickness on the other side. Air cooling was directed at the samples during spraying, which kept the substrate temperature to be below 300°C (monitored with infra-red thermal camera). Non-nickel coated samples were sprayed in a stationary manner, where the tensile specimens were fixtured and the spray torch rastered over the surface to deposit the coating.

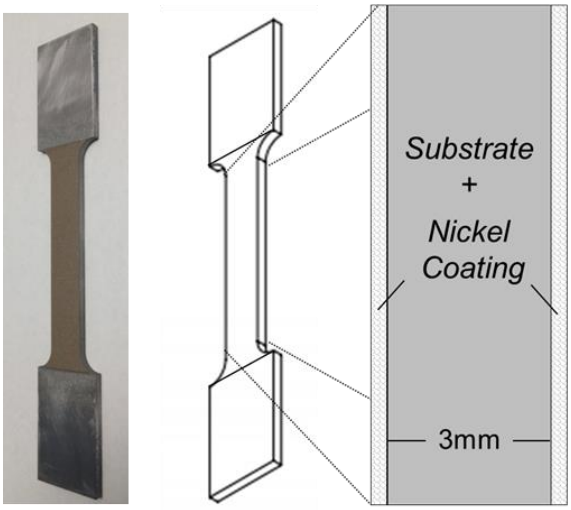

Figure 4-1 TS Nickel coated specimen and its schematic (neck width 12.7mm, length 63.5mm). Note it is coated on both sides to maintain symmetry.

4.2.6 Substrate Preparation

4.2.6.1 Steel Samples

The substrates were commercially produced rolled 1008 carbon steel sheet materials and laser cut into a dog-bone shape. Substrates were used either in the as-received condition, stress relieved at 300°C in a furnace under inert atmosphere, or mechanically grooved in order to simulate "damaged" substrates prior to spraying. Select steel samples were fully annealed at 925°C for a soaking time of 2hrs before furnace cooling back to room temperature in order to remove the rolled grain structure of the steel. Annealing was performed under vacuum.

4.2.6.2 Other substrates

Copper (>99.9%) tensile specimens of the same dimensions were additionally prepared, and were annealed at 500°C in a furnace under inert atmosphere. Aluminum 6061 Samples were sprayed in the as received condition, though were thicker (4.7mm) than the steel or copper.

4.2.7 Tensile Testing

All the tensile tests were conducted with a servo hydraulic tensile testing machine with a static 200kN load cell. The deformation within the sprayed specimen was measured with a clip-on extensometer (with resolution of ~1µm) with the clips placed 25mm or 50mm apart. The mechanical arm pull rate was set at 2mm/min, producing a strain rate of 0.033/min between the two grips, approximately 60mm apart. In all cases, at least three samples from each condition were tested for repeatability

4.3 Results

4.3.1 Mechanical behavior of nickel coated steel

4.3.1.1 Nickel Deposit Characterization

It is well known that thermal spraying introduces residual stresses in both the coating and the substrate due to splat quenching, impact peening, and mismatch in coefficients of thermal expansion. The extent of residual stresses in the deposit, as well as the mechanical properties, is known to be sensitive to spray parameters. To assess their role in understanding the performance of the spray coated laminates, three different sprayed parameters were investigated to yield differences in nickel coating properties as well as interactions with the substrate. Average in-flight particle temperature and velocity were measured for each condition, shown in Figure 4-2(a). Coating A is sprayed with a high combustion pressure and a reducing flame, which results in high particle velocity and particle temperature. Coating B is also fabricated with high combustion pressure but with an oxygen rich flame to enhance the probability of particle oxidation. Coating C was sprayed with the lowest combustion pressure among the three conditions, resulting in lower particle temperature and velocity.

The hardness and residual stress for these coatings are shown in Figure 4-2(b). All the coatings have significantly higher hardness than that of the 1008 steel. The higher hardness of coatings A and B vs. coating C can be explained from the high densities of these coatings as evident from the SEM micrographs shown in Figure 4-3. Coatings A and B are almost fully dense at >99% of bulk nickel. It is estimated that 95MPa compressive stress is present in coating B, while lesser amount for coatings A and C (65 and 55 MPa, respectively).

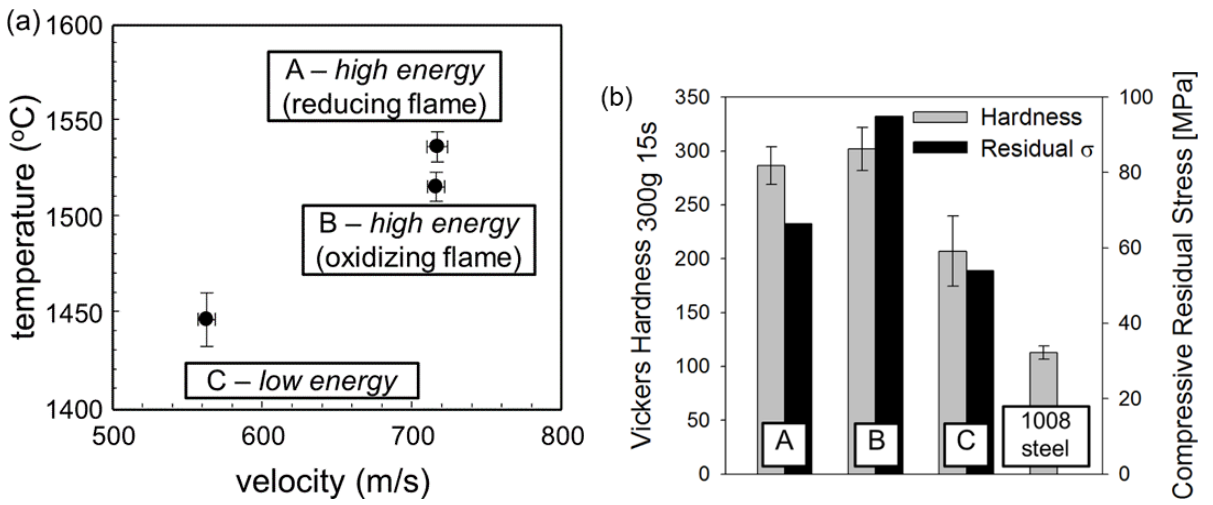

Figure 4-2 (a) Measured in-flight particle velocity and temperature of the nickel sprayed by the parameters in Table 4-1. (b) Residual stress (measured by beam curvature) and hardness of the coatings produced by the same parameters

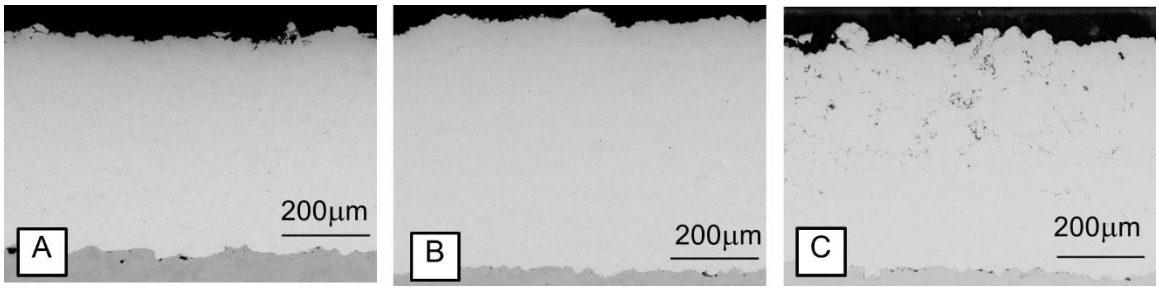

Figure 4-3 SEM micrographs of Nickel A, B, & C coating cross-sections

These compressive stresses and hardnesses affect the overall mechanical behaviors of coated specimens as shown in Figure 4-4, where the tensile behavior of the as-received tensile specimens coated with conditions A, B, and C. All coatings were sprayed to the same thickness of 0.175mm on each side of the tensile specimens, for the total thickness of 0.35mm. In all cases, the stress is adjusted for the increase in the thickness due to nickel addition i.e., the cross-section under load includes the thickness of the coating. Note that "average stress" is shown here

since the actual stresses within the steel and nickel is different due to their different stiffness. The average stress-strain relations of less dense and lower residual stress coating C is very similar to that of steel only specimen which suggests that the actual stress-strain of this nickel coating is likely to be similar to that of steel. On the other hand, specimens with higher energy coatings A and B show higher yield strengths, corresponding with their higher hardness values, as compared to steel and coating C. These measurements show the yield stress of nickel coating to be significantly higher than that of steel. In fact, to account for ~40MPa rise in the average yield strength when the coating is only about 10% of total thickness, its yield stress would have to be greater than that of bulk nickel, which would be unreasonable. Hence, it is likely that some modification of the substrate occurs during the spray process (this will be explained in Section 4.3.1.3). It is also important to note since the compressive residual stresses (55~95MPa) are present in nickel coatings (see Figure 4-2(b)), these stresses must be subtracted when estimating their yield strengths. For processes A and B, the stress-strain behaviors begin to merge at about 0.6% strain.

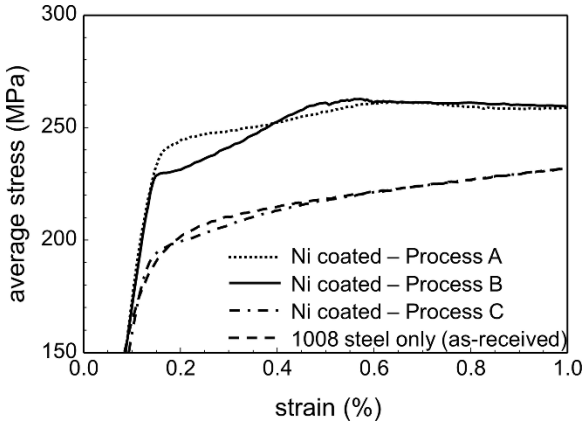

Figure 4-4 Average stress-strain relations of as-received specimens sprayed under different process conditions. All are with 0.35mm thick nickel coatings.

The repeatability of multiple coated specimens was very good (at least 3 samples per condition), as their measured stresses were within ±4MPa for any given strain. The only major variability occurred in the failure above 15% strain (not shown).

As the best performing coating in the sense of hardness, compressive residual stress, and composite stress-strain behavior, coating B was used for additional mechanical characterization.

4.3.1.2 Coating Thickness Effect

Nickel coatings were sprayed to different thicknesses onto the same, as-received steel substrates with the processing parameter of coating B. Here two other coating thicknesses, 0.08mm and 0.70mm, were prepared in addition to the 0.35mm thick coating shown previously. These dimensions were selected to test if a similar behavior can be observed in a very thin coating as well as in a moderately thick coating. The thicknesses of three coatings represented about 2.5%, 10% and 20% of the total specimen thicknesses. Although results of coatings with additional thicknesses will offer clearer picture of nickel coated specimens' behaviors, the selected thicknesses should reveal their dependence on the thickness. Note that for potential applications (e.g., repair), thicker coatings will be more of the interest. In all cases, nickel coatings were sprayed onto both sides of substrate to maintain symmetry. The measured averaged stress-strain behaviors are shown in Figure 4-5. The result of the 0.08mm thick coated specimen differs very little from that of the steel only specimen while the specimens with thicker coating (0.35mm and 0.70mm) exhibited appreciable rises in the average yield stress. Although both specimens yield at around 230MPa, the hardening rate is higher for the one with the thicker nickel coats (0.70mm). The tangent modulus of 0.70mm thick coat specimen is about double of that of 0.35mm thick coat specimen, which is consistent with the coating thickness ratio. However at about 0.35% strain, the 0.70mm thick coating develops cracks within the coating and

also partially delaminates from the substrate near the edge of the filet of the dogbone. At this point the strain hardening halts and the stress remains nearly constant. Although the nickel coating has partially failed at this stage, most is still adhered to the substrate, albeit discontinuously. This explains the stress level being kept around 260MPa and not dropping to the level of the uncoated steel. For the thinnest nickel coating, it may retain strength even at a strain of 1%. However, since its thickness is so much smaller than that of the substrate, its actual behavior is somewhat unclear.

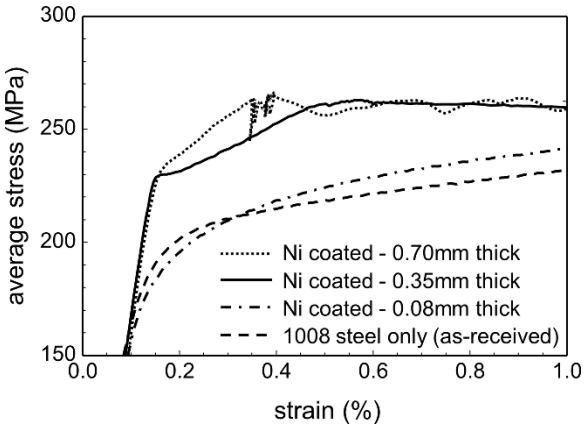

Figure 4-5 Average stress-strain relations of nickel coated specimens with various thicknesses. Specimen without the coating (as-received) is also shown as a reference.

These measured results raise an important question. In elastic plastic bi-metal specimens, if the response of each phase is independent of the other, the effective behavior should still show the nonlinearity near the lower yield strain of the two metals. Here the nonlinear behavior of steel begins at about 0.1% strain but the average stress-strain curve of coated specimen remains linear well-passed this strain. The only way to explain this phenomenon is that the coating application alters the stress state of the steel substrate. This question is more closely investigated in the following section (4.3.1.3).

4.3.1.3 Coating on Stress Relieved Substrates

The results in Section 4.3.1.2 suggest that some changes in the mechanical behavior occurred in the substrate steel due to the heating during spraying (both from the torch and solidifying particles). In order to minimize such effects, 1008 steel substrates were heat treated at 300°C in an inert gas furnace for 2 hours and allowed to cool prior to spraying. This pre-heat treatment condition was selected in order to relieve any residual stresses within the tensile specimens that would otherwise occur during coating deposition, since the measured substrate surface temperature stayed below 300°C during the spray (besides moments when the torch was directly on the measured area). Note that when a molten droplet initially strikes the substrate, the surface temperature rises above this value. However, due to the small size of the droplets, the heat transfer is limited and the high temperature region is relatively small.

The stress-strain relations of "stress relieved" and "as-received" steel specimens are shown in Figure 4-6. The heat-treatment essentially removes embedded stresses and exhibits the upper and lower yield points of the steel (230MPa and 220MPa, respectively) as well as provides linear behavior at higher stresses prior to yield. Both essentially exhibit similar behaviors for strains greater than 0.6%.

Nickel coating at condition B was then deposited on the stress relieved steel substrate. The stress-strain behaviors of coated and steel only specimens are shown in Figure 4-6. Here the stress-strain relation of nickel coating on as-received steel is also included. It essentially overlaps that of nickel coating on heat-treated steel. These results suggest that heat input from spray essentially causes the similar effects on the rolled steel as the heat-treatment at 300°C

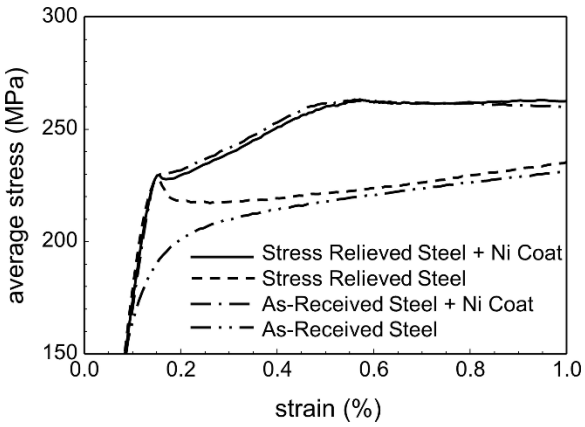

Figure 4-6 Average stress-strain relations of Ni coating on stress relieved and as-received steel substrates. The results of steel only specimens (stress relieved and as-received) are also shown.

4.3.1.4 Estimated stress-strain relation of nickel coating

The large increase in the yield strength of the nickel-coated specimen can be explained by the increase in the effectively heat-treated steel. However, there is a large discrepancy between the post-yielding behavior between the steel and the nickel coated specimens. Based on the results shown in Figure 4-6, the difference in behavior between coated and non-coated stress relieved specimens was analyzed to estimate the property of the nickel coating. First, the elastic modulus of the stress relieved 1008 steel was carefully extracted from the stress-strain relations and determined to be E = 204GPa. Then the linear part of stress-strain behavior of the nickel coated specimen was measured and found to have an effective modulus of 199GPa. From the thickness ratio of coating to substrate, the modulus of the nickel coating was then determined to be 121 ±5GPa. The relatively large error bound arises from the fact that the coating is only about 10% of the total specimen thickness. Thus, the entire stress-strain of the nickel coating is essentially estimated from subtracting the steel-only result from the composite result (after

adjusting for thicknesses). In the procedure, a residual stress of -95MPa in the nickel coating (Figure 4-2(b)) was also taken into account to obtain the nickel coating stress-strain behavior.

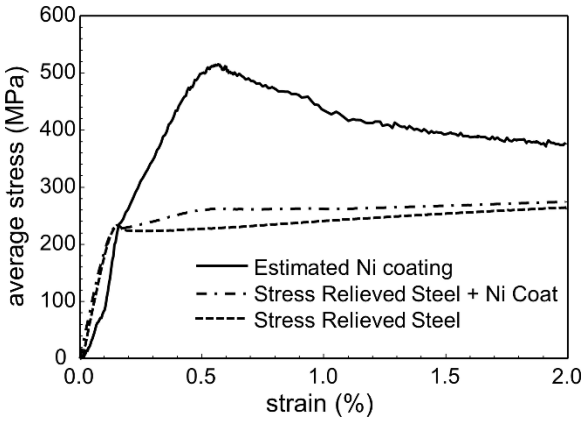

Figure 4-7 Estimated stress-strain relation of the TS Ni coating obtained from the difference in the measured stress-strain results of Ni coated and stress relived steel only specimens

The overall stress-strain relation is shown in Figure 4-7. As shown in the Figure, the estimated maximum stress of the nickel coating is about 515MPa which occurs at about 0.55% strain. Note that the results from repeat specimens are within ±20MPa of this value. Without considering the residual stress effects, the peak stress reaches about 560MPa. After reaching the peak, the stress gradually decreases as damage and cracks begin to develop within the nickel coating (resulting in lower load carrying capability). If a free-standing nickel coating were tested, it would likely fail (fracture) at a lower strain. However, since the coating is adhered to the substrate, it effectively retains its stiffness albeit in a decreasing manner.

4.3.1.5 Repairing of "Damaged" Substrates

In order to simulate the repair of a damaged structural element, the as-received specimens were locally grooved on one side within the gage-section and then re-filled with sprayed nickel as shown in Figure 4-8. It should be noted that it was only this section that used grooved

specimens for tensile testing. Coating were only applied on the grooved side of the specimen. In a preliminary test, the groove depth was chosen to be 0.25mm and condition B described earlier was sprayed. To illustrate *repair* of the substrates to desired load bearing capability by the coatings, the total load vs. extension (between extensometer clips) records are shown in Figure 4-9. As seen in Figure 4-9, the grooved specimen has a lower load bearing capability. After the groove is filled in, the resulting load-displacement curve is raised. The approximate difference in the load is carried by the nickel coat. The post-yield load (~10.4kN) is higher than that of the same thickness steel specimen without groove (~9.6kN). This is possible since the coating has a higher yield strength, as demonstrated in Section 4.3.1.4.

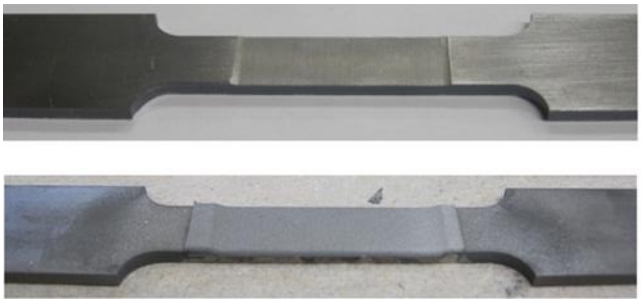

Figure 4-8 Photograph of grooved and nickel repaired tensile specimens

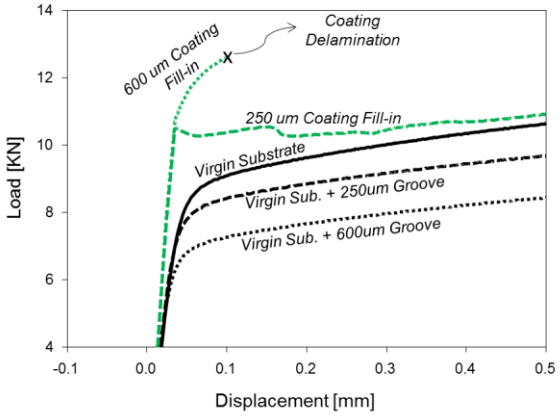

Figure 4-9 Load vs Displacement of grooved and groove-filled steel with the TS Ni coated specimens

4.3.1.6 Substrate Surface Preparation

In all the cases shown thus far, the substrate surface has been grit blasted prior to coating application in order to enhance the mechanical bonding between the coating and substrate. With a weaker bond strength, the ability for the coating to stay adhered under any stressing is reduced. In order to demonstrate the difference in the load bearing capability of the nickel coating based upon surface preparation, coated specimens with and without grit blasting prior to coating application are shown in Figure 4-10

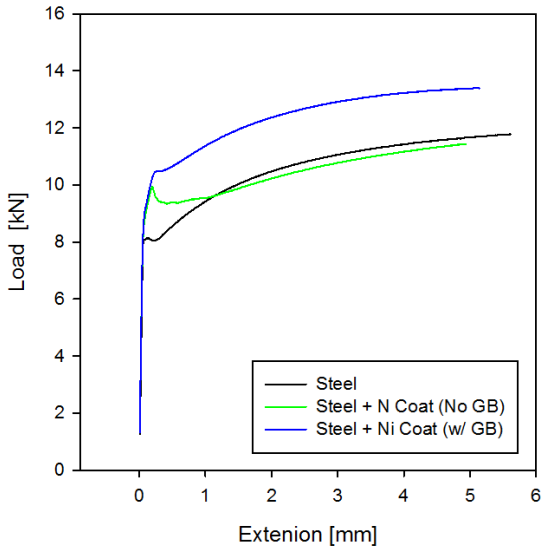

Figure 4-10 Load vs. Extensometer travel for the stress relieved steel plus nickel coating, with and without grit blasting(GB) prior to coating application

The load vs. extension behavior of the two coated specimens are mostly the same prior to yielding, but the load suddenly drops after the yield point in the non-grit blasted sample. In the grit blasted sample, the load continues to be higher than the un-coated substrate. Without proper anchoring of the coating with grit blasting, the load carried by the coated specimen is significantly lower and nearly matches the load-extension behavior of the uncoated steel after ~1mm of extension (corresponding to ~4% strain), as the coating prematurely delaminates. The grit blasted sample continues to carry a higher load long after this strain

4.3.1.7 Nickel Coating on 1018 Steel

Additional tests were conducted for the TS nickel coating on stress relieved 1018 steel (sprayed with condition B). The thicknesses of steel is 6.3mm with 0.73mm of coating. This steel has significantly higher yield strength (325MPa) than that of 1008 steel as shown in Figure 4-11.

This steel shows almost no hardening up to 1.3% strain then begins to harden to 460MPa at about 10% strain (outside the range of the plot). The average stress-strain relation of the coated specimen exhibits a very similar behavior as that of the 1018 steel only specimen. In fact, the only apparent difference is about 20MPa higher average stresses during post-yielding (up to 1.5% strain).

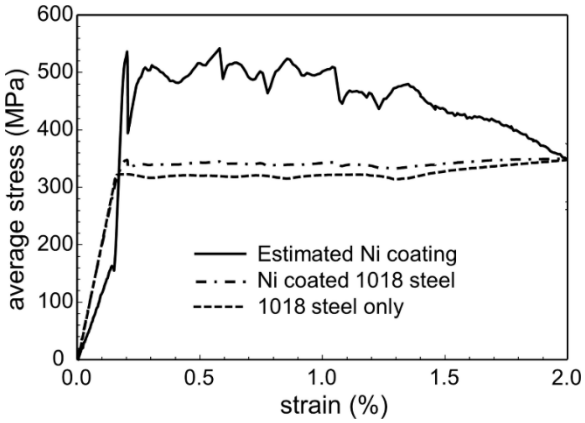

Figure 4-11 Estimated stress-strain relation of TS Ni coating obtained from the difference in measured stress-strain results of Ni coated and 1018 steel only specimens.

The stress-strain relation of the nickel coat was extracted with the same method described in Section 4.3.1.4, with the estimated residual stress of -13 MPa. It is noted that this residual stress value is different from the value measured via bi-layer curvature in Section 4.3.1.1 (-95 MPa), though it is not surprising that the spraying of a stationary flat beam vs beam mounted to a rotating carousel would produce a different magnitude of residual stress due to differences in factors such as cooling and application rate. The peak stress reaches about 535MPa which is consistent with the 1008 steel substrate tests. However due to the higher yield and post-yield stress of 1018 steel, the difference between the steel only and nickel-coated specimens is very small, as shown in the Figure 4-11. Thus the estimated property is less accurate than those

obtained earlier. In fact, a small noise in the measured data translates to larger error and oscillation as shown in the Figure. The estimated post-yielding behavior of this coating is somewhat different from the previous tests. It still exhibits softening but at a lower rate. Nevertheless, the general trend is still consistent with the other cases, and this is described more in detailed in Section4.4.

4.3.1.8 Steel Condition

As indicated in Figure 4-6, the metallurgical condition of the 1008 steel is slightly altered by the thermal input from the TS coating process causing substrate stress relaxation. This changes the behavior of the steel from having a non-linear stress strain behavior near the yield point to having a clearly observable upper and lower yield point. With coating application to both of these steels, the specimen's stress strain behavior near yield is essentially the same, confirming the synergistic benefit that the nickel adds to the steel. However, since the rolled steel does not undergo full annealing at 300°C, the grain structure of the rolled steel remains the same. With a full anneal at 925°C, the rolled grain microstructure of the steel is removed and an isotropic grain distribution within the steel is produced. Etching of the polished cross section of these two steel states in the lengthwise, widthwise, and planar is shown in Figure 4-12.

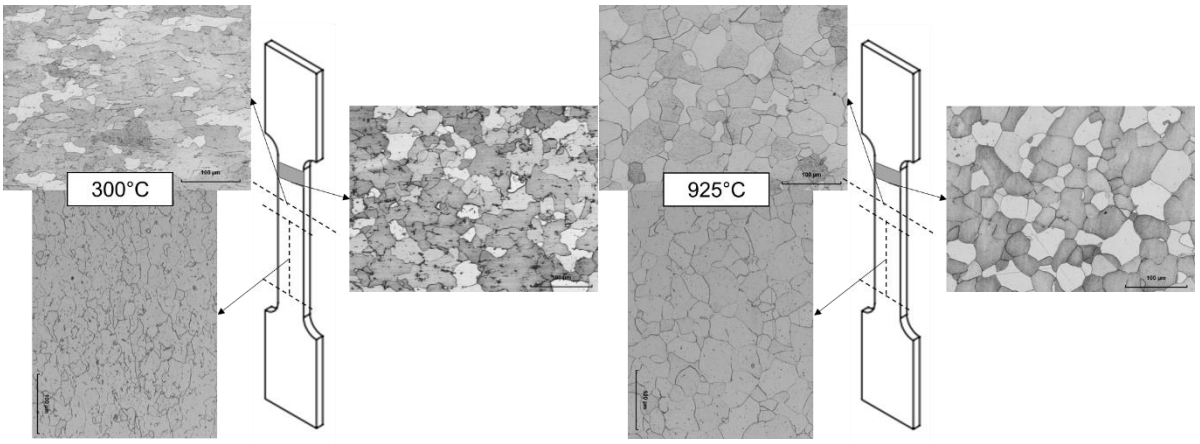

Figure 4-12 Grain microstructure from etched cross-sections of the stress-relieved and fully annealed steel tensile specimens

With a difference in the anisotropic vs. isotropic grain structure of the steels, the expected stress strain behavior can be expected to be different to some degree. Comparisons of the tensile behavior of these two steels are shown in Figure 4-13. The same nickel condition was sprayed onto both substrate types within the same spray run, with examples of the stress strain data shown in Figure 4-13.

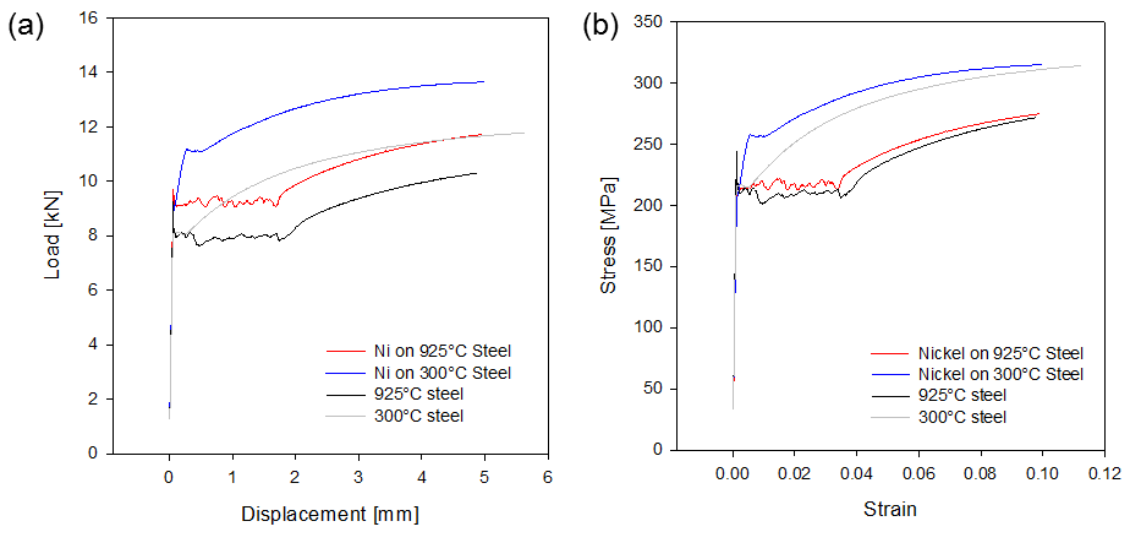

Figure 4-13 Nickel coating condition B on stress relieved and fully annealed steel in (a) Load-Displacement and (b) Stress-Strain.

The tensile behavior of the 300°C and 925°C steel (stress relieved and annealed) show considerable post yield differences in the uncoated state, though the yield point of two are quite similar, indicating that little work hardening was present in stress relieved steel (as well as the as-received 1008 steel). The onset of hardening occurs at a much later strain in the annealed 925°C steel (>0.04%), whereas work hardening begins almost immediately after yield in the stress relieved steel. This difference is likely due to both the grain orientation, as well as size, where the rolled grain microstructure is oriented in line with direction of tensile pulling, allowing limited strain until hardening occurs.

When the same nickel coating is put onto these steels, a noticeable change in the yield behavior of the composite is observed, as well as the load carrying capability. The fully annealed steel does not reach as high of an average stress throughout lower yield point, instead showing

noisy/serrated behavior as the coating likely begins the accumulate damage through cracking or delamination. However, the composite strength is still higher than that of the uncoated substrate, indicating that the coating still offers a benefit to the steel. The extracted stress strain behavior for the coatings on both stress relieved (300°C) and fully annealed (925°C) substrates are shown in Figure 4-14 where it is seen that the nickel coating applied to the 300°C treated steel has a peak stress value soon after the initial yielding of the steel, followed by a gradual decrease in the stress level with further strain. The nickel coating on the 925°C treated steel does not reach the same stress peak and instead shows a choppy stress strain behavior after the composite's yield point. The maximum stress value within the coating is experienced near 0.04 strain, with a behavior similar to the nickel on 300°C steel shortly afterwards. This point corresponds to the onset of hardening in the uncoated steel. Though the same coating was put onto the tensile specimens, the extracted coating properties are different. The exact reason for this is not understood but points to differences in the synergistic behavior of the coating and substrate, which can be seen in Figure 4-13

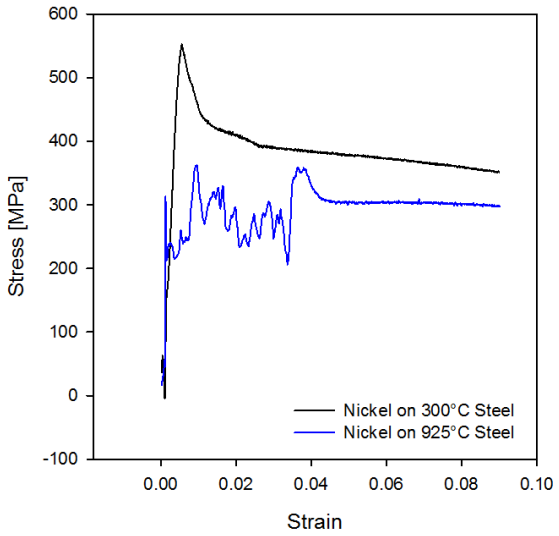

Figure 4-14 Extracted stress strain behavior of Nickel coating on stress relieved and fully annealed steel (300°C and 925°C heat treatment temperature, respectively)

4.3.2 Non-Ferrous Substrates

4.3.2.1 Copper on Copper

When considering the repair of non-ferrous material components, the behavior of the substrate material with coating application and its reaction to the processing conditions must also be considered if one is to properly interpret the strength of the coating. One such example is the spraying of copper onto an annealed copper substrate. Due to the high sensitivity to work hardening, the grit blasting of a copper surface prior to coating application significantly alters the stress-strain behavior of the material. The stress-strain of tensile dog bone in the annealed and annealed plus girt blasting state are shown in Figure 4-15

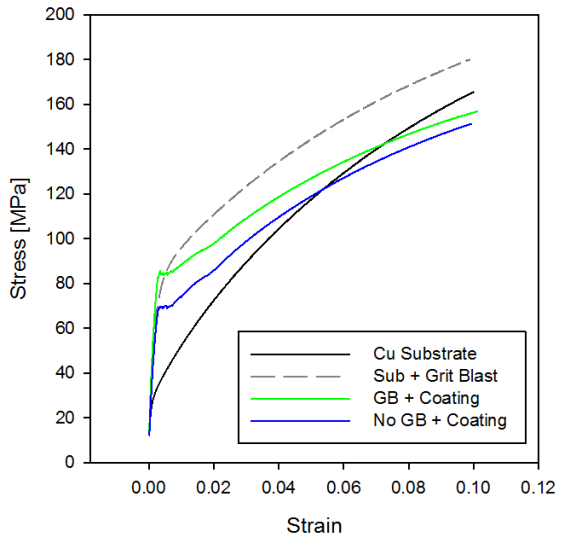

Figure 4-15 Stress strain behavior of copper coating on copper substrates with and without grit blasting prior to coating application. Annealed copper substrate with and without grit blasting also included

Here it is clear to see that the work hardening induced into the copper via grit blasting dramatically increased the yield point of the tensile specimen. Even though grit blasting primarily impacts the stress state near the surface, there is still enough of a change in overall stress-strain of the specimen from the compressive stresses and cold working induced by the grit blasting of the annealed copper.

When a copper coating is applied to each substrate, shown in Figure 4-15, it is noticeable that a net benefit in the stress strain behavior of the coating application is only observed in the case of the non-grit blasted substrate. When the substrate is grit blasted prior to a coating being applied, the average stress strain behavior of the specimen is lower than the specimen with grit blasting alone. It does not make sense that the same coating applied to a grit blasted and non-grit blasted substrate would affect the stress-strain behavior differently, especially since the sample

that wasn't grit blasted prior to coating application (which could be more susceptible to coating delamination) showed the coating improving the yield point of the specimen. Thus, it must be that the coating processes can change the stress-strain behavior of the substrate.

In addition to copper being easily work hardened, it is also easily annealed back to a softer state. In order to ascertain if relief of the work hardening from grit blasting was being achieved by the coating process, the coating property approximation method used for the extraction of the nickel coating properties shown in Figure 4-7 and explained in Section 4.3.1.4 was used. First, the stress-strain properties of the coating were extracted from the sample that was not grit blasted prior to spray. These coating properties were then *subtracted* from the coated specimen that was grit blasted prior to spraying. This difference reveals the stress strain behavior of the grit blasted substrate that has been exposed to the heat from the coating process and is shown in Figure 4-16.

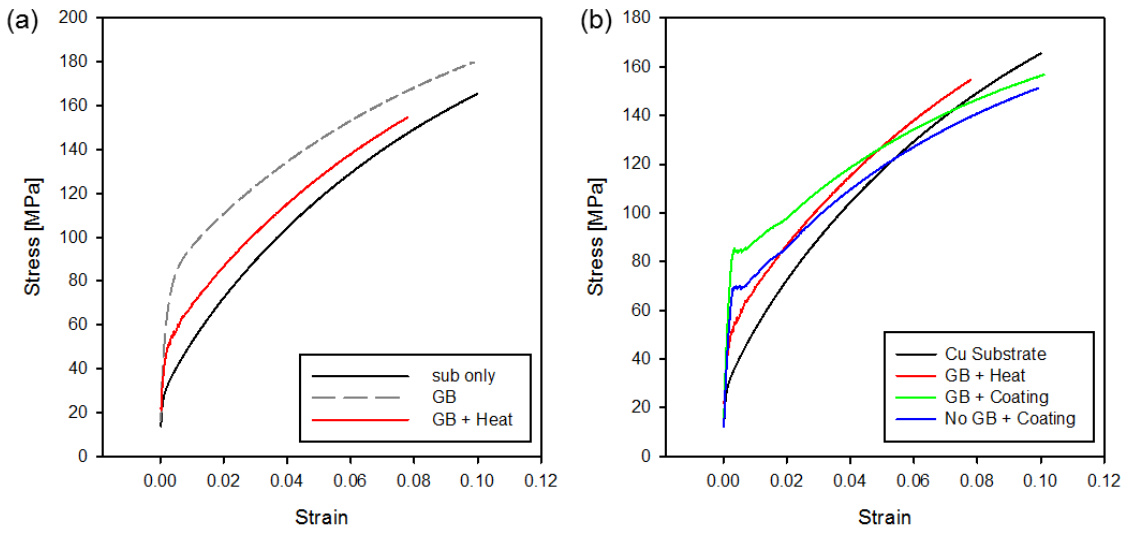

Figure 4-16 (a) Extracted stress-strain behavior for the grit blasted copper substrate after thermal softening, using the coating properties of the copper coating on the non- grit blasted substrate for subtraction. (b) Stress strain behavior adapted from Figure 4-15 including the thermally softened substrate

Figure 4-16(a) shows that a significant portion of the work hardening effect that was induced by grit blasting has been relieved, with the extracted stress-strain behavior of the substrate that has been grit blasted and subjected to the process heat lying in between that of the annealed copper and the annealed plus grit blasted copper. When this substrate property is substituted for the sample that was grit blasted prior to coating application, a more sensible difference between the coated and un-coated is seen, as shown in Figure 4-16(b). Here, both coated specimens shown improvement over their uncoated equivalent state. Figure 4-17compares the extracted coating properties between the two specimens, using the equivalent substrates shown in Figure 4-16(b) for the computation.

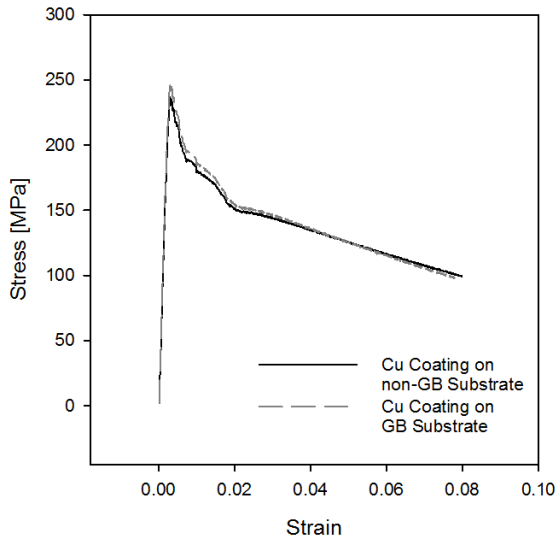

Figure 4-17 Extracted stress-strain behavior of both copper coatings using the correction of the thermally softened substrate in the case of grit blasting prior to coating application (Figure 4-16(a))

As it is seen, the extracted stress-strain behavior of the coating are very similar. Since both these coatings were sprayed in the same manner at the same time, it should be expected that their properties should be very similar, verifying this methodology and confirming that substrate work hardening relief is occurring. The copper coating shows a much higher yield stress (~250 MPa) than the substrate material, though significant drop in stress occurs quickly after yielding. The stress gradually decreases in the coating at higher stains though there is still significant strength in the coated layer.

The heat supplied to the substrate during coating application comes from the convective heat from plume and the conductive heat from the solidifying deposited particles. To ascertain the effective contribution of work hardening relief from each both heat source, a grit blasted copper substrate was subject to heating by the HVOF torch as if the coating was being deposited,

though without any powder put into the torch plume. The resulting tensile behavior is shown in Figure 4-18

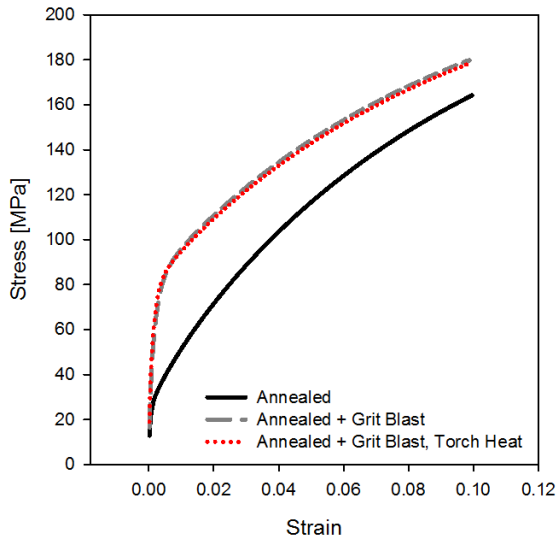

Figure 4-18 Stress strain behavior of grit blasted copper substrate that was exposed to torch heat only (no powder), with little difference from only grit blasted substrate

Very little difference occurs in the stress-strain behavior of the grit blasted specimen after heating with the torch, pointing to the conclusion that the majority of the work hardening relief of copper is due to the conductive heat from the depositing particles. Thus the amount of relief would be dependent on the thermal load of the deposit, such as particle temperature and deposition rate.

4.3.2.2 Nickel Coating on Copper Substrate

The nickel coating condition "B", established in the previous sections as being able to strengthen the overall composite structure, when sprayed onto steel, was sprayed onto an

annealed and grit blasted copper substrate for tensile testing, with the results shown in Figure 4-19. The annealed and grit blasted copper stress-strain behavior is also shown for comparison

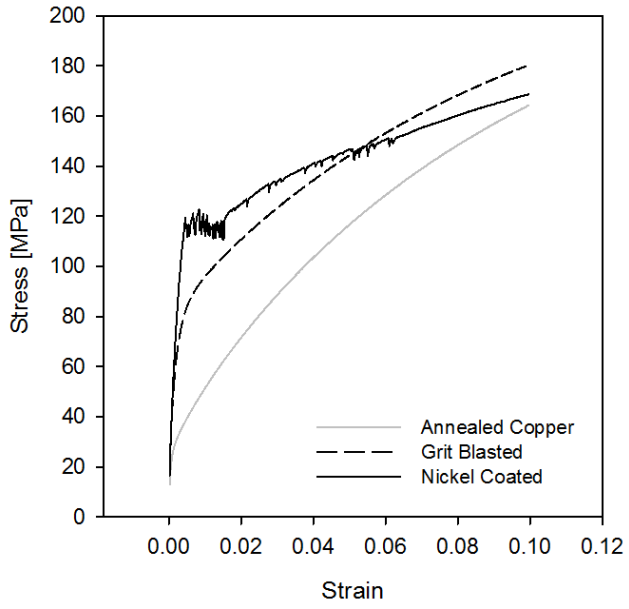

Figure 4-19 Stress-Strain behavior of Nickel coating on copper, with annealed and annealed plus grit blast for comparison

The nickel coating addition strengthens the composite structure compared to both the annealed and annealed plus grit blasted substrate. This was not the case with the copper coating, where the coating addition onto the grit blasted substrate showed weaker stress strain behavior than the grit blasted copper alone, indicating a higher strength in the nickel coating. This was due to the thermal input of the coating process relieving a portion of the work hardening induced by grit blasting in the copper substrate. The same effect can be expected here, since a significant thermal energy input can be expected from the solidifying nickel particles depositing on the substrate surface. Figure 4-20 shows the extracted coating's stress-strain behavior for the nickel

coated copper, based on the substrate behavior in the annealed, annealed plus grit blasting, and partially relieved (from Figure 4-16(a)) condition.

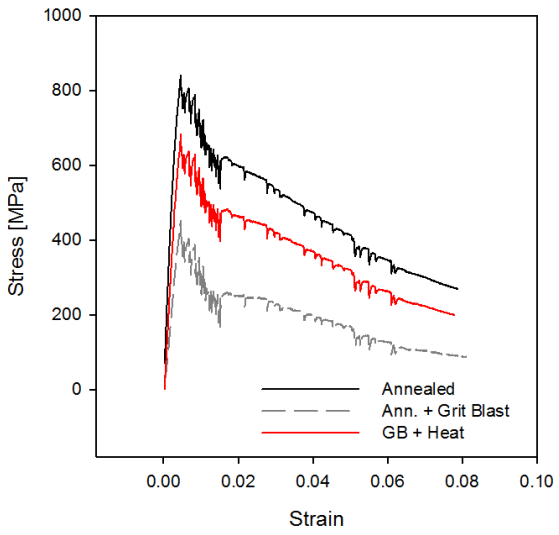

Figure 4-20 Extracted stress-strain behavior of nickel coating on copper, using the annealed, annealed plus grit blast, and thermally relieved stress strain behavior

As expected, the highest estimated coating stress strain behavior is expected when the furnace annealed copper specimens is used in the calculation and the lowest when using the annealed plus grit blasted specimen. Though it cannot be expected that the same degree of work hardening relief will be experienced with the deposit of the nickel coating as the copper coating in Section 4.3.2.1, Figure 4-20 shows some insight into the expected stress strain behavior of the nickel coating on copper substrates. No assumption of the coating residual stress has been made, though it can be expected that the coating is in a more compressive residual stress state than if on steel due copper having a larger CTE (~16.4 µm/m °C) than nickel.

The most noticeable difference between the nickel coating's behavior on copper as compared to steel (Figure 4-7) is the post yielding behavior, where dramatic oscillations in the

stress strain behavior are observed up until 2% strain, as opposed to the smooth post yield behavior of the similar coating on steel. This is not experimental noise but likely to be from unstable damage and local micro-cracking taking place in the coating. Compared with the stiffer steel substrate, the compliant copper substrate amplifies the unstable events since the coating's strength makes for a larger portion of the overall tensile specimen's strength.

4.3.2.3 Aluminum on Aluminum

When considering the tensile behavior of such TS coated composites, whether it be for repair, additive manufacturing, or enhanced surface functionality, all of the above mentioned effects of processing and substrate condition must be considered

Besides repair, the prospect of thermal spray as an additive manufacturing process holds appeal, with the high deposition rates of arc spray and cold spray being adequate for rapid deposition of material onto surfaces. However, the deposition methods, coating properties, and expected residual stresses from these process are largely different. In-Situ beam curvature measurements for deposition of arc spray and cold spray aluminum coatings deposited onto Al 6061 substrate are shown in Figure 4-21 (a) and (b) respectively

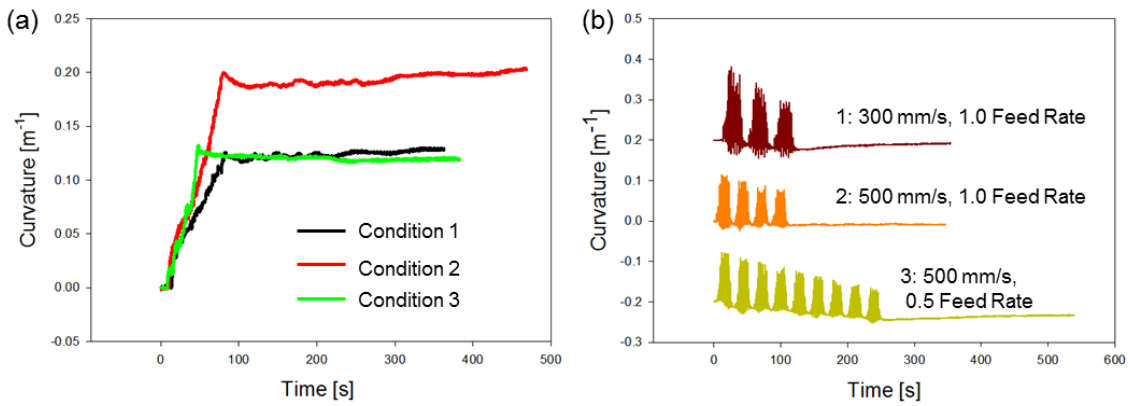

Figure 4-21 In-Situ curvature measurement of aluminum sprayed onto Al6061 Substrates by (a) Arc Spray and (b) Cold Spray

In the case of the Arc Spray (AS) deposition processes, the deposition of molten aluminum with low particle velocity produces a large degree of quenching stress during deposition, resulting in a tensile residual stress. Cold Spray (CS) deposition relies upon solid state deposition, with particle bonding dependent on adiabatic shearing upon impact as opposed to melt quenching. As such, limited quenching stresses are produced during coating deposition and a neutral/slightly compressive residual stress is produced in these coating examples.

The expected mechanical properties of these coatings are different as well. Micro-indentation of these coatings reveal how the load transfer upon compression is endured, giving an indication of the bonding between the deposited particles. The resulting indentation stress-strain using the Taber approximation [66] of these coatings are shown in Figure 4-22

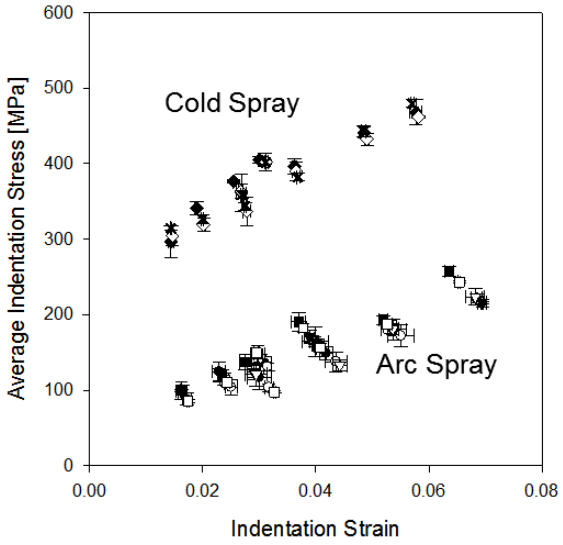

Figure 4-22 Indentation Stress Strain of the Arc Spray and Cold Spray Aluminum from Figure 4-21 using the Taber approximation

The indentation stress strain of the two coatings show considerable difference across deposition techniques, with the CS Aluminum displaying a stronger plastic deformation resistance to indentation load than the AS Aluminum. This is indicative of a mechanically stronger coating via the bonding of deposited particles, where it would be expected that the CS coating would supply more of a synergistic strength benefit to an aluminum composite than the AS coating.

Selection of a single parameter from the AS and CS samples were sprayed onto both sides of Al 6061 dogbone specimens and tensile tested in order to determine the strength of the aluminum-based composite. The load vs displacement and stress vs strain near the yield points are shown in Figure 4-23(a) and (b), respectively.

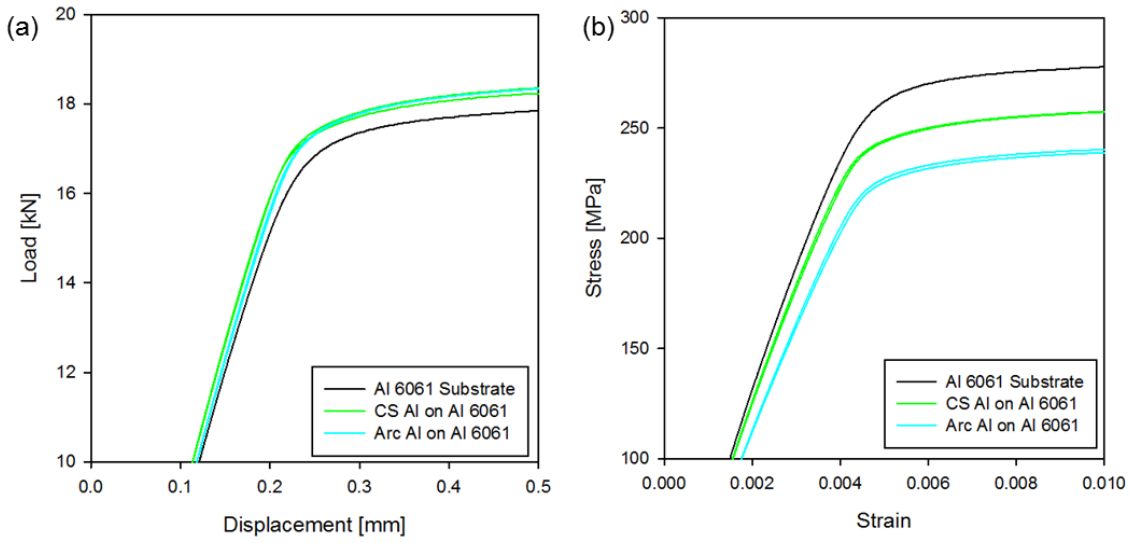

Figure 4-23 Tensile behavior of Arc and Cold spray Aluminum on Al6061 in (a) Load vs Displacement and (b) Average Stress vs. Strain

When considering the load contribution that each coating contributes in Figure 4-23(a), both coatings raise the composite's load capacity to the same yield point, which can be expected as thickness is added to the cross-sectional area of the tensile specimen. When the coating's thickness is taken into account for the calculation of average stress in Figure 4-23(b), it is revealed that the specimen's strength is actually lower than that of the bare Al 6061. The differences in the coating's contribution between the two processes is highlighted, where the weaker and tensile residual stress AS coating offers the weakest contribution to the composite. The neutral/compressive residual stress state of the CS coating, coupled with the better indentation response performs better compared to the AS coating, though it is evident that the strength of the CS coating does not match that of the Al 6061 substrate.

4.3.3 Damage Tolerant Coatings

When considering the use of TS coatings as a repair or additive manufacturing technique, the mechanical behavior of the coated composite is inherently clear as a relevant performance evaluation in order to determine the integrity of the coating. It may be less obvious to consider the mechanical behavior of a TS coated composite wherein the primary function of the coating's addition is surface functionality. However, when the composite component is subjected to load, there is a need to understand the mechanical behavior the TS coating addition can have. As mentioned in the Chapter 1, there are many instances with the applications of damage tolerant coatings where the coated component will experience loading.

Damage tolerant coatings are considerably harder than metallic coatings, though the increased hardness comes at a price of increased brittleness. Cermet materials, such as WC-CoCr, use metallic binders in order to increase toughness, but the mechanical stress-strain behavior of the coating can be expected to behave differently than a purely metallic material, such as nickel. To illustrate, a WC-CoCr coating, was applied to the same steels as the nickel coating in Section 4.3.1.8. The load-displacement and stress-strain behavior of the coated specimen is shown in Figure 4-24

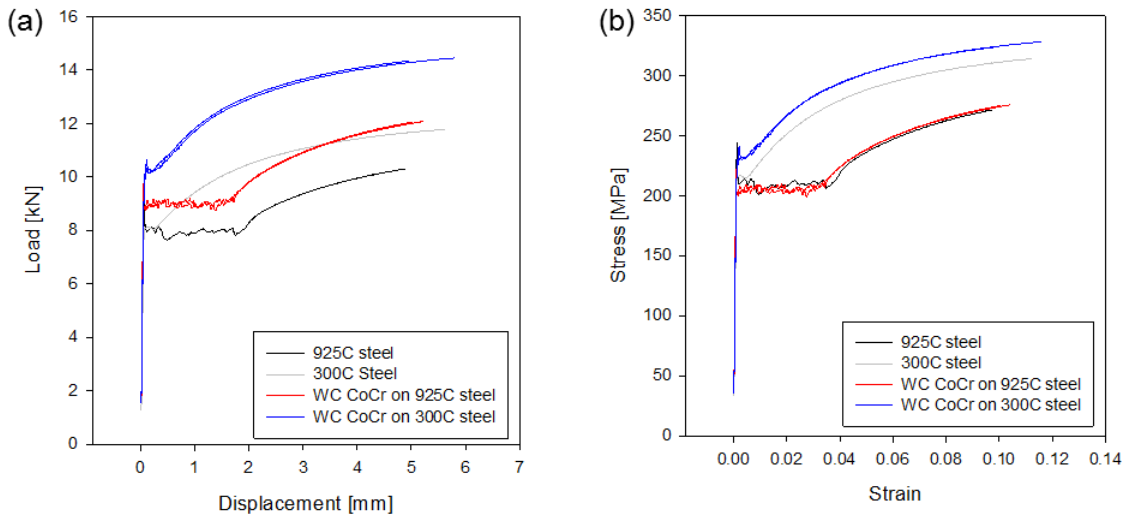

Figure 4-24 Tensile behavior of WC-CoCr coated Steel, both in the stress relieved and annealed state, in (a) Load vs. Displacement and (b) Average Stress vs. Strain

Again, the differences in the tensile behavior of the stress-relieved and annealed steel are observed, with nearly the same yield points and the annealed steel's onset of hardening occurring at a much higher strain. With the WC-CoCr coating addition, a load carrying case is observed in both cases. However, when the WC-CoCr thickness is accounted for in the calculation of average stress, the strength of the composite is nearly the same in the case of the annealed steel, with a slight increase in the case of the stress relieved steel. The extracted stress-strain behavior for these coatings are shown in Figure 4-25

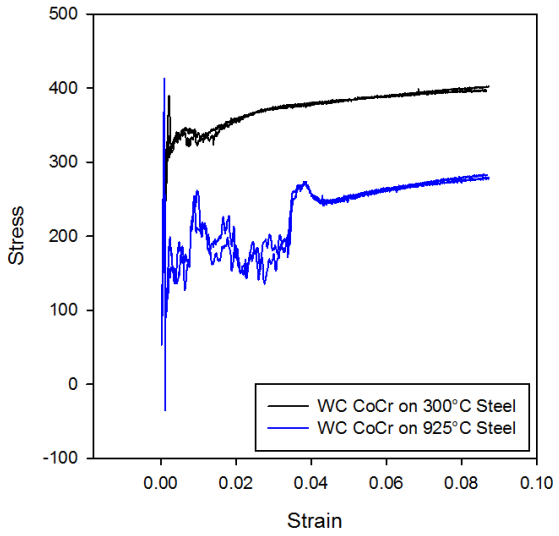

Figure 4-25: Estimated stress strain behavior of the WC-CoCr on both stress relieved and annealed steel (300°C and 925°C heat treatment, respectively)

Here it is seen that the WC-CoCr coating has a much higher stress level when on the 300°C steel, with an initial peak followed by oscillations, and even increasing after 0.01 strain when the uncoated substrate would begin to harden. The coating stress strain behavior on the 925°C steel shows a rapid peak in stress similar to the coating on 300°C steel, followed by a much larger drop and more intense serrations in the stress-strain behavior in the coating.

Besides cermets, ceramic coatings can also be employed as wear resistant surfaces due to their high hardness. However, this is a significant loss in the toughness in purely ceramics coatings, as the metallic binder material is not available to offer any ductility to the coating. Typically, there is a limited processing range where high velocity thermal spray processes can successfully deposit ceramic coatings due to limited particle dwell time, lower plume enthalpy (compared to plasma), and higher feedstock melting temperature. However, significant densities can be observed once successful deposition is achieved. HVOF alumina coatings were deposited

onto both sides of the stress relieved steel (300°C heat treatment) and tensile tested. To produce ceramic coatings with a small amount of dispersed metal within the microstructure (a pseudo-Cermet), a portion of alumina feedstock was blended with a small amount nickel powder and deposited onto tensile specimens in an attempt to raise the toughness/ductility of the coating. The results of the tensile testing are shown in Figure 4-26 , with both load-displacement and stress-strain.

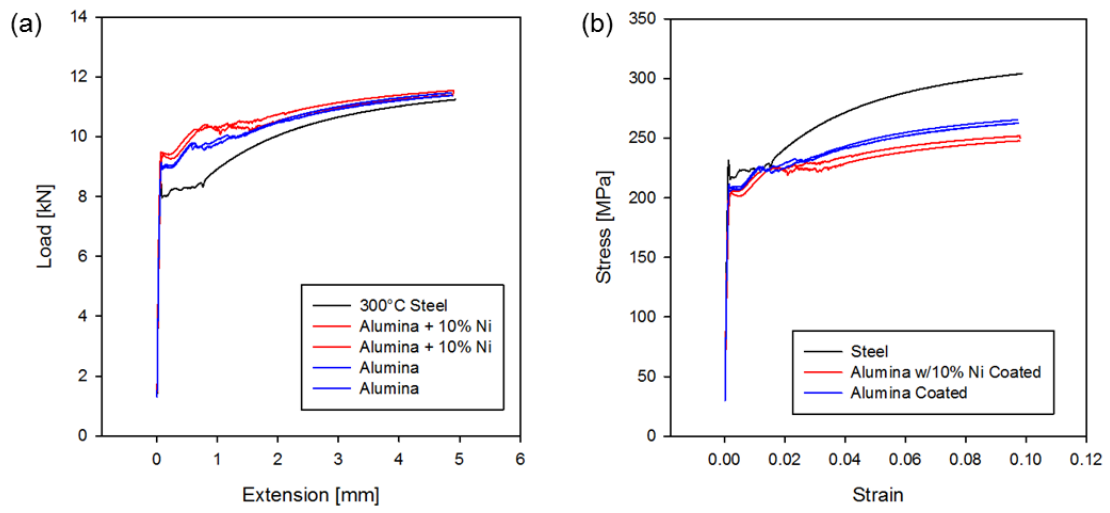

Figure 4-26 Tensile behavior of Alumina and Alumina blended with Nickel on both stress relieved and annealed steel in (a) Load vs. Displacement and (b) Average Stress vs. Strain

Again, the addition of the coating raises the load bearing capacity of the tensile specimen, with the alumina + nickel offering the greater load increase. When the thickness is accounted for in the calculation of average stress, both TS coated composites perform poorer than the steel substrate alone. This indicates that the strength and load enduring ability of the coating is very poor, likely due to the brittle nature of the alumina coating.

4.4 Discussion

The present study has investigated a potential role of metal and cermet TS coatings as load supporting components within a bi-material structure. The application of dense TS coatings onto steel can lead to enhanced strength of the existing structures due to the added metal as well as through process induced changes to the system, as seen in the case of nickel deposited onto steel. To further interpret the results, it is of importance to identify the respective contributions of the substrate (subjected to TS), the coating material and any synergistic effects of the two.

Substrate Effects

The question of how the surface preparation and coating application affect the parent material's stress-strain response requires critical examination. As shown in Figure 4-6, the stress-strain response between the coated structures made with stress relieved and as-received steel is nearly the same, though the response of the heat stress relieved and as-received steel is different. It is likely that the as-received substrates contained residual stress from manufacturing and machining, indicated by the lack of the upper and lower yield points seen in the heat-treated specimen. Latent particle heat during deposition as well as heat from the torch may have contributed to alterations to the substrate steel. Thermal camera images indicate substrate temperatures to remain below 300˚C (with spray time under ten minutes), which indicates full annealing accompanied with microstructural changes is not likely to occur, though some stress relief is possible. A mixture of residual stress in the as-received specimens, grit-blasting, and accumulation and relaxation during deposition from particle impact and cooling, respectively, may also induce the phenomenon of static strain aging in the substrate steel, though no change in yield point was observed in samples that were grit blasted and heated by the torch plume (no

introduction of powder into the plume) and is not shown. In the cases of fully annealed steel specimens, the post yielding stress-strain behavior has dramatically changed in the uncoated material as seen in Figure 4-13. Such a difference is induced only by substrate annealing and is not approached by TS coating deposition. The softening and grain regrowth, resulting in isotropic grain size and orientation (Figure 4-12), accounts for this stress-strain behavior difference, with delayed hardening after yield.

Non-ferrous substrates, such as copper and aluminum, have their own unique tensile behaviors and sensitivities to the TS process. For example, copper showed a large susceptibility to work hardening from grit blasting (Figure 4-15), a copper surface preparation method to prepare a substrate for grit blasting. The heat from the process partially relaxed this work hardening, changing the stress strain behavior of the underlying substrate within a coating-substrate composite as seen in Figure 4-16. The alterations to the copper from the TS process plays a large role in the composite stress-strain behavior, where the same coating applied to a grit blasted and non-grit blasted substrate are dramatically different. In the case of Al on Al in Figure 4-23, changes within the substrate were not investigated, but the sensitive tempering of the Al6061 substrate may be disturbed by higher temperature processes

Coating Properties and Synergistic Behavior

Based on several tests of repeat samples, the modulus of the TS nickel coating B was estimated to 120GPa while its maximum strength was estimated to be about 500MPa, which is greater than many of structural metals. The reduction of 30% in the Young's modulus is due to presence of weak interfaces (i.e., boundaries between splats) within the TS nickel coating. Since the coating is 99%+ dense, the modulus reduction due to porosity should be small. On the other hand, the maximum strength is comparable to the strength of bulk Ni. There are two scenarios

for this high stress. The rapidly solidified metal is known to comprise of fine grains, which are known to provide higher hardness and consequently higher yield strength [67]. In addition, the HVOF sprayed Ni could have finely dispersed oxides which can contribute to dispersion strengthening, though no oxide phases were detectable through X-ray diffraction measurements of Coating B. However, in this particular case, the explanation of high tensile strength lies on the "load transfer" mechanisms of coating-substrate structure. As damage initiates at some voids and/or weak interface, its progression is prevented by the local load transfer through the substrate.

No other coating material shown (WC-CoCr, alumina, or copper) demonstrated as high a strength as nickel condition B. WC-CoCr, though a hard and strong material, shows to be too brittle to accommodate load as well as the nickel. Figure 4-25 shows how the abrupt drop in coating stress strain occurs immediately after the composite yield point, though the coating layer does not drop to zero indicating some residual strength still exists. Alumina coatings, even more brittle than the WC-CoCr, do not contribute to the overall stress-strain behavior of the composite, even with a small load increase as seen in Figure 4-26. The copper coating, though ductile and displaying a smooth stress-strain drop after yield (Figure 4-17), is not as strong as the nickel coating. This can be attributed to the inherent properties of the metal, where copper is much softer than nickel

The coating stress-strain behavior is largely different for the coatings sprayed onto the fully annealed samples. The load bearing capability of both nickel and WC-CoCr coatings has been diminished with the larger degree of plasticity after the yield point of the steel, as seen in Figure 4-14 and Figure 4-25. This may be due to the inability of the coating material to accommodate the higher strain of the steel after yielding, forming cracks and damage within the

coating. The reduced ductility of the coating material with the TS processes also contributes to this phenomena.

It has been observed in all the material systems presented that an increase in load carrying capability occurs with a coating addition. However, it is more important to the designer that the composite's strength be considered, where in the processing of the coating becomes critical, since a debit in the combined strength of the coating and substrate can occur in the case of weaker coatings, as is the case in Figure 4-23. When bonding is weaker, as is the case in the alumina coated dogbones in Figure 4-26, limited load benefit is offered by the coating application, since even as the coating becomes fragmented and weaker, continued attachment to the substrate does continue to provide additional load support

Mechanism

Based on the extracted stress-strain curves of the nickel coating on various substrates, the tensile deformation of TS metallic coating on a substrate can be described in three stages, as shown in Figure 4-27(a). In the 1st stage (strains less than ~0.2%), near linear elastic response prevails (with $E \cong 120$GPa for Coating B). In the 2nd stage (strains between 0.2% and ~0.5%), some damage is initiated and progresses. If there were no substrate to transfer load, sudden failure (at the weakest site) is likely to occur during this stage. Such an event is statistical and the actual failure stress should depend on the size of specimen (i.e., a larger specimen is more likely to contain weaker sections and tends to have a lower failure load). Though not tested, failure stresses of free-standing TS nickel specimens would be in the range of 200~300MPa. With the substrate to transfer load as schematically shown in Figure 4-27(b), the nickel coating can continue to carry load although at a slightly lower modulus (~100GPa) in this stage. However once the stress reaches the yield stress of bulk nickel (~500MPa), the deformation increases

rapidly and the coating begins to fail at many locations. In the 3rd and the final stage (strains greater than ~0.5%), cracks form and the coating loses its stiffness or effectively softens, as illustrated in Figure 4-27(a). Even with cracking, as long as the nickel coating is still adhered to the substrate, it provides some residual load sharing to the overall specimen and does not fail suddenly as the case without the substrate. How TS coatings soften will depend on the (plastic) deformation behavior of substrate with different softening behaviors of TS nickel coating on different substrates

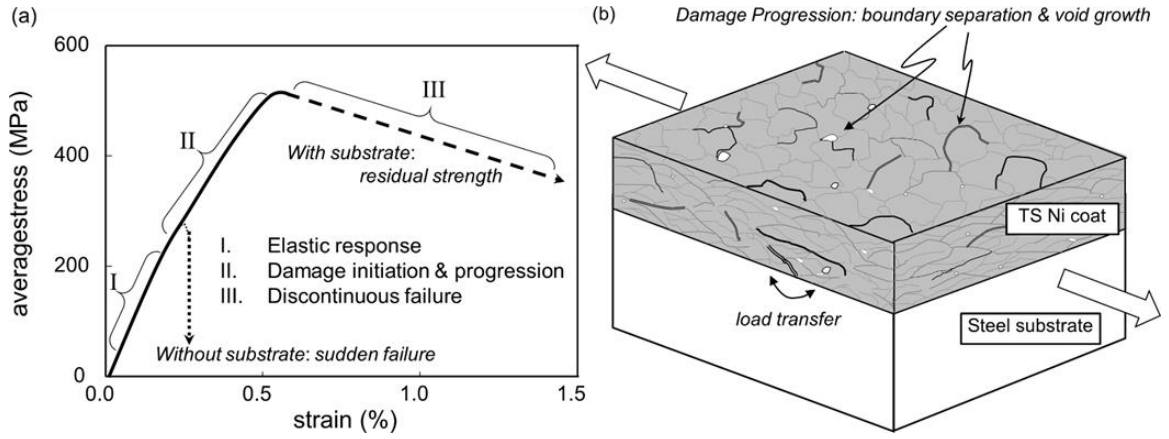

Figure 4-27 (a) Estimated three deformation stages of the nickel coating on substrate is shown in tensile stress-strain relation. (b) Schematic of load transfer mechanisms during stage II

4.5 Conclusions

The present study elucidated the mechanical behavior of high velocity TS coatings and its capacity to carry mechanical load as a bi-material structure. The synergy between coating and substrate, including the conditioning of the substrate, was also shown to be critical in composite loading. Such an understanding is needed for potential application of TS metals and cermets in uses where load bearing of the component takes place. The highest performing coating in this

study, an HVOF nickel coating, benefited from the enhanced strength and compressive residual stress imparted by the TS process. TS Ni's deformation behavior can be described in three stages. The key mechanism is the load transfer which occurs when it is deposited on to a sufficiently ductile substrate. Having the support of the substrate prevents the TS coating from failing at much lower loads. With the substrate, the maximum strength of TS Ni reaches near the strength of bulk Ni. It is expected that other near fully dense metallic coatings have similar deformation stages as introduced here, such as the copper coating which was discussed. Harder and more brittle coating materials, such as WC-CoCr and alumina, suffered from their lack of ductility and lost load carrying strength at a faster rate than that of the metallic coatings. However, the WC-CoCr coating studied, with metallic binder for increased toughness, outperformed the alumina coating in synergistic strengthening of the coating-substrate system.

Although only tensile behaviors were examined here, the compression behavior of the TS coating is expected to be different, especially at large strains. The softening behavior may not occur under compression. Since many of engineering structures are subjected to compression (e.g., bridges, buildings, landing gear), investigation of TS coatings under compression is clearly needed and should be studied in the future

.

5 Structural Integration of High Velocity Thermal Spray Coatings Part II: Cyclic Mechanical Behavior of TS Coated Specimens

5.1 Introduction

In the design of a component in normal service life, the loads applied to the material are meant to be well below the yield strength in order to ensure safe operation and to prevent premature failure. However, cyclic loading over long periods of time below the yield point can still accumulate damage within the material, leading to eventual failure by the mechanism of fatigue. Fatigue occurs when cyclic loading of a material gradually moves dislocations to the edges of grain boundaries and surfaces, inducing microscopic roughness. This roughness leads to a local stress intensity which are higher than the overall body, which may eventually initiate a crack, known as a "*fatigue crack*". With further cycling, the stress intensity near the crack drives the crack growth in accordance with Paris' law up until the point of sudden failure [68]. For ferrous materials, there generally exists a minimal stress amplitude where fatigue failure will not occur with more cycles, known as the "*endurance limit*", which generally is accepted at 10^7 cycles of loading without failure for ferrous materials. Some non-ferrous materials, such as Aluminum alloys, never reach a true endurance limit and are designed with this in mind. With the awareness of such fatigue phenomena, the design of cyclically load bearing parts takes precaution to avoid fatigue failure by using adequate material and dimensions to keep the

expected stress below the endurance limit or within a safer operating range. In addition to the intrinsic fatigue resistance of materials, surface modifications can be employed to delay or reduce the likelihood of fatigue crack initiation and growth, such as reducing surface roughness through finishing, inducing compressive residual stresses such as shot peening, and other methods of surface hardening (nitiriding, carburizing, remelting)[69-72].

The incorporation of a TS coating in the design of a load bearing component would require assurance that the effects of the coating's presence and processing will not incur a debit to the fatigue life of the component. Preferably, coating addition would have an increase in the fatigue life while maintaining surface functionality. The prospect of enhanced fatigue life is very appealing, where multi-functional added value to the part through TS processing would allow for higher performing components. Incorporating surface functionality and fatigue/mechanical integrity requires in depth understanding of the factors that determine coating properties and performance, as well as the interplay between the coating and substrate as well as the behavior of the substrate independent of coating application. Figure 5-1 highlights these location based demands of a structurally integrated coating.

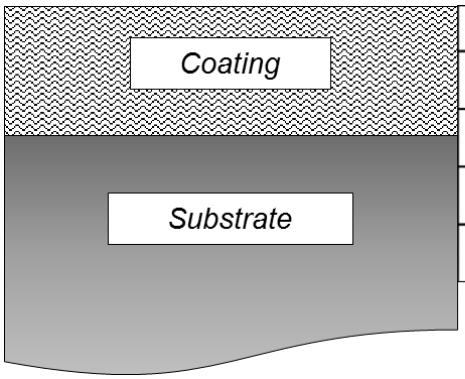

Region	System Requirement
Coating Surface	Functionality
Coating-Substrate Interface	Adhesion
Substrate Sub-Surface	No Fatigue Debit
Bulk Substrate	No Structural Debit

Figure 5-1 Location specific functionality of structurally integrated TS coatings

Numerous academic fatigue studies of TS coated specimens have been carried out, though no common consensus on whether an enhancement [7-10] or debit [7, 11-14] in fatigue life is generated with coating application. Since TS coating properties are highly dependent on the processing parameters used [5, 15], an assessment with one coating process parameter does not offer a complete picture on the fatigue of TS coated specimens [13, 16]. With parametric studies of coating processing, it has been reported that the residual stress state of the coating has a large influence on the relative fatigue life of coated specimens [12, 16, 17], as well as coating properties such as coating toughness [10]. The presence of residual stresses throughout a material prone to fatigue loading has been considered a critical factor for the fatigue life of uncoated components as well [18, 19], as the superposition of the applied stress and residual stress throughout a fatigued body leads to local stress intensifications. Such stress intensifications are then prone to fatigue crack initiation and growth as described by Paris' Law [20]. Other investigations into the effect of substrate preparation prior to coating deposition, such as shot peening or grit blasting, have also been studied as residual stress contributors in attempts to mitigate fatigue debits incurred by coating application [11] or to isolate the coating's influence on fatigue life [7].

Property and Stress Based Approach to Fatigue Life

As described in Section 3, the role of particle state resulting from feedstock material, torch type, and torch operating parameters play a large role in determining the properties and performance of damage tolerant coatings. Most importantly, there are large differences in the formation and residual stress within the coating. The force resulting from these stresses are also balanced through a stress profile within the substrate as well. The presence of residual stresses throughout a material prone to fatigue loading has been considered a critical factor for the fatigue life of uncoated components [70, 72] as the superposition of the applied stress and residual stress throughout a fatigued body leads to local stress intensifications. In addition to the residual stresses inherent in thermal spray coatings, the properties involved in coating load bearing (modulus, yield strength) have also been demonstrated as being controllable via particle state manipulation as seen in Section 4. Thus the control of torch operating parameters and particle state have the ability to manipulate the load bearing capability of TS coatings, as well as the residual stress state through coating formation stresses.

Residual stresses within the substrate and coating of a TS coated specimen can also arise from sources other than the state of depositing particles. The thermal stress, arising from thermal expansion mismatch strain ($\varepsilon=\Delta\alpha\Delta T$), can also contribute significantly to the residual stress state of a coating-substrate, particularly when the thermal mismatch between the two is large or a relatively high deposition temperature is expected. Since deposition rates, pause time between passes, part size and geometry, and directed cooling are all variables in TS coating application, the managing or exploitation of thermal stresses can also be used as a tool to alter the residual stresses in a coating-substrate system.

Since surfaces are prone to large stress intensification due to roughness, it is important to note that typical substrate surface preparation for TS may also induce alterations to the residual stress state, and thus fatigue life, of the specimen. Such preparations include grit blasting, a common preparation technique to enhance the mechanical bonding of the coating to the substrate, induce compressive residual stresses into the surface, as well as grain distortion and surface roughening, which can have implications on fatigue behavior. Fatigue prone surfaces can also be treated with processes such as shot peening that intentionally induce compressive residual stresses, which are well known to delay surface fatigue crack initiation and growth at the substrate surface [70, 73, 74]. Any introduction of stresses into the substrate prior to coating application will also have effects on the fatigue life of a TS sprayed specimen.

Finally, the fatigue behavior of the substrate has a large role in the how the coated component will perform, due to the majority of the structure being comprised of the parent material. As such, considerations of the substrate modulus, strength, toughness, and composition will have dominating roles in the fatigue life when mated with a coating. Additionally, the fatigue life of the substrate alone is what any coated substrate will be compared to, as designers account for the relative differences that coating application can have on the part and decide on its implementation. However, there is also the need to consider the interplay that can occur between the coating and substrate during coating deposition if different substrate choices are considered for design, such as adhesion strength and thermal expansion mismatch induced stresses, as well as the load sharing capabilities between the substrate and coating, such as modulus and strength differences

5.2 Experimental Methods

5.2.1 Feedstock and Spray Parameters

Several sets of experiments were conducted wherein the role of particle state, thermal stress, substrate preparation, and substrate type on fatigue life of TS coated specimens were examined. All coatings were sprayed with a JP-5220 spray system (Praxair Surface Technologies, Indianapolis, IN), a liquid fuel HVOF torch. Selection of operating parameters were based on both manufacturer recommended conditions, as well as variations from experimental work. Feedstock material used included the commonly employed damage tolerant coating compositions of CrC-NiCr and WC-CoCr, though several powder morphologies were used for specified tests. All powders used were commercial varieties, selected from Table 3-1. The spray conditions (and powder used) for each fatigue specimen is shown in Table 5-1

Condition	Material	Powder	Kerosene [L/hr]	Oxygen [SLPM]	Barrel [mm]	Spray Distance [mm]	O_2/Fuel	Combustion Pressure [MPa]	Coating Thickness [µm]
1	CrC-NiCr	sx 195	18.9	648	152	406	1	0.52	110
2	CrC-NiCr	sx 195	23.5	1009	152	406	1.26	0.79	110
3	WC-CoCr	WOKA 3652	20.0	623	152	305	0.91	0.50	220
4	WC-CoCr	WOKA 3652	28.0	858	203	305	0.89	0.72	160
5	WC-CoCr	Amperit 556	22.7	778	203	279	1	0.61	150
6	WC-CoCr	Amperit 556	18.9	651	102	381	1	0.50	150
7	WC-CoCr	Amperit 556	18.9	873	152	381	1.35	0.62	150
8	WC-CoCr	WOKA 3652	23.5	969	152	330	1.23	0.73	165
9	WC-CoCr	WOKA 3652	24.6	943	152	330	1.12	0.74	120

Table 5-1 Sprayed conditions and associated powder for coating used in fatigue testing

5.2.2 Measured Particle State

Inflight particle properties (average temperature and velocity) were measured using an Accuraspray G3 ™ (Tecnar Automation LTEE, St-Bruno, QC, Canada). Measurements were made prior to coating deposition at the stand-off distance of the would-be surface, with the average of more than 10 seconds of recorded data used for reported values.

5.2.3 Coating Stress Characterization

Coating stress calculations were made through the measurement of in-situ beam curvature, with stress values calculated using the Stoney formula [11, 75]. Substrate temperature was concurrently measured via contact thermocouples on the substrate back side. Spray patterns on the beam were altered in order to alter substrate temperature in several cases. Pause time between the strokes was also changed for temperature manipulation. Schematics of the difference between "box" and "ladder" rastering programs are shown in Figure 5-2

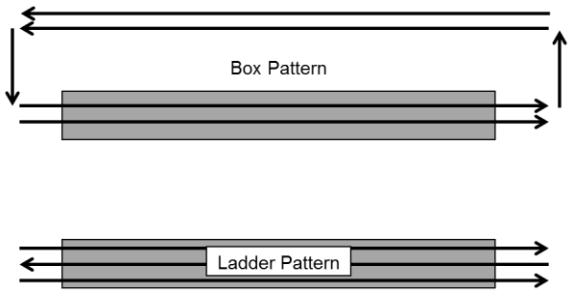

Figure 5-2 Deposition patterns used on the in-situ beam curvature measurement device in order to alter substrate temperature

5.2.4 Coating Property Measurements

5.2.4.1 Vickers Hardness

Vickers hardness of the coatings was measured on mounted and polished cross sections at a load of 300g for 15s. Measurement of the indent diagonals were performed using optical microscopy.

5.2.4.2 Indentation Modulus

Indentation modulus measurements were taken on the top surfaces of polished coatings using an instrumented indenter with a Berkovich tip (Micro-Materials Limited, Wrexham Technology Park, Wrexham, UK). Elastic recovery of the coating upon unloading was used to calculate the indentation modulus, as described by Oliver and Pharr [36]

5.2.5 Fatigue specimen preparation

Rotating Bend Fatigue (RBF) specimens were machined out of cold drawn 1018 steel to the nominal dimensions shown in Figure 5-3. All samples were annealed within a vacuum furnace at 900°C for a dwell time of 2hrs and allowed to cool within the furnace to ambient temperature in order to remove work hardening and reduce the cold drawn grain structure within the steel to produce a stress free steel. Titanium 6Al 4V (Ti64) samples were not heat treated and were sprayed in the as received condition.

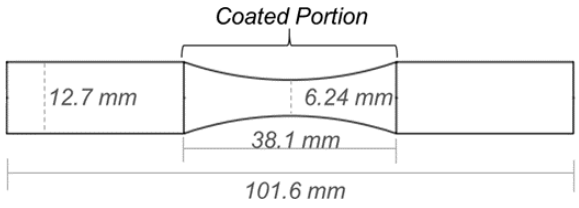

Figure 5-3 Rotating bend fatigue specimen nominal dimensions, with portion coated by WC-CoCr indicated.

The planar steel beams, cylinders, and selected RBF samples were grit blasted using an alumina grit. Samples were cleaned in an acetone bath with ultrasonic agitation for cleaning prior to coating deposition to ensure no trapped grit would be included in the coating-substrate interface. Select RBF samples were shot peened in a similar manner, using the same grit blasting equipment with steel shot replacing the alumina grit.

Samples were coated in a manner shown schematically in Figure 5-4, with sample spinning at a constant rotation (600 RPM) and the torch slowly rastering (50mm/s) down the neck region of the samples. Raster speed of the torch was used so that one full turn of the sample would correspond with a vertical travel distance of 5mm (the same used between coating strokes on planar samples when using the JP torch). Shields and masking were used to eliminate overspray onto the non-neck portions of the sample.

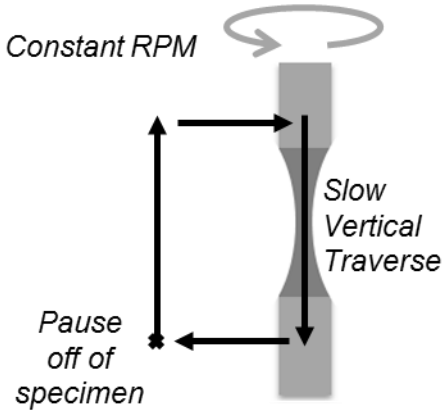

Figure 5-4 Torch view schematic of coating technic used for RBF and uni-axial fatigue specimens, with rotation of the specimen and vertical traverse down the neck of the sample

5.2.6 Temperature Measurements

Surface temperature of the necks of the RBF samples during spraying were monitored by an IR thermal camera (FLIR Systems, Wilsonville, OR), with manipulation of the temperature being accomplished by robotically varying the time between coating strokes on the samples.

5.2.7 Rotating Bend Fatigue Testing

Fatigue testing was performed using a RBF-200 model rotating beam fatigue testing machine (Fatigue Dynamics Inc., Dearborn MI, now System Integrators LLC, Glendale AZ). Samples were tested at a frequency of ~100Hz, under fully reversed loading (R=-1), at varying applied moments until failure or severe deformation triggered the motor's cutoff switch while the cycle counter recorded the number of cycles to failure. No grinding or polishing of the substrate or the coating after deposition was done in order to not alter the roughness of the coating after deposition. Micrographs of fatigue fracture surfaces were taken using either an optical stereoscope or SEM in backscatter mode.

Select RBF testing (4340 Steel substrate samples) was performed by Darmstadt Technical University in Germany, under Prof. Dr.-Ing. Brita Pyttel. Similar testing procedures were used as those in CTSR, though coated samples were ground and polished with SiC paper to desired thickness prior to testing. Figure 5-5

Figure 5-5 Image of RBF specimen for 4340 Steel samples with dimensions labeled

5.2.8 Uniaxial Fatigue Testing

Uniaxial fatigue testing was conducted with a servo hydraulic tensile testing machine (Instron 8800, Norwood MA) with a 200kN static and 100kN dynamic load cell. Deflection was measured with a clip-on extensometer (with resolution of ~1μm) with the clips placed 12.5mm apart. Fully reversed (R=-1) testing at a rate of 5Hz was conducted until specimen failure or elongation larger than the extensometer range occurred.

5.2.9 Coating Stripping

WC-CoCr coating stripping was performed using a solution of Potassium Sodium Tartrate (Rochelle salt) and Sodium Carbonate in distilled water at concentrations of 50 g/l and 150 g/l, respectively. A D.C. voltage of 3-4 volts was applied to the sample and an immersed steel electrode, producing a current of 1-1.3 Amps. The solution was continuously stirred and keep ~60°C during the stripping process, with periodic light brushing of the coated area to expedite the stripping process. After coating removal, the RBF samples were washed with distilled water and dried prior to fatigue testing. Similar procedures have been used to effectively strip WC-CoCr coatings [76, 77]

5.3 Results

It should be noted that in order to calculate a stress amplitude value for the surface of the RBF specimens, the increase in specimen diameter due to coating thickness is treated as if the coating is identical to the substrate, which is not an ideal assumption. However, in the case of most coated component design, the coating is not treated as a load carrier but its thickness is taken into the measurement of the part's geometry. Thus all stress amplitudes on the fatigue specimens are reported as if composed of the substrate alone.

5.3.1 Role of Torch Parameters and Particle State.

As discussed in Chapter 3, the operating conditions of an HVOF torch will have significant influence on the thermal and kinetic energy state of a particle. This in turn will affect the coating formation behavior and the properties of the coating. These properties (e.g., residual stress, modulus, hardness) have an influence in the fatigue life of HVOF coated specimens, as will be demonstrated.

5.3.1.1 Rotating Bend Fatigue of CrC-NiCr on 4340 Steel

Though there are differences in spraying on flat specimens vs round specimens for fatigue testing, the qualitative trends in properties can be assumed to be similar based on what was observed in planar specimens. The first example of this is the stress and properties of two CrC-NiCr coatings that were sprayed onto an in-situ beam curvature device using the conditions 1 and 2 in Table 5-1. These spray parameters produced two largely different stress states and coating properties, measured from samples taken from the coated beams. The measured particle state and planar evolving and residual stresses are shown in Figure 5-6 (a) and (b) respectively. Here it is seen that the manipulation of particle state strongly influences the evolving stress and residual stress of the coating, where the difference between a quenching and peening evolving stress has been demonstrated simply through torch parameter manipulation. The hardness and indentation modulus of these two coatings, referred to as “neutral” and “compressive” due to their expected residual stresses, are shown in Figure 5-7. Here it is seen that the coating with compressive residual stress has both higher hardness and indentation modulus as compared to the neutral coating. These differences in stress and properties are expected to play a large role in the fatigue life of the coated specimens.

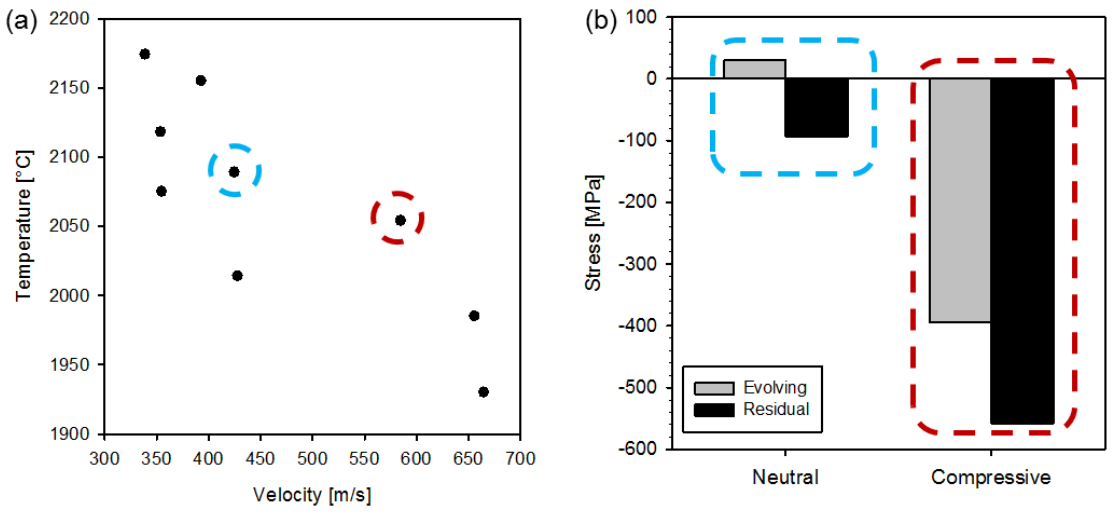

Figure 5-6 (a) Temperature and Velocity of CrC-NiCr sprayed by LF-HVOF with selected coating conditions used to spray onto fatigue specimens. (b) Evolving and Residual stress calculations from in-situ beam curvature measurement of the conditions shown in (a)

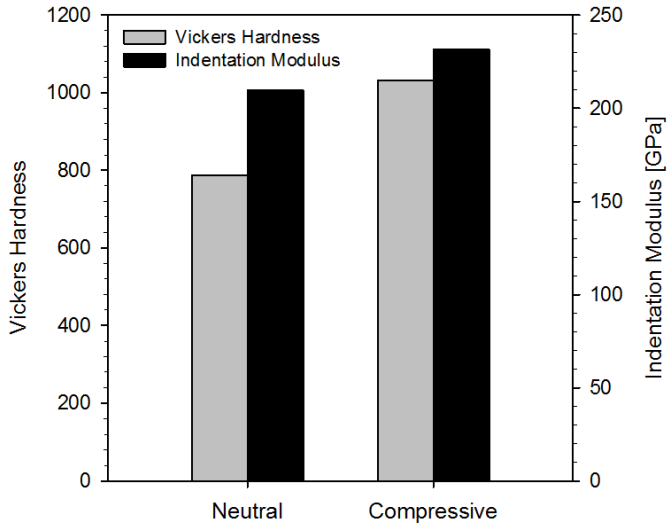

Figure 5-7 Measured properties on the planar samples of the "neutral" and "compressive" CrC-NiCr samples

These conditions were then sprayed onto 4340 steel RBF specimens, with deposition rates and cooling arrangements kept constant for the two conditions. After grinding and polishing, the RBF specimens were then tested until failure or runout (>10^7 cycles without failure). Uncoated and grit blasted only specimens were tested as well to compare the relative differences. The SN graph of these samples are shown in Figure 5-8

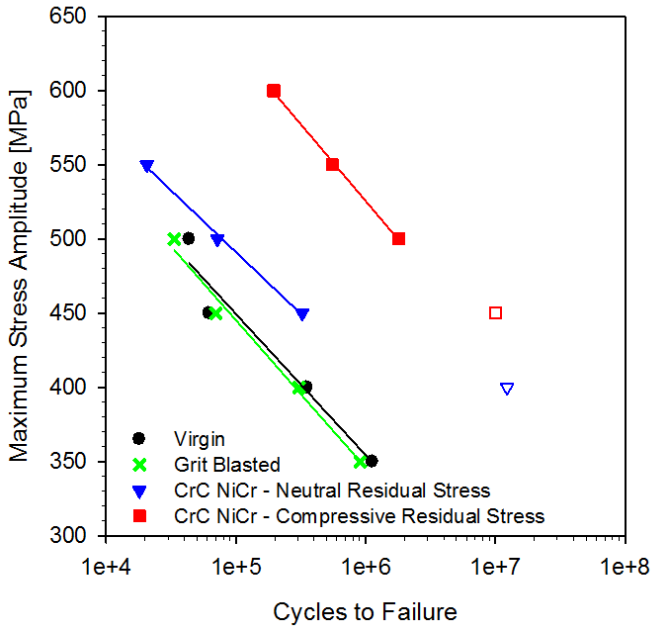

Figure 5-8 Stress Amplitude vs Cycles to failure for CrC-NiCr coated 4340 steel, with the bare and grit blasted substrate shown for comparison. White filled samples indicate run out

It can be seen that the coating with a higher amount of expected compressive residual stress and stronger mechanical properties outperformed the coating that was expected to have a nearly neutral residual stress and weaker mechanical properties. Both coated specimens outperformed the bare and grit blasted substrates, offering a synergistic benefit to the fatigue life of the specimens through coating addition. Grit blasting did not appear to influence the fatigue life of the bare substrate.

5.3.1.2 Rotating Bend Fatigue of WC-CoCr on 1018 Steel

Similar characterization involving WC-CoCr was done, where manipulation of torch operating parameters were able to produce different particle states, as conditions 3 and 4 shown in Table 5-1. Depositing these conditions onto steel beams with simultaneous curvature measurement was used to calculate the different evolving and residual stresses for the particular conditions shown in the Figure 5-9

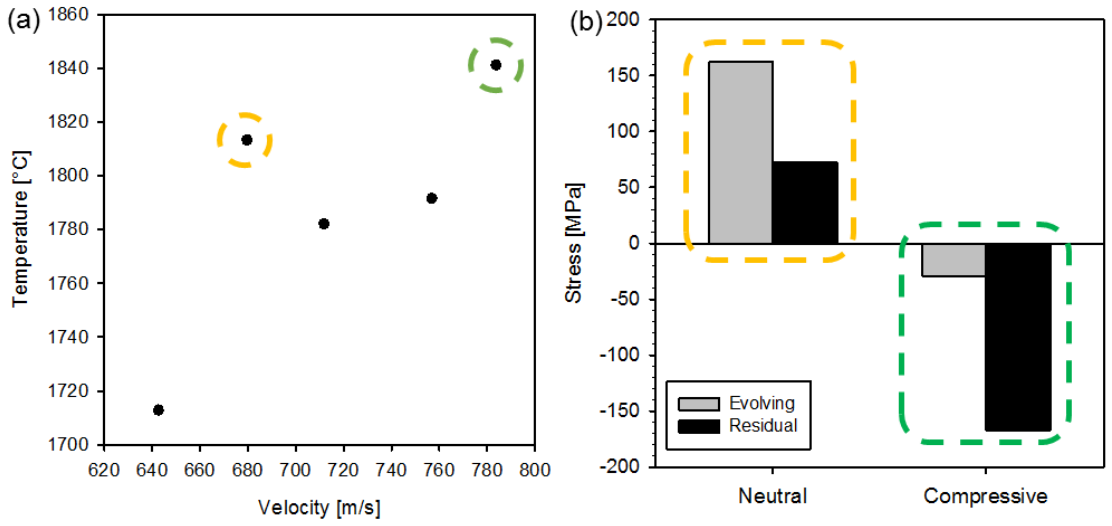

Figure 5-9 (a) Temperature and Velocity of WC-CoCr sprayed by LF-HVOF with selected coating conditions used to spray onto fatigue specimens. (b) Evolving and Residual stress calculations from in-situ beam curvature measurement of the conditions shown in (a)

Again, it can be seen that the particle state has a strong influence on the evolving and residual stress. In this case, net compressive evolving stress is not observed, in contrast with the second CrC-NiCr deposits shown in Figure 5-6(b). Hence the compressive residual stress here is primarily a result of the thermal mismatch stress between the steel and WC-CoCr coating.

These two spray conditions were then sprayed onto as received (cold drawn) 1018 steel RBF specimens, where deposition parameters of cooling and surface speed were kept constant, though different from the CrC-NiCr samples. Again, uncoated and grit blasted only specimens were tested to observe the relative comparisons. The results are shown in Figure 5-10

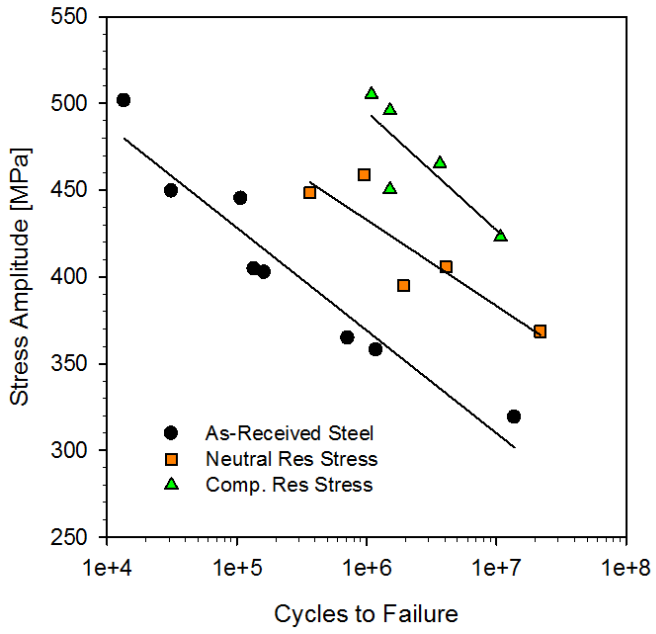

Figure 5-10 Stress Amplitude vs Cycles to failure for WC-CoCr coated 1018 steel under the two conditions shown in Figure 5-9(a), with the bare substrate shown for comparison.

It is seen that the coating with a higher expected magnitude of compressive residual stress offers the greatest improvement in specimen fatigue life. The coating with an expected neutral residual stress also yields a benefit to the fatigue life, but to a smaller amount than that of the compressive coating. Both coatings do offer improvement to the overall fatigue life of the component, similar to the case of the CrC-NiCr coated samples.

5.3.1.3 Uniaxial Fatigue of Alternative WC-CoCr and 1018 Steel

An alternative feedstock material of WC-CoCr, with a smaller particle size and finer carbide size, was subjected to a variety of torch operating parameters that produced different particle states (conditions 5, 6, and 7 in Table 5-1. More uniquely than the WC-CoCr in Section 5.3.1.2, the evolving stress of the fine carbide WC-CoCr was much more manipulate-able via torch operating parameters, offering a wider menu of stresses within the coating. Curvature vs. time measurements of three selected coating conditions are shown in Figure 5-11(a), where the resultant coating residual stresses on the planar beam result in coatings with tensile, neutral, and compressive residual stress. It is noted that the most compressive residual stress coating also has a negative evolving stress, indicating the dominance of peening in the coating's formation. Hardness measurement of the coatings shown in the Curvature vs. time plot are also included in Figure 5-11(b) where the compressive coating has a higher hardness than the other two coatings.

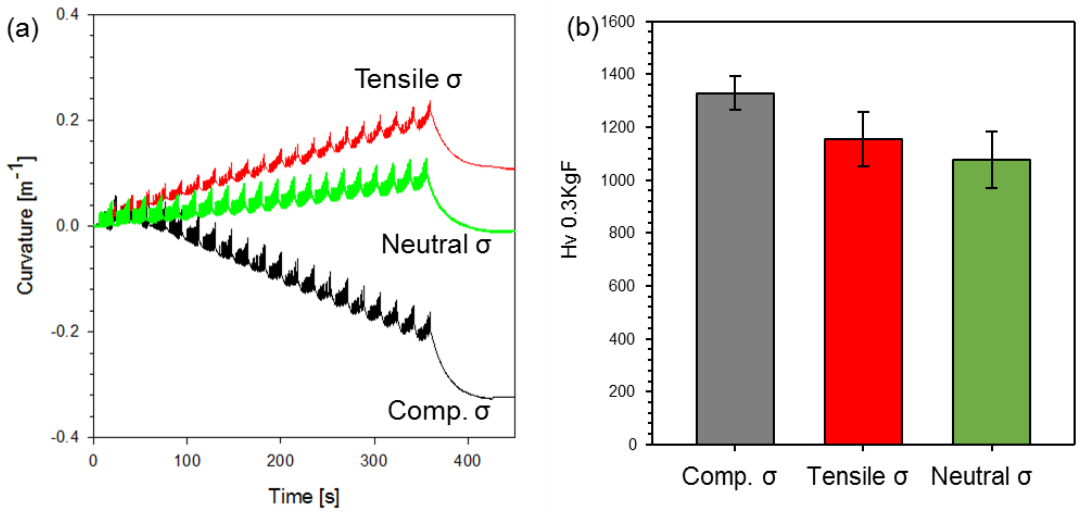

Figure 5-11 (a) Curvature evolution of three torch conditions spraying fine carbide WC-CoCr (Amperit 556) resulting in a tensile, neutral, and compressive residual stress state and (b) measured cross sectional Vickers hardness of the three coatings in (a)

These coatings were then applied to the specimen geometries shown in Figure 5-5 and fatigue tested in the uniaxial direction until failure. The results of this fatigue testing is shown in Figure 5-12, as well as uncoated, as received 1018 steel samples

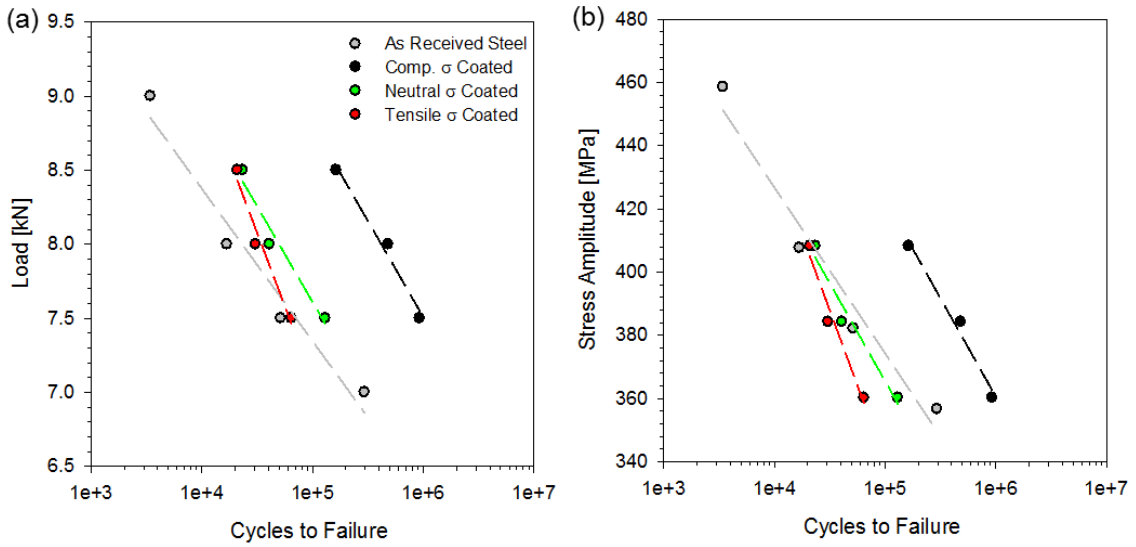

Figure 5-12 Uniaxial fatigue behavior of 1018 steel coated with the conditions in Figure 5-11 in (a) Load vs cycles to failure and (b) average stress amplitude to failure

When considering the fatigue strength simply as the uniaxial load, all coated specimens show some benefit to the fatigue life, particularly the compressive stress coating. However, as cross sectional thickness is added to these specimens, it would be intuitively expected that the load enduring capability of the entire specimen would increase, thus not making as rich of an assessment of the integrated fatigue resistance of the specimen. When taking the additional cross-section into the account for an average stress (average due to differences in the moduli and Poisson ratios), it becomes clear to see that the compressive residual stress WC-CoCr coated specimen is the only sample to gain a fatigue life credit.

Due to such phenomena as static strain aging [78] or the possible softening or stress relief of the substrate as seen in Section 4, the question of how the process influences the fatigue life of the steel base material was preliminarily investigated. Steel samples were grit blasted and subjected to the torch heat without any powder in the same manner as if coating were to be deposited. These steel samples were then fatigue tested, with results shown in Figure 5-13, comparing the relevant sample with a coating by the same condition.

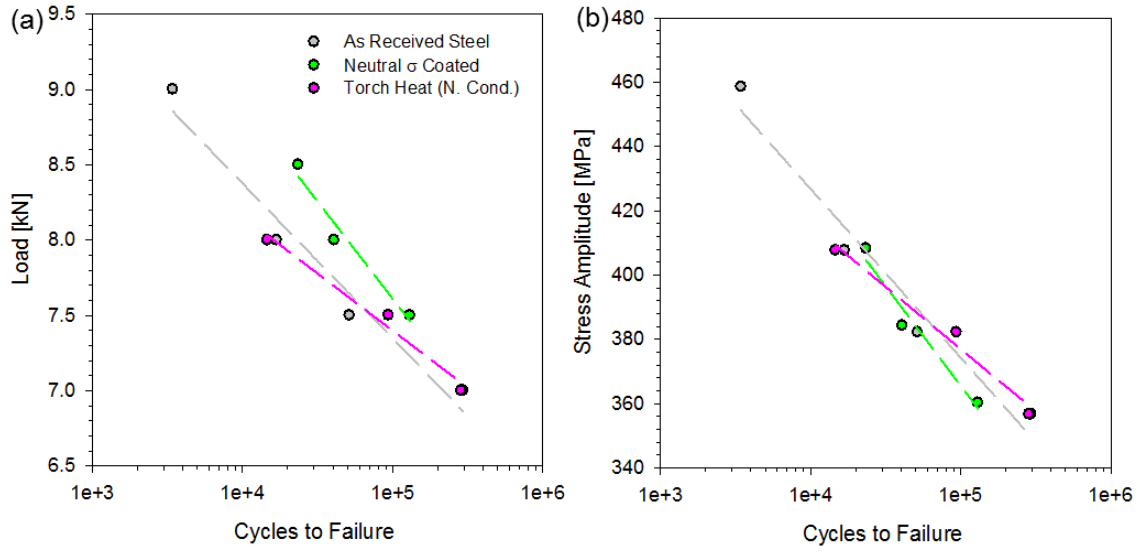

Figure 5-13 Uniaxial fatigue behavior of 1018 steel with the neutral residual stress condition WC-CoCr and the samples only exposed to the heat from the torch in (a) load vs cycles to failure and (b) average stress vs cycles to failure

There appears to be no significant difference in the fatigue life of the base material as compared to the grit blasted and torch heated sample. Thus, it can be said that grit blasting and the convective heat supplied by the torch did not greatly alter the fatigue behavior of the base material. This emphasizes the influence of the coating processing, namely the particle state and

resultant evolving and residual stresses, on the relative fatigue life of the WC-CoCr coated steel tested in uni-axial fatigue.

5.3.2 Deposition Parameters and Thermal Stress

5.3.2.1 Thermal Stress Manipulation

In order to assess the magnitude of difference in residual stress that can be achieved by deposition conditions (i.e., pause time between coating strokes) as opposed to different particle states, beam curvature measurement was used to monitor the deposition of WC-CoCr. Substrate temperature was manipulated by changing the amount of pause time between coating strokes using robotic programing while spraying condition 9 from Table 5-1. The measured and smoothed curvature-time behavior for the deposition and cooling of the WC-CoCr coatings sprayed onto low carbon steel planar beams are shown in Figure 5-14(a), with deposition and cooling regimes noted. Values for the deposition, thermal, and resultant residual stress calculated by the measured curvature with the Stoney formula are shown in Figure 5-14(b), using the curvature points indicated in Figure 5-14(a) The average back side substrate temperature stabilized at approximately 350°C for the High Temperature (HT) coating and 200°C for the Low Temperature (LT). As such, a larger compressive thermal stress is produced in the HT coating by the higher deposition temperatures and the substrate having a larger coefficient of thermal expansion than the coating. Both coatings had a similar deposition stress, making the residual stress primarily different by the thermal stress component.

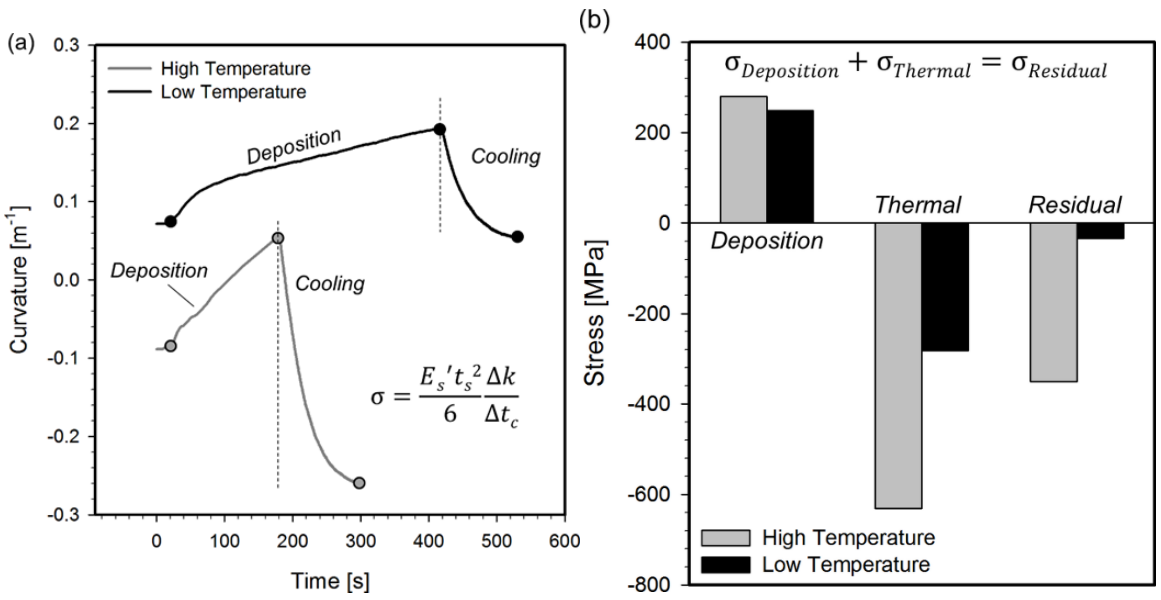

Figure 5-14 (a) Measured beam curvature during the deposition and cooling of the WC CoCr coatings on steel with both short and long passes between successive coating strokes and (b) calculated deposition, thermal, and residual coating stresses from curvature measurements

To assess the mechanical property influence from deposition parameter manipulation, hardness and indentation moduli of the two coatings from Figure 5-14(a) and (b) were measured and are shown in Figure 5-15(a), where it is seen that the coatings properties have been slightly influenced by the time between deposition strokes. Changing the specimen geometry while keeping similar deposition stroke timing to that of the RBF samples, steel and aluminum cylindrical samples of 12.7mm diameter were sprayed in order to assess the influence of coating-substrate CTE mismatch on coating hardness, with results shown in Figure 5-15(b). Also included in the Figure is a 25.4mm diameter steel sample sprayed in the same manner in order to give an indication of surface speed effects. Though higher hardness than the planar samples was measured, the relative difference in coating hardness with pause time (and thus substrate temperature) show subtle yet consistent differences in the coating hardness on the cylindrical samples, with little influence from the substrate's CTE or diameter.

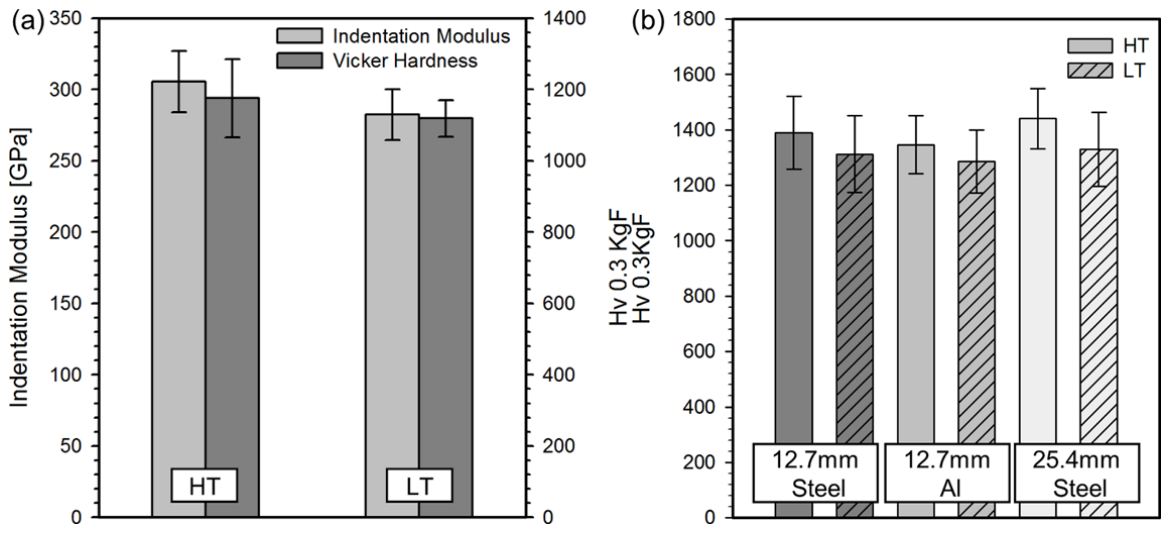

Figure 5-15 (a) Indentation modulus and cross section hardness of the short and long pause coatings on the planar steel beams shown in Figure 2(a). (b) Cross section hardness of coatings deposited on different cylindrical substrates with both short and long pause time.

Control of the surface temperature on the RBF samples during deposition via deposition stroke timing produced two coatings, referred to henceforth as Low Temperature (LT) and High Temperature (HT) coatings. IR measured surface temperatures during LT and HT deposition were approximately 50°C and 150°C, respectively, at the beginning of each coating stroke. In order to avoid the complexities in fatigue behavior arising from surface compressive residual stress, roughness, and grain distortion that can be induced by grit blasting, a set of rotating bend fatigue samples were coated without grit blasting. No coating delamination was observed while spraying onto the substrates or during fatigue testing, which confirmed adequate bonding. A set of specimens where the steel was grit blasted prior to coating deposition was also tested with the same coatings. The stress vs number of cycles to failure curve (S-N) for the annealed (A) steel, LT coated, and HT coated samples, with and without grit blasting prior to spraying, are shown in Figure 5-16. It is clear to see that there is a large difference between the coated samples' fatigue life depending on which coating is applied to the steel and if grit blasting was used.

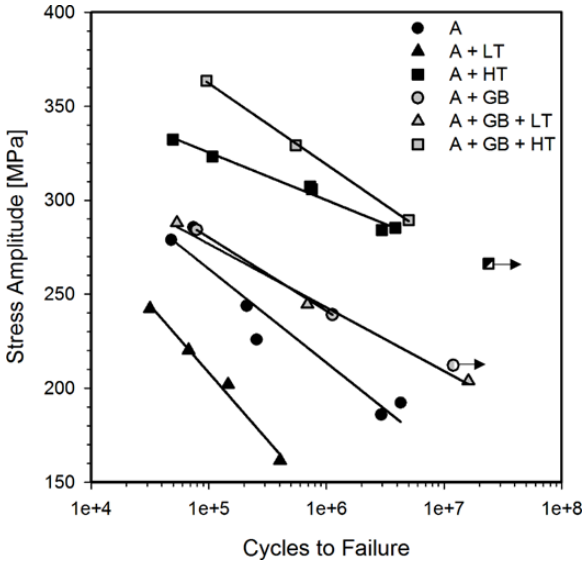

Figure 5-16 Stress amplitude vs. cycles to failure for Annealed 1018 steel (A) with Low and High Temperature WC-CoCr coated steel (A+LT and A+HT, respectively), specimens that were annealed and grit blasted (A + GB) with and without LT and HT coating deposition. Arrows indicate runout.

In the cases where the substrates were not grit blasted, the HT coated samples (A + HT) produced a large increase in fatigue life vs. the uncoated steel. The LT coated samples yielded a fatigue debit relative to the uncoated steel, indicating a high sensitivity of the coating application and surface deposition temperature on expected specimen fatigue life.

The set of samples that were grit blasted prior to coating deposition are also shown in Figure 5-16. From the Figure, it is evident that grit blasting slightly increased the fatigue life relative to the annealed steel samples, which can be attributed to the compressive stresses and grain distortion induced into the surface of the sample from the blasting process. The samples with the LT coating applied to grit blasted substrates did not show significant fatigue life difference from the grit blasted only samples. Although compared to the LT coated samples without grit blasting (A + LT), the difference between a fatigue debit or credit with LT coating deposition relative to

the annealed steel samples is shown to be dependent on grit blasting prior to coating application. The samples with grit blasting and the HT coating showed an increase in fatigue life relative to the grit blasted only specimens, with a slight increase in fatigue life when compared to HT coated samples that were not grit blasted.

Another set of samples were shot peened and tested with and without the application of the HT WC-CoCr coating and behaved very similar to the grit blasted substrates in the same scenarios and are not shown.

A typical fracture surface of the non-grit blasted and coated samples is shown in Figure 5-17(a), with the fatigue crack initiation and final fracture sites within the substrate indicated. Coating delamination was observed on many specimens adjacent to the final fracture site, though no adhesive coating failure was observed adjacent to fatigue crack initiation sites, confirming an adequate coating bond strength during fatigue testing, even without grit blasting. Figure 5-17(b) shows a more detailed image of the crack initiation site, where cohesive coating failure was frequently found in the adjacent area.

Fracture surfaces of the sample grit blasted prior to LT WC-CoCr coating deposition are shown in Figure 5-18(a). The coating shows a severe amount of in-plane cracks, as well as complete cohesive coating failure adjacent to the fatigue crack initiation site in the substrate. The fracture surface of the LT coating on a non-grit blasted substrate is shown in Figure 5-18(b), with an inset highlighting a crack that passed through the coating and substrate. Cohesive cracking within the coating is again visible, yet this instance shows a crack path passing through the substrate and into the coating.

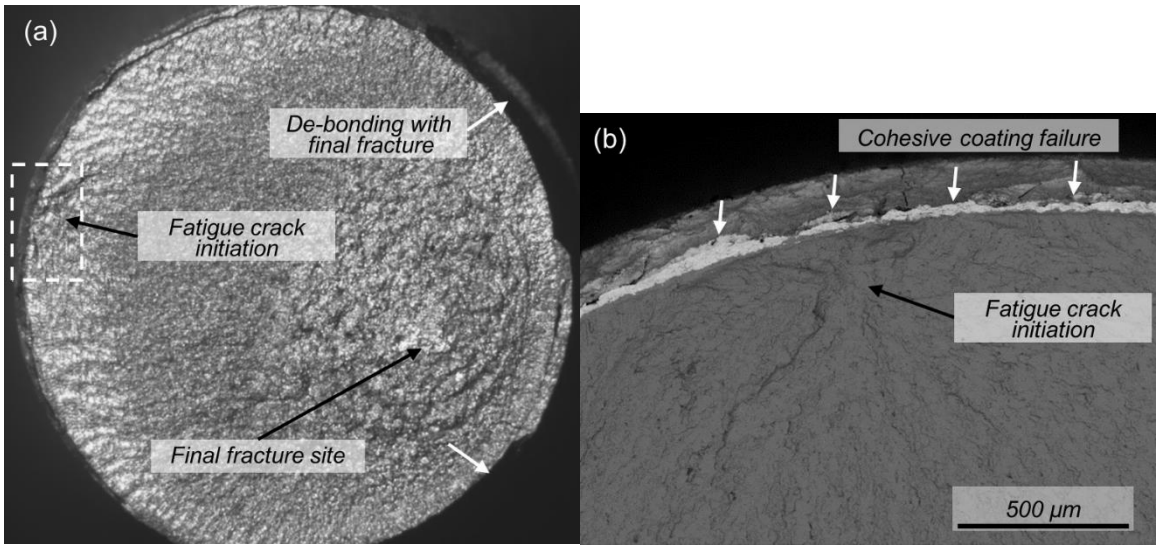

Figure 5-17 (a) Optical image of typical fatigue fracture surface with fatigue crack initiation, final fracture site, and coating de-bonding from final fracture indicate. SEM of the highlighted region of initiation site shown in (b) with cohesive coating failure and fatigue crack initiation site. Both images are of a single A + HT sample

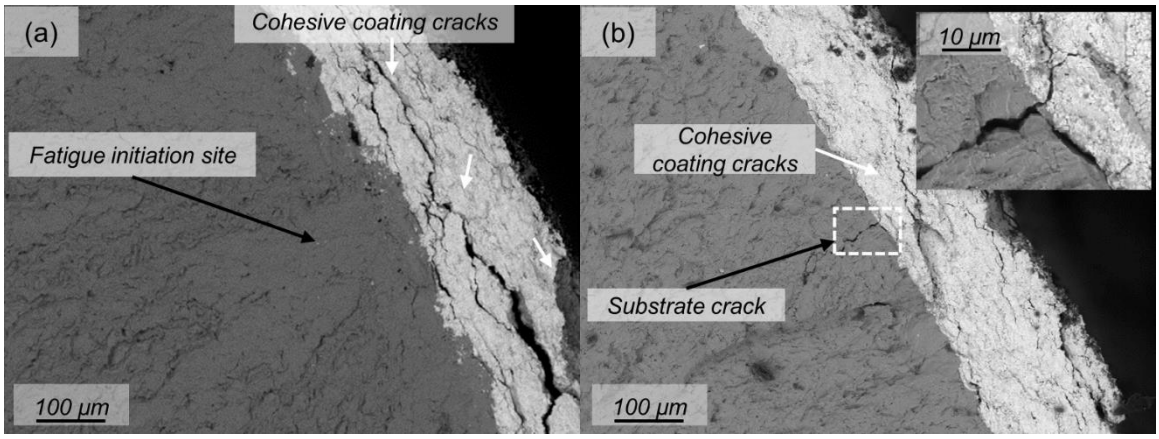

Figure 5-18 SEM images of fatigue fracture surface of LT coated samples (a) grit blasted prior to coating deposition, with fatigue crack initiation site and cohesive coating cracks indicated and (b) not grit blasted prior to coating deposition with similar cohesive

5.3.2.2 Coating Processing Effects

Grit blasted and non-grit blasted substrates that had both LT and HT coatings were chemically stripped and fatigue tested, as shown in Figure 5-19(a) for the LT coated and stripped samples and Figure 5-19(b) for the HT coated and stripped samples. It can be seen in the cases where the steel was not grit blasted prior to coating deposition that the S-N curve falls back in line with the annealed steel, indicating that the coating process did not induce a large change in the fatigue life of the steel in this case. The grit blasted specimens that were coated and stripped before fatigue testing also show a return to the S-N curve of the annealed and grit blasted specimens, though a slight drop in fatigue life is observed.

Fatigue testing of a stripped specimen that had been shot peened and coated showed no difference in fatigue life from that of only shot peened specimens.

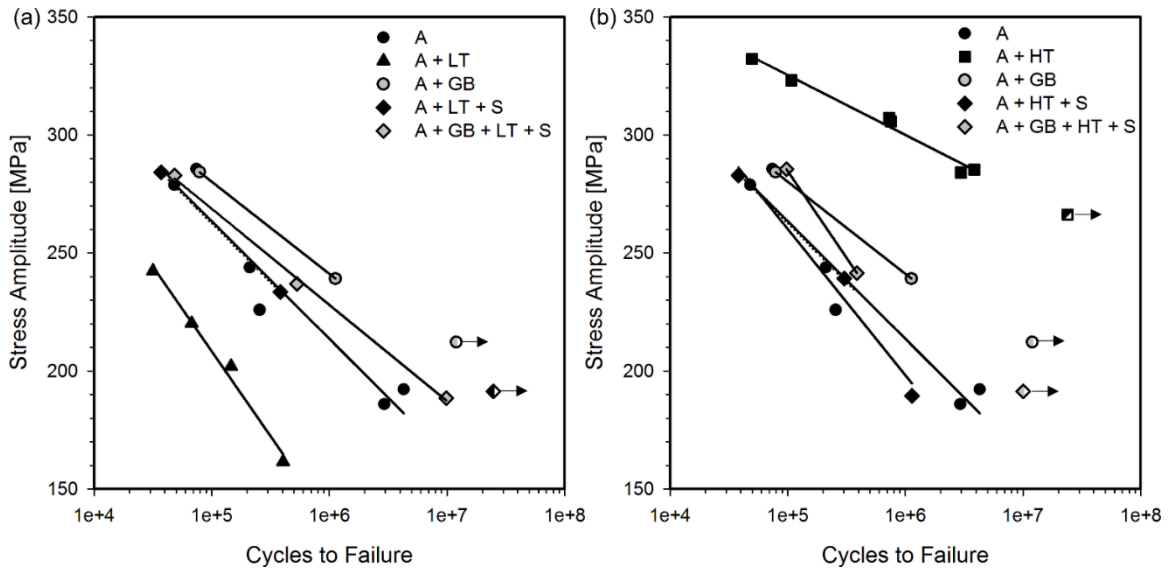

Figure 5-19 Stress amplitude vs. cycles to failure for specimens that were coated and stripped prior to fatigue testing, with and without grit blasting. LT and HT coated samples included for comparison in (a) and (b), respectively.

5.3.2.3 Partial Fatiguing

In order to assess how the coating and substrate deteriorate during fatigue testing, coated samples were fatigue tested for certain portions of the expected fatigue life and then halted from testing prior to fracture. The WC-CoCr coating was then removed by the stripping processes described in the experimental methods and resumed fatigue testing until failure as a bare substrate. No grit blasting of the substrates was done in this case. The results of this testing is shown in Figure 5-20(a) for a sample with the LT coating and Figure 5-20(b) for a sample with the HT coating, both with the relevant data from Figure 5-16 shown in grey. Sample a, with the LT WC-CoCr coating applied, was fatigued to approximately 50% of the expected linearly measured fatigue life at that stress, which correlates to 95% of its expected logarithmically measured fatigue life. After pausing fatigue testing and stripping the coating off, sample a' was fatigued at the same load until failure, falling short of the expected fatigue life for the uncoated steel samples, indicating significant damage to the substrate had occurred during prior fatigue testing as sample a. Sample b with the HT WC-CoCr coating applied was fatigue tested to the similar portion of expected fatigue life as sample a (50% linear, 95% logarithmic), though at a higher load and longer time due to the HT coated sample's prolonged life. After pausing and stripping the coating off, sample b' was fatigue tested to failure, reaching a life equivalent to that of the baseline annealed 1018 steel material, suggesting that no significant damage accumulated within the substrate during the prior fatigue testing as sample b

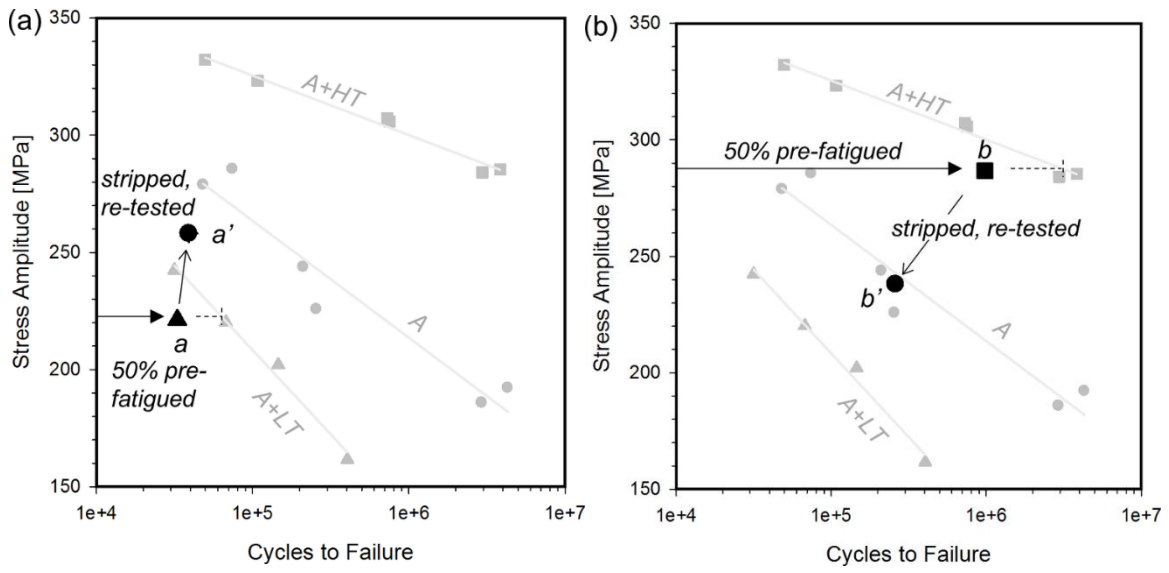

Figure 5-20 Stress amplitude vs. cycles to failure for coated samples that were partially fatigue tested, stripped, and tested as uncoated until failure for a sample with (a) LT coating and (b) HT coating. Related samples from Figure 3are included in grey as reference

5.3.3 Role of Substrate

Though a large amount of structural components that require damage tolerant coatings are steel based, the composition and metallurgical condition of the steel (grain size, % work hardening) will have a large influence on the fatigue life of a steel specimen undergoing cyclic stress. In the presented cases thus far, the 1018 steel RBF and uniaxial fatigue specimens have been in either in the as-received (cold drawn) state or annealed. In order to characterize the grain structure of the two steels, longitudinal and radial cross sections were mounted, polished and etched with 2% Nital solution. The optical images highlighting the differences in grain structure for the two samples is shown in Figure 5-21

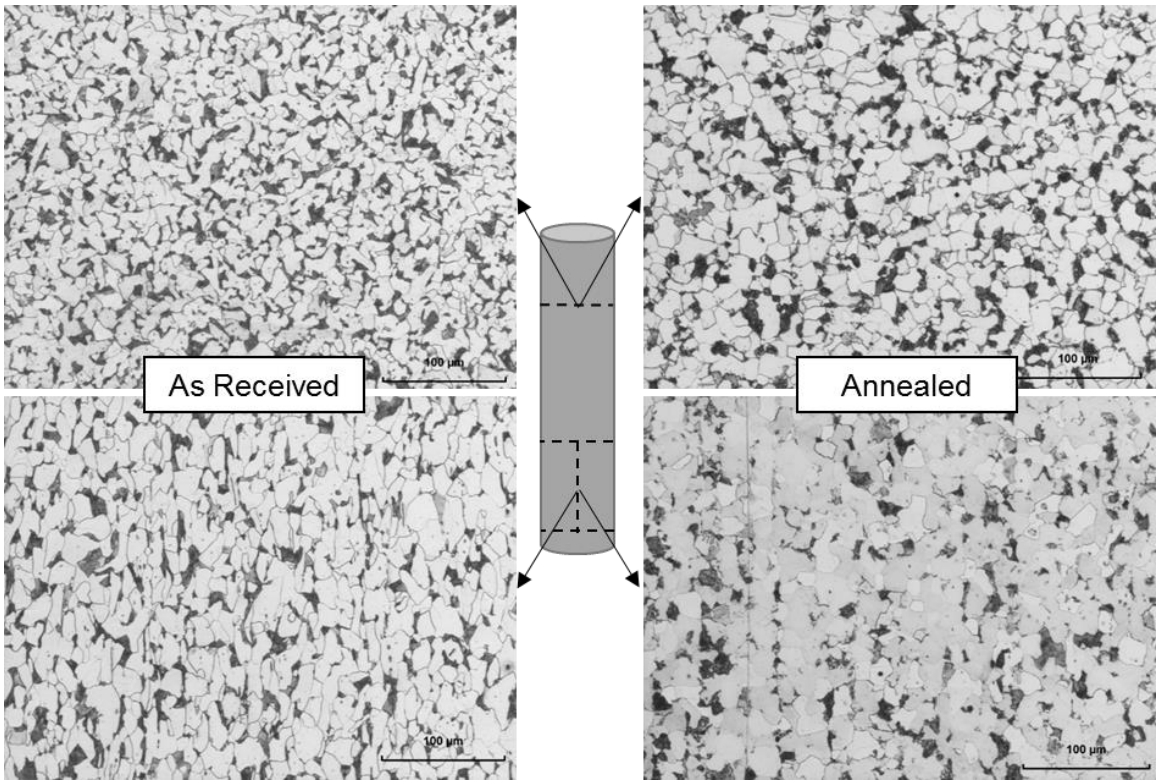

Figure 5-21 Etched cross section of the as received and fully annealed 1018 steel used for RBF testing

Here it is seen that the as-received steel contains longitudinal oriented grains, resulting from its cold drawing production, thus producing an anisotropic microstructure. With annealing, it can be seen that some change in grain size and direction is produced, though an anisotropic grain microstructure still resides in the annealed specimens.

A WC-CoCr coating was deposited with the same torch and deposition conditions (condition 8 in Table 5-1) onto both the as-received and annealed RBF samples and fatigue tested until failure. These results are shown in Figure 5-22. Both substrates were grit blasted prior to coating application

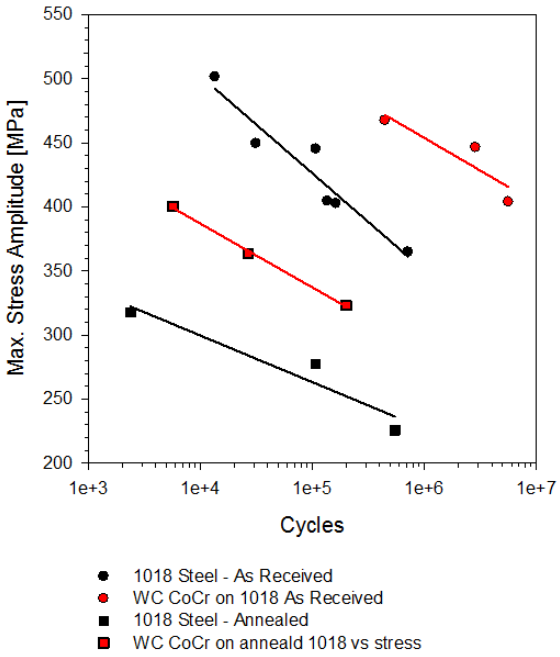

Figure 5-22 Stress amplitude vs. cycles to failure for the same WC-CoCr sprayed onto as received and fully annealed 1018 RBF steel specimens, with both uncoated substrate included for comparison

It can be seen that the annealing of the 1018 steel reduces the fatigue life relative to the as-received state considerably. Fatigue of steel materials have shown that grain orientation can both increase or decrease the rate of damage propagation, depending on the loading direction [79]. In the case of the longitudinal grain orientation being in-line with the applied stress and normal to the preferred direction of fatigue crack growth, the higher fatigue life of the as-received steel can be explained. Annealing of the steel may also soften the material, lowering the yield strength of the steel and therefore the threshold for fatigue damage to initiate.

When an identical WC-CoCr coating is put onto both the as-received and annealed RBF specimens, the resulting S-N curve shows that both coatings offer fatigue benefit to the samples, yet the initial fatigue life debit incurred through annealing is not fully recovered by coating

application. With the same processing parameters and expected thermal stresses, no residual stress differences in the coating or substrate is to be expected. The two steel states would also have the same elastic modulus, thus not altering the load sharing or stress profile within the coated specimen, leaving the dominating fatigue of the specimen's fatigue life the state of the steel prior to coating application in this case.

In the pursuit of lighter base materials, a designer may choose a material such as titanium or aluminum based alloys for the substrate material. In such a case, not only is the fatigue behavior of the base material subject to be different than that of the steel conditions shown here, but several differences in coating-substrate interactions will arise in coating deposition and specimen loading. The difference in thermal expansion between the coating and substrate will produce considerably different thermal stresses, and thus residual stresses, with the same torch operating parameter. Figure 5-23(a) shows the calculated residual stresses from beam curvature measurements of the same torch operating parameter as used for the steel RBF specimens (condition 8 in Table 5-1) sprayed onto low carbon steel and Ti64. Two different deposition patterns (Figure 5-2) for each resulting in two different substrate temperatures, shown in Figure 5-23(b).

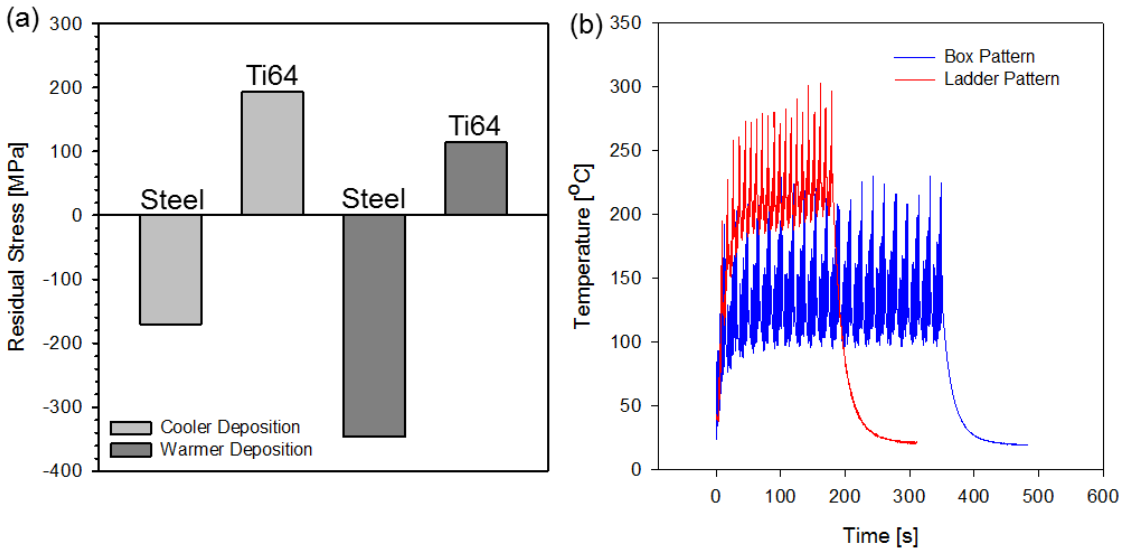

Figure 5-23 (a) Calculated residual stress of the same WC-CoCr coating sprayed onto steel and Ti64 substrates using different deposition patterns on an in-situ beam curvature measurement device. (b) Substrate backside temperatures measured for the spraying of samples in (a) with different deposition patterns.

The same torch parameter (and thus particle state) result in largely different residual coating stresses, with coating applied on the steel substrate in compression and the same coating on Ti64 resulting in a tensile residual stress. As discussed in Section 5.3.2, the thermal stress can contribute significantly to the coating residual stress. In the case of steel (CTE ~ 12µm/m °C) and WC-CoCr (CTE ~ 6µm/m °C), a significant thermal mismatch strain is expected, adding compressive residual stress upon cooling, whereas the CTE of Ti64 (~9µm/m °C), the expected thermal stress is roughly halved. Deposition stresses may be different between the substrate, and subsequently, factors such as bond strength due to interfacial forces and wetting may be altered.

When the same coating condition as the as-received and annealed steel specimens above are sprayed onto Ti64 RBF samples (Condition 8 in Table 5-1), it can be assumed that the expected residual stress state will be largely different and possibly in the opposite stress state.

The coated Ti64 samples were fatigue tested in the same manner, with the SN results shown in Figure 5-24. All samples were grit blasted prior to coating application

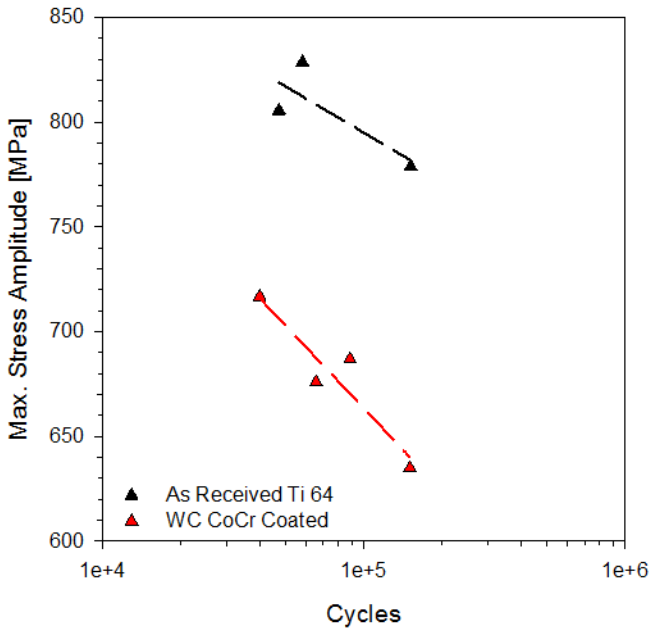

Figure 5-24 Stress amplitude vs. cycles to failure for the same WC-CoCr coating condition in Figure 5-22 sprayed onto Ti64 substrates. Uncoated Ti64 shown for comparison

The fatigue life of the as-received Ti64 is much higher than that of either steel, though when the WC-CoCr coating is applied, there is a decrease in the relative fatigue life as compared to un-grit blasted and uncoated samples. Assuming a largely different residual stress state is present in the coating, with nominally the same properties as the coating sprayed onto the steel samples, a change in the fatigue life could be expected as seen in the case of thermal stress manipulation in 5.3.2. As an additional difference from steel RBF specimens, the lower modulus of Ti64 would place a larger portion of the load carrying onto the coating during fatigue testing.

This would raise the stress experienced by the coating in addition to the likely tensile residual stress

Other factors may include any detrimental thermal sensitivity of the Ti64 alloy to the coating process or the roughening from the grit blasting process having accounting for fatigue life reduction through the severe notching sensitivity in titanium alloys. These aspects were not investigated.

5.4 Discussion

In the TS coated specimen fatigue work presented, it has been demonstrated that many factors influence the fatigue life of a TS coated component, such as the initial substrate fatigue behavior, torch operating parameters, and deposition conditions. The substrate also provides a benchmark of which to compare these coating processing influences, allowing for dissection of these fatigue results. TS coatings are inherently defect-containing structures with pores, cracks, and inter-splat boundaries. Whereas fatigue of bulk materials depends upon dislocation pile-up to provide roughness and necessary stress intensification for fatigue crack initiation, the presence of defects in TS coatings provide stress intensification points within the coating prior to any mechanical loading. This inherently changes the fatigue nature of TS coatings, where stresses and defects within the coating play the larger role in determining fatigue life of a coated specimen.

As any material is loaded either uni-axially or in a bending moment, an applied stress profile exists within the material, which is uniform in the uni-axial case but variable in bending. When stressed and un-stressed below the yield point repeatedly, the material is prone to failure

by fatigue and the expected fatigue life of the material is related to the amplitude of peak stresses experienced within the applied stress material. If a material is coated, it becomes a bi-material, as in the case of the TS coated specimens. The resulting stress profile within the substrate and coating upon application of a bending moment or uniaxial load to the RBF sample is altered, due to the presence of the TS coating. The magnitude of the applied stress throughout the specimen will depend on the coating's thickness and modulus, altering the stresses experienced within the substrate and coating as compared with an uncoated sample. Specimen curvature calculated using statics equations of pure bending of a coated cylinder (an assumption for the thinnest diameter of the RBF specimen) take into account the moduli difference and dimensions of the coating and substrate as such.

$$K = \frac{64\ M}{E_s \pi D_s^4 + E_c \pi (D_{s+c}^4 - D_s^4)} \qquad \text{Equation 1}$$

Where K is the curvature of the specimen, M is the applied moment, E is the modulus of the coating or substrate, and D is the diameter of the substrate or substrate with coating. Knowing the curvature of the specimen allows for calculation of the local stresses throughout the specimen.

$$\sigma_s = E_s K R \qquad \text{Equation 2}$$

$$\sigma_c = E_c K R \qquad \text{Equation 3}$$

Where R is the radius throughout the specimen. Figure 5-25 shows the calculated longitudinal stress profile under a single moment using these equations for different coating moduli, using coating and substrate dimensions from those in Section 5.3.2. It is clear to see that coating addition lowers the local stress amplitude within the substrate by the coating accommodating a portion of the load, depending on the modulus of the coating.

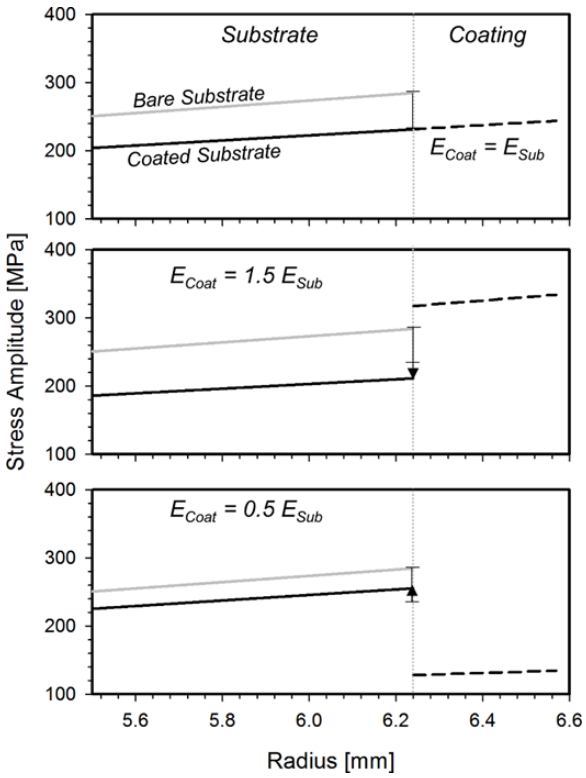

Figure 5-25 Calculated applied longitudinal stress profile from pure bending moment (6.78 Nm, 60 in-lb,) of a cylinder with coating modulus at 0.5, 1.0, and 1.5 times that of the steel substrate. Dimensions and values used
Substrate: E = 205 GPa, ν = 0.29, Radius =3.12 mm, Coating: ν = 0.23, Thickness = 0.165 mm

The dimensions of the substrate and coating are simple variables that will depend on a case by case basis, as well as the elastic modulus of the substrate material. The coating modulus will be limited by the intrinsic modulus of the material chosen for coating application and will also vary largely upon processing. With phase change considerations aside, the apparent modulus of the coating will be determined by such factors as splat-to-splat bonding, where any coating porosity or weak inter-lamellar bonds will reduce the stiffness of the coating. Particle state has been shown to have a large influence on the formation of the coating on a splat bonding basis (Figure 5-6, Figure 5-9, Figure 5-11), with secondary effects of deposition surface temperature shown in Figure 5-15(a) having the ability to influence the indentation modulus of the coating as

well. Once these deposition factors are coalesced into a coating with particular mechanical properties, the stress profile across any specimen geometry can be predicted (assuming perfect mechanical bonding).

In addition to the applied stress profile of a TS coated specimen upon loading, there is also the superposition of the residual stress within the coating-substrate profile that must be considered for accurate description of locally experienced stresses within the materials. As it has been repeatedly shown throughout this work, residual stresses inherently arise from TS coating processing in the forms of quenching and peening deposition stresses and thermal mismatch stresses. Since stress intensification is considered a large condition in determining fatigue crack growth rate and local stresses within a specimen lead to the likelihood of fatigue crack initiation, it is critical to understand the super-position of both the applied stresses and residual stresses within a TS coated component. The manipulation of residual stresses in TS coatings through torch selection, operating parameters and deposition conditions, described in Chapter 3, offers a coating designer considerable freedom in targeting desired coating stresses not only for surface functionality, but also for fatigue considerations. As Figure 5-8 and Figure 5-10 show, cermet coatings with expected higher compressive stresses performed better than those materials with a less compressive or more neutral expected residual stress. The same behavior is seen in the case of the uniaxial fatigue specimens in Figure 5-12, where the coating with the highest expected compressive residual stress is the only set of samples that offer a fatigue life benefit as an integrated structure. Note that the residual stresses measured by beam curvature methods, i.e., planar samples cannot be assumed to be exactly the same as in the cylindrical substrate due to differences in relative surface speed, expected angular particle impact, and different substrate

surface temperatures. However, the qualitative residual stress differences can be expected to be the same between coating conditions.

It is important to consider that the differences in residual stresses in the examples described in Section 3 which were achieved through particle state manipulation also changed the coating properties in-tandem. In order to manipulate the coating residual stress with the same torch operating parameters and with as little alterations of the coating properties as possible, the study in Section 5.3.2 was carried out where manipulation of the thermal stress component was achieved through deposition stroke timing. With curvature based stressed measurements, it is clear to see that a higher surface temperature during coating deposition primarily results in large differences in thermal stress, and ultimately the coating's residual stress, as shown in Figure 5-14(a). It has been documented how the local deposition temperature of an impacting splat can affect its quenching behavior, particularly bonding strength [47, 48]. With both deposition conditions for the HT and LT coatings in Figure 5-14(a), which have the same surface speed, feed rates, and cooling, the different surface temperatures experienced during deposition explain the differences of the measured coating hardness and modulus for the planar samples as seen in Figure 5-15(a). In the case of these coatings being sprayed on cylindrical samples, the higher thermal expansion mismatch between aluminum (~24 µm/m °C) and HVOF sprayed WC-CoCr (~6 µm/m °C) versus low carbon steel (~12 µm/m °C) would nearly double the expected thermal stress, yet it is primarily the surface deposition temperature influencing coating hardness in Figure 5-15(b). Therefore, it can be inferred that the impact of thermal stress alone on the coating hardness is negligible in this case and it is instead the quenching and bonding behavior of individual splats that are affected. Thus, it can be stated that the slight differences in coating hardness and large differences in thermal stress occur in tandem as a result of the deposition

parameters (stroke pause timing) and subsequent surface temperature, yet do not directly influence each other.

Such differences can be expected in the case of the LT and HT coatings sprayed onto the RBF specimens, where a slightly stiffer HT coating would offer a larger contribution to the load sharing of the sample's bending moment than the LT coating. More importantly, the expected differences in coating residual stress due to thermal stress would impart the HT with a greater magnitude of compressive residual stress. Figure 5-26 shows the magnitudes of expected longitudinal thermal stress for the two coatings, calculated using the model described by Tsui and Clyne [80] and a deposition temperature of 50°C and 150°C for the LT and HT coatings, respectively. Depending on the modulus of the coating after deposition, the magnitude of the stress imposed in both the coating and substrate can vary, with a stiffer coating producing higher stresses. This demonstrates the high sensitivity of the coating's stress state on the thermal stress, with a significantly lower stress induced in the substrate for this scenario. Calculation of an expected deposition stress contribution using the Tsui and Clyne model for the RBF specimens cannot be assumed to be the same as the planar specimens due to differences in relative surface speed, expected angular particle impact, and different substrate surface temperatures. However, calculations indicate approximately a 10 to 1 ratio for the magnitude of deposition stresses experienced by the coating and substrate, respectively, within these expected dimensions. This again underlines the critical importance of processing on coating residual stress.

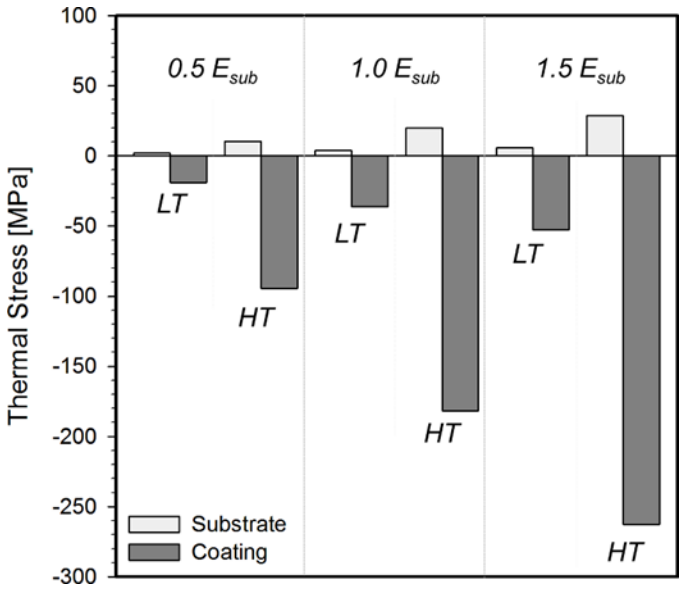

Figure 5-26 Calculated longitudinal thermal stresses of a cylinder using the Tsui and Clyne model for the Low Temperature (LT) and High Temperature (HT) coatings with coating modulus at 0.5, 1.0, and 1.5 times that of the steel substrate. Deposition temperatures of 50°C and 150°C were used for the LT and HT coatings, respectively, and ambient temperature of 25°C

Substrate: E = 205 GPa, ν = 0.29, Radius =3.12 mm, α = 12 μm/m °C
Coating: ν = 0.23, Thickness = 0.165 mm, α = 6 μm/m °C

Similarly, additional residual stresses due to grit blasting or shot peening would also superimpose on the stress profile, offering a benefit to the substrate and thus to the coated specimen's fatigue life, as seen in Figure 5-16. These stresses produced via grit blasting or shot peening are largely left unaltered by the coating process heat, which is evident by the samples that were coated and stripped prior to fatigue testing (Figure 5-19). In the case of the annealed steel sample in Figure 5-16, grit blasting adds a noticeable credit to fatigue life of the steel, whereas in cases on non-annealed steel, such Figure 5-8, the grit blasting does little to affect the fatigue life of the steel. Perhaps the compressive stresses induced were lower owing to differences in the strength of the material or that the roughness increase largely counteracted whatever gain was achieved through the blasting. In the case of Ti64, the high notch sensitivity of the alloy reduces

the fatigue resistance of the material with grit blasting, which may account for the drop in fatigue life observed in Figure 5-24. It is also suggested from the stripped coating samples without any grit blasting that the high kinetic energy particles that initially impact the substrate surface do not impart a fatigue life benefit such as grit blasting or shot peening does. Thus, it can be said that the state of the substrate is largely left unaltered by the coating processes in this scenario. This may not be the case for more thermally sensitive or softer substrates, such as tempered aluminum alloys or copper, for example.

The expected residual and applied stress profiles can now be utilized to explain fatigue performance. As evident for samples b' in Figure 5-20, testing a significant portion of the expected HT coated sample's fatigue life did not accumulate significant damage within the substrate, indicating that the stiffness of the coating adequately reduced the stress amplitude experienced by the substrate, delaying damage accumulation. The higher hardness and more compressive residual stress in the coating contributes to the integrity of the coating being maintained for a longer period of fatigue testing. The opposite case was observed with the LT coating in samples a and a', with the higher amount of coating tensile stress and lower hardness not being able to maintain the coating integrity during fatigue testing. It is possible that a lower coating stiffness in the LT coating did not adequately alleviate the stress experienced by the substrate as well. Thus, the substrate began to accumulate fatigue damage much earlier in the same portion of expected fatigue life

In the case where both coating stresses and properties were largely different, such as the CrC-NiCr coated fatigue specimens in Figure 5-8, both residual stresses and the coating properties play a role in the fatigue life. The compressive coating is expected to have a higher modulus than the neutral coating, as the planar samples did (Figure 5-7). This would reduce the stress intensity experienced by the substrate during fatigue testing. The compressive stress within the coating,

along with the higher hardness, allows the coating to withstand cyclic loading for a longer period of time before accumulating damage, where the load carrying ability of the coating would be reduced.

Experimental studies, as well as modelling [81],have reported on the behavior of crack advancement through two well bonded materials of the same modulus. Crack advancement occurs in the softer material when the crack is initiated in the harder material, and crack blunting occurs when an initiated crack within the softer material approaches the interface of a harder material. In the case of a WC-CoCr coating perfectly bonded to a 1018 steel substrate, it is possible that crack advancement from the coating into the substrate can occur. However, the weaker coating-substrate interface and the anisotropic nature of thermal spray coatings inherent in their deposition method [37] offer different crack pathways than the through-thickness direction, producing the in-plane and interfacial branching directions the coating crack takes in Figure 5-18(b). The large amount of in-plane (cohesive) coating cracks observed on the fracture surfaces of the majority of the RBF samples agree with this preferred crack pathway, with primary fatigue crack initiation occurring in the substrate. It can be hypothesized that the coating can act to delay fatigue damage initiation and propagation within the substrate if adequate stress reduction is supplied to the substrate. The hardness and the residual stress of the coating determines its ability to resist damage due to cyclic loading, yet does not increase the likely-hood for premature deleterious coating-to-substrate crack advancement in these scenarios and is instead driven by substrate fatigue crack initiation and growth

5.5 Conclusion

The fatigue life of TS coated components was explored through several studies that included variations in coating materials, spray torch parameters, deposition conditions, and

substrate materials on both uniaxial and rotating bend fatigue specimens. It was shown that both increases and decreases to the fatigue life of coated parts are possible with the above process changes.

One of the key factors in determining the fatigue life of TS coated components is the compressive residual stress within the coating. Better coating properties for damage tolerance (e.g., hardness, modulus) can be expected from more compressive residual stress coatings, as discussed in Chapter 3. Both specimen heating by the torch and stripping of the coating prior to fatigue testing indicated that little change occurred to the substrate's fatigue life due to the TS process. Stripping of the coating after partial specimen fatigue testing revealed no change in the fatigue life of the substrates for those coatings with higher compressive residual stress. This was not the case in samples with less compressive residual stress in the coating, where fatigue life of the substrate was shortened. Substrate choice and condition with the same coating was shown to different fatigue life changes, with a benefit to steel and a detriment to titanium-based substrates.

The mechanism of how TS coatings modifies fatigue life of components was discussed. Coating addition reduces the stress upon the substrate material, depending on the properties and dimensions of the coating. The residual stress profile from the TS process is superimposed on the coating-substrate system, further changing the local stress experienced. It was then shown that as the coating deteriorates from cyclic loading, more load gets transferred to the substrate, thus increasing the stress levels experienced in the substrate. The initial condition of the substrate, as well as sensitivities to grit blasting and the coating process then determines the remaining fatigue life.

6 Synthesis of work

The body of this work has presented several aspects of the processing-properties-performance relationships for TS coatings produced by high velocity deposition, with the aim to develop the necessary criteria for the coating to meet the multi-functional requirements of wear and corrosion protection, while simultaneously offering synergistic benefit to the structural performance of the entire coated component. With these processing considerations, a schematic pathway for understanding the mechanical behavior of structurally integrated TS coatings is shown in Figure 6-1, with several of the topics addressed in this work.

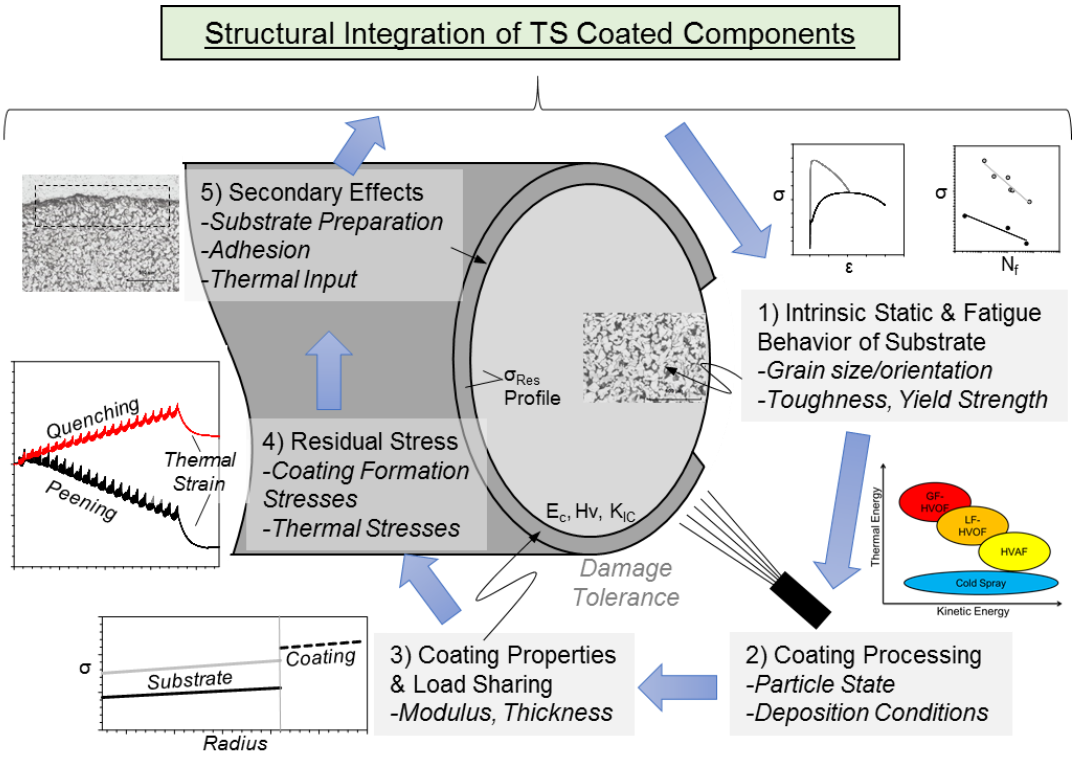

Figure 6-1 Schematic pathway for the factors determining the effects of structurally integrated TS coatings

The first box in Figure 6-1 accounts for the intrinsic static and fatigue strength of a substrate that is to be coated by TS. The composition and metallurgical state of the substrate to be sprayed on will vary depending on the particular application, thus having different properties. Some of these substrate properties will be interact with the coating's properties, such as thermal expansion mismatch (Section 5.3.3), whereas other properties will be independent until considered in mechanical testing. The benchmark comparison of the mechanical performance of the uncoated substrate vs. coated substrate will also give an indication if the coating application gives a synergistic benefit, enhancing the component's performance and enabling the consideration of prime reliance.

The second box, coating processing, is where all the factors of feedstock composition, torch selection, torch parameter, and deposition conditions are explored and the coating surface functionality is decided. The processing and properties of these coatings will determine functional performance, such as corrosion protection and/or wear resistance, though these same properties will have a role in the structural integrated performance of these coatings. Section 3 explored several of these materials and processing parameters and their influence on coating properties.

The third box indicates how load sharing in the coating-substrate system is now altered through addition of a TS coating. Coating and substrate elastic mechanical properties and the load or moment applied to a coated component will determine the local stress experienced throughout the coated body. Manipulation of processing parameters, coating thickness, and specimen geometry will all play a role in determining what stresses are to be expected. Similar to any structural material design, management of these applied stresses will aid to ensure mechanical failure does not occur in service.

However, as the fourth box indicates, the nature of TS processing results in considerable residual stresses present within the coating and substrate. These residual stresses would then be superimposed onto the applied stresses experienced in a coated component, thus altering the experienced stress within a loaded coating-substrate system. Manipulation of these stresses through processing was demonstrated throughout this work, showing how feedstock materials, torch selection and operating parameter, deposition conditions, and coefficient of thermal expansion differences can all play a role in determining coating stress.

Finally, the fifth box brings consideration of secondary effects to the coating-substrate mechanical performance from the pre-processing or coating processing itself. Such effects

include how the substrate is prepared prior to grit blasting (e.g., shot peening, grit blasting) where changes in surface roughness and addition of compressive residual stress have shown differences in mechanical behavior (Figure 4-18Figure 5-19Figure 4-18 Stress strain behavior of grit blasted copper substrate that was exposed to torch heat only (no powder), with little difference from only grit blasted substrate). Proper coating adhesion must also be ensured by surface preparation, where a lower adhesion will reduce the coating's load carrying contribution to the specimen (Figure 4-10), thus lacking structural integration. Heat input to the substrate during coating application also has the potential for changing mechanical performance through such mechanisms as stress relief (Figure 4-6).

When all these considerations are taken into account, the ability to predict the fatigue life or static strength of a TS coated component is elucidated. The residual stresses and defect containing microstructures of TS coatings considerably vary the mechanical behavior when compared to bulk materials, requiring in depth study of the processing-property relations of the spray process. With these necessary relationships are identified, the optimization of a structurally integrated TS coating can be used in the design of a load bearing component to enhance not only surface functionality, but synergistic mechanical benefit as well.

7 Conclusion

Several aspects of the processing influence on coating properties and performance for wear and corrosion protection were outlined in Chapter 3, including the variables of spray material and process selection. Each spray material and torch selection then has further variables of feedstock material morphology and torch operating conditions, producing variations in particle state from the transfer of thermal and kinetic energy from the plume to the particles. Further particle-plume interactions were documented pertaining to the phase changes and decomposition experienced by the particles during flight. The state of the in-flight particles, coupled with deposition conditions, was found to have significant influence on one of the most critical aspects of TS coatings; formation and residual stresses. The magnitude of formation and residual stresses were assessed via in-situ beam curvature measurements, offering key insights into the evolving stress based on kinetic energy and deposition rate. Properties such as modulus and hardness give indicators of the coating density and integrity of splat- bonding, with the densification and compressive stresses from high particle kinetic energy compacting the coating for beneficial wear and corrosion performance.

With the ability to produce dense and strong coatings through high velocity TS processes and judicious parameter selection, the load bearing capability of these coatings were assessed in the form of tensile testing in Chapter 4. The coating processing benefits of high velocity TS was shown to have synergistic benefits in composite strengthening in select cases, such as HVOF

nickel deposited onto steel. Though TS coatings are generally more brittle than the bulk materials they are comprised of, the load sharing between strong coatings and their substrates displayed synergistic benefits of strengthening of the bi-materials, as well as graceful failure when the coating takes on damage. The effect of coating application on the stress-strain behavior of the substrate was also shown to be minimal in the case of ferrous substrates, with some stress relief occurring in substrates that have residual stresses from previous processing. With substrate that are more sensitive to work hardening and thermal effects, such as copper, the coating processing effects on the substrate are more severe, where grit blasting and heat from deposited particles are able to change the stress-strain behavior of the substrate. The additive manufacturing of aluminum by contrasting processes of wire arc and cold spray again demonstrated that not all TS coatings are able to offer the same synergistic strengthening, even as the load bearing of the composite increases with added thickness. The stress-strain behavior of damage tolerant coated steel, such as WC-CoCr and alumina, demonstrated different load carrying abilities with purely ceramic coatings yet suffered from higher degrees of brittle-ness and not adequately strengthening the tensile specimen. WC-CoCr, a Cermet material, was able to synergistically strengthen the tensile specimen without brittle coating failure, aided by the addition of ductile binder material (CoCr).

Engineering components are generally not designed for operation near expected failure stresses, therefore the predominant mechanical failure mechanism of concern that can occur in coated components comes from changes in expected fatigue life from the substrate. Thus, the alterations to the fatigue life of a component that has been TS coated were the focus of Chapter 5, where the influence of coating processing on fatigue life was investigated. The role of the residual stresses within the TS coating were clearly shown to have an influence on the relative

fatigue life. Manipulation of these residual stresses were achieved both by varying particle state and by controlling deposition conditions. Variation of the particle state through torch operating conditions also had large influences on the coatings' mechanical properties, such as indentation modulus and hardness. Stress manipulation through the deposition conditions explored had minimal effects on these coating properties. The damage progression of a coated component was demonstrated, where stripping of a coating part way through fatigue testing revealed whether or not fatigue damage had accrued within the substrate up until that point. It was demonstrated that in the case of a poor coating, damage occurred within the substrate when tested to a percentage of the expected fatigue life. However, in the case of fatigue enhancing coating added to the substrate (i.e., a coating condition that extended overall fatigue life), no damage had accrued within the substrate at the same percentage of expected fatigue life. It was also demonstrated that the same coating may not be ideal for different substrate scenarios, where a single coating condition on a titanium and steel substrate offered a fatigue debit and credit, respectively. Differences in expected residual stress (through thermal stress differences), substrate sensitivity to pre-processing (i.e., grit blasting), and substrate modulus differences could account for these differences. Thus, consideration of both the substrate and coating (both processing and presence) are paramount in prediction of fatigue life.

Once considered only for surface functionality or for low performance demanding repair (restored dimensions, cosmetic), TS coatings can now have significant ramifications on the mechanical performance of a coated components either in static tensile or cyclic fatigue scenarios. The pathway to processing a coating that adds both surface functionality and maintaining or enhancing mechanical performance of the entire component is the key to providing multi-functionality of TS coatings. The tensile and fatigue behavior discussed in

Chapter 4 and 5, respectively, describe testing methodologies for mechanical assessment of coating application. Coating properties, and most importantly residual stress, are critical for how load will be distributed throughout the component and the locally experienced stresses. The synthesis and control of such properties were thoroughly demonstrated in Chapter 3, where feedstock material, processing control, and deposition will determine coating residual stresses and properties. Additionally, the surface performance of these coatings (wear and/or corrosion) are also dependent upon these very same processing conditions. The difference between treating TS coating as a surface enhancement vs. a structurally integrated layer addition is the consideration of the coating and substrate as a system within TS processing. Whereas surface characteristics such as wear resistance generally do not depend on the underlying substrate, structural performance of a coated component is highly dependent on the substrates behavior, with a coating having the ability to significantly alter component mechanical behavior and life.

8 Future Work

8.1 Process-Property Relationships

Feedstock Morphology/Chemistry and Evolving Stress

In Section 3.3.2.3, it was discussed how the different morphologies of WC CoCr had drastically different evolving stresses based on the same torch operating conditions. The mechanism behind this observed effect is not entirely clear, but points to the powder size and carbide grain size having an effect in this case. Other factors may include morphological density, which may change the melting state achieved in-flight and the particle impact and bonding behavior. The implications of a different evolving stress, and thus residual stress state within a coating, have been shown on such performance aspects as wear, corrosion, and fatigue. Thus, the ability to understand the mechanism that powder morphology can have on tailoring coating stresses opens new opportunities to reliably and robustly produce coatings with desired residual stresses.

In conjunction with feedstock morphology, the chemistry of the feedstock powder will have a large influence on the evolving stress in high velocity TS deposition. Every coating material has a degree of workability for compressive stresses to be generated during deposition, such as soft metals like copper, whereas harder materials will be unlikely or impossible to achieve peening dominant evolving stress, such as high volumetric carbide Cermets or pure ceramics. As it was discussed in section 3.3.3.2, the tendency for inflight particle oxidation for

susceptible metals can drastically change the evolving stresses of such species. The primary mechanisms suspected for this would be the subtraction of quenching stresses from inhibited splat bonding, allowing peening to be the dominant stress mechanism for more oxidized particles. The effect on particular coating properties and performance from this effect would be particularly interesting, to see if a benefit from compressive stresses arising particle oxidation could be optimized for a greater performance than un-oxidized and coatings in tension.

One example of both powder chemistry and morphology is shown in Figure 8-1, where alternatives for a powder feedstock material reveal differences in evolving stress for the same torch operating parameter.

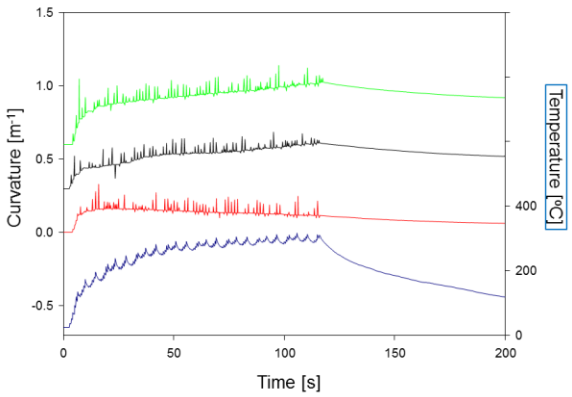

Figure 8-1 Curvature evolution of three Cermet feedstocks of various morphology and chemistry sprayed with the same DJ torch parameters

Here it can be seen that the denser morphology powder (red) has a net peening evolving stress, whereas the less dense particles (green and black) have a quenching evolving stress. Based on performance requirements, the benefits or detriments of such feedstock differences would be worthwhile to explore as cheaper coating feedstock alternatives could exist that would enable greater cost benefit or lower the entry costs for particular coating applications. Such

process mapping and mechanistic study of the effects listed in Section 3 would be necessary for such a study

8.2 Static Tensile Testing

Incorporation of Digital Image Correlation

The use of digital image correlation (DIC) for the mapping of 2D strain within tensile specimens have gained significant popularity in recent years, especially in cases of additive manufacturing [82]. The ability to globally assess two dimensional strain offers considerable benefit over strain gauges or extensometer measurements. TS coatings are a prime candidate to benefit from DIC measurements, where the surface behavior such as cracking and delamination can be more easily quantified and correlated to coating properties such as toughness and residual stress. Extrinsic factors on coating tensile performance, such as coating thickness or finishing, may also be explored using digital image correlation. An example of WC CoCr sprayed to different thicknesses is shown in Figure 8-2, where the delamination behavior is considerably different. The use of DIC could enhance the understanding of coating failure under loading and be used to optimize coating properties and thicknesses.

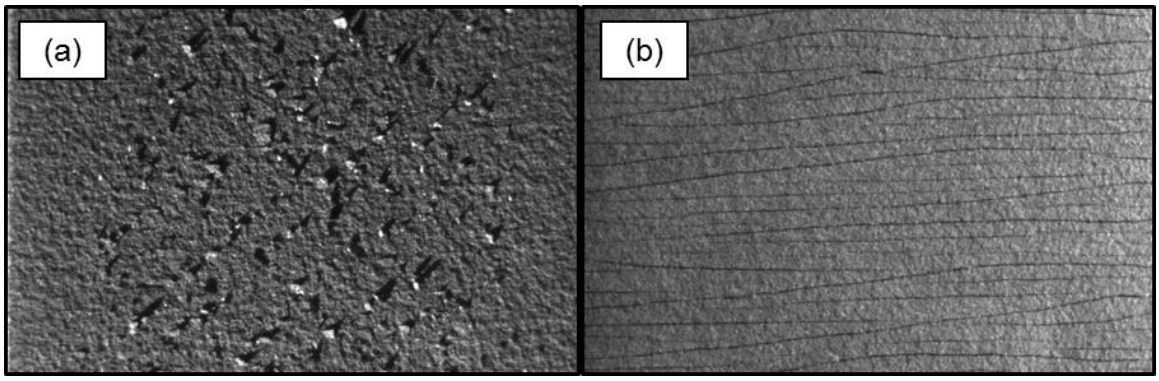

Figure 8-2 Cracking and delamination of WC-CoCr coatings on steel tensile specimens at different coating thickness (a) 65µm and (b) 200 µm

Preliminary work has also shown significant differences in the fracturing and delamination of coated specimens under static tensile load. One such example shown in Figure 8-3, shows how the fracturing behavior of pure ceramic and ceramic blended with metallic material is changed by introduction of ductile material. This increased the coating's cohesion and adhesion, as well as delayed the onset of visible damage onset within the coating.

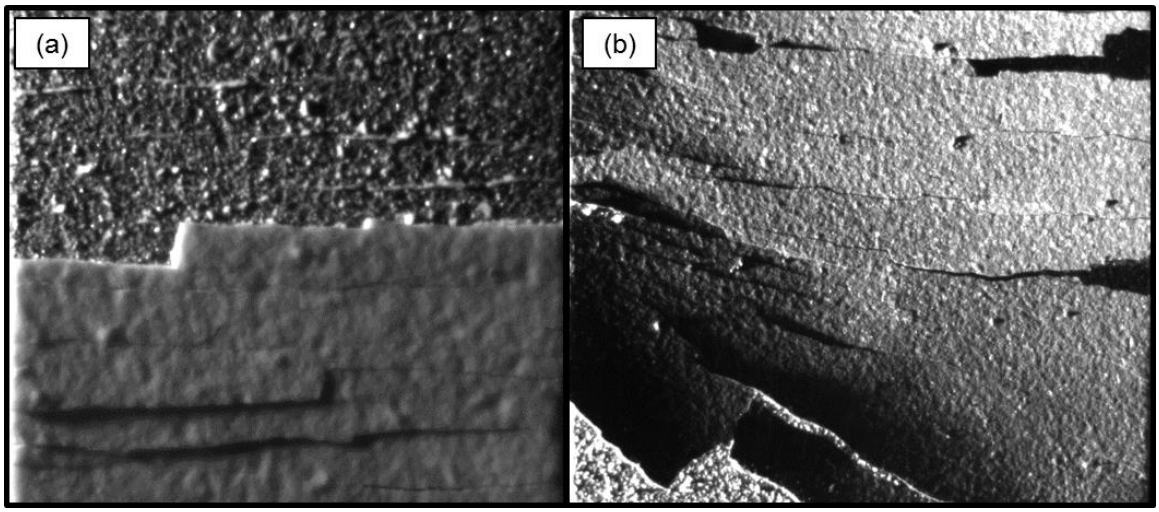

Figure 8-3 Cracking and delamination behavior of coatings on steel tensile samples. (a) HVOF deposited Alumina, showing brittle cracking and delamination. (b) HVOF Alumina-Nickel blended powder, showing increased coating cohesion and adhesion.

8.3 Dynamic Mechanical Testing: Fatigue

The role of TS coated specimens has been explored in this work and comes to a hypothesis that the dictating factors in the relative fatigue life will be dependent on the coating properties (stiffness, residual stress, etc.). The load bearing of the coating is thought to reduce the load experienced by the substrate until significant degradation of the coating shifts load back onto the substrate. The advancement of a coating crack directly into the substrate is not believed by the author to be a primary mechanism in the fatigue failure of TS coated specimens. Instead, it is the loss of load bearing due to coating crack growth that allows for greater fatigue damage to incur nearby in the substrate. The confirmation of this hypothesis would require in-situ monitoring of fatigue crack growth among an assortment of coating and substrate materials, with different mechanical properties and residual stress.

With the general principles of fatigue behavior of TS coated specimen described on the basis of coating properties and residual stress, the manipulation of coating processing leaves a great deal of flexibility for coating design. Among those possibilities include the ability to construct a multi-layered or functionally graded coating architecture. Such benefits of a graded or multi-layer microstructure include the ability to varying the stiffness and therefore the applied stress profile throughout a coated component. The tailoring of residual stress by multi-layer processing would also allow a designer to similarly manipulate the superimposed stress profile across a component experiencing cyclic loading. Consideration of surface functionality must also be considered, as a wear or corrosion protective surface is often the primary need for a TS coating. Such multi-layer examples include the use of a softer metallic bond coat that could enhance coating adhesion or reduce galvanic coupling, while allowing the top surface of the coating architecture to be a harder layer for wear resistance. The fatigue behavior of such multi or graded layer TS coatings are largely unexplored, though the surface functionality has seen considerable interest in past [83].

With fatigue behavior of a coated component considering the coating and substrate as a system, the sensitivity of a substrate to the coating process is also a critical factor, where particular engineering alloys are often specifically heat treated or tempered for their performance. The changes to the substrate due to coating processing and the thermal effects that coincide with it will vary from material to material, thus requiring future study based upon application needs. Such an example was the fatigue work presented on Ti64 in Section 5.3.3, where it is likely that the grit blasting of the substrate decreased the fatigue resistance of the material. Optimizing surface preparation for titanium alloys for TS coating application is an important subject, where TS coatings have opportunity to protect the surface of high strength-to-

weight ratios titanium alloys and thus enable their insertion into service where the surface properties of uncoated titanium are of concern.

9 References

[1] S. Sampath, R. Gansert, H. Herman, Plasma-spray forming ceramics and layered composites, JOM, 47 (1995) 30-33.
[2] C. Hackett, G. Settles, J. Miller, On the gas dynamics of HVOF thermal sprays, J Therm Spray Techn, 3 (1994) 299-304.
[3] H. Assadi, F. Gärtner, T. Stoltenhoff, H. Kreye, Bonding mechanism in cold gas spraying, Acta Mater, 51 (2003) 4379-4394.
[4] S. Kuroda, Y. Tashiro, H. Yumoto, S. Taira, H. Fukanuma, S. Tobe, Peening action and residual stresses in high-velocity oxygen fuel thermal spraying of 316L stainless steel, J Therm Spray Techn, 10 (2001) 367-374.
[5] T.C. Totemeier, J. Wright, Residual stress determination in thermally sprayed coatings—a comparison of curvature models and X-ray techniques, Surface and Coatings Technology, 200 (2006) 3955-3962.
[6] G.G. Stoney, The tension of metallic films deposited by electrolysis, Proceedings of the Royal Society of London. Series A, Containing Papers of a Mathematical and Physical Character, 82 (1909) 172-175.
[7] S. Kuroda, T. Fukushima, S. Kitahara, Simultaneous Measurement of Coating Thickness and Deposition Stress during Thermal Spraying, Thin Solid Films, 164 (1988) 157-163.
[8] Y.C. Tsui, T.W. Clyne, An analytical model for predicting residual stresses in progressively deposited coatings .1. Planar geometry, Thin Solid Films, 306 (1997) 23-33.
[9] J. Matejicek, S. Sampath, In situ measurement of residual stresses and elastic moduli in thermal sprayed coatings - Part 1: apparatus and analysis, Acta Mater, 51 (2003) 863-872.
[10] J. Matejicek, S. Sampath, T. Gnaupel-Herold, H.J. Prask, Residual stress in sprayed Ni+5%Al coatings determined by neutron diffraction, Appl Phys a-Mater, 74 (2002) S1692-S1694.
[11] A. Valarezo, S. Sampath, An Integrated Assessment of Process-Microstructure-Property Relationships for Thermal-Sprayed NiCr Coatings, J Therm Spray Techn, 20 (2011) 1244-1258.
[12] J. Matejicek, S. Sampath, D. Gilmore, R. Neiser, In situ measurement of residual stresses and elastic moduli in thermal sprayed coatings - Part 2: processing effects on properties of Mo coatings, Acta Mater, 51 (2003) 873-885.
[13] T. Varis, T. Suhonen, A. Ghabchi, A. Valarezo, S. Sampath, X. Liu, S.-P. Hannula, Formation Mechanisms, Structure, and Properties of HVOF-Sprayed WC-CoCr Coatings: An Approach Toward Process Maps, J Therm Spray Techn, DOI 1-10.
[14] K. Shinoda, J. Colmenares-Angulo, A. Valarezo, S. Sampath, Effect of deposition rate on the stress evolution of plasma-sprayed yttria-stabilized zirconia, Journal of thermal spray technology, 21 (2012) 1224-1233.

[15] L. Prchlik, S. Sampath, Effect of the microstructure of thermally sprayed coatings on friction and wear response under lubricated and dry sliding conditions, Wear, 262 (2007) 11-23.
[16] S. Wayne, J. Baldoni, S.-T. Buljan, Abrasion and erosion of WC-Co with controlled microstructures, Tribology transactions, 33 (1990) 611-617.
[17] G. Bolelli, V. Cannillo, L. Lusvarghi, M. Montorsi, F.P. Mantini, M. Barletta, Microstructural and tribological comparison of HVOF-sprayed and post-treated M–Mo–Cr–Si (M= Co, Ni) alloy coatings, Wear, 263 (2007) 1397-1416.
[18] J. Picas, A. Forn, G. Matthäus, HVOF coatings as an alternative to hard chrome for pistons and valves, Wear, 261 (2006) 477-484.
[19] J. Murthy, B. Venkataraman, Abrasive wear behaviour of WC–CoCr and Cr 3 C 2–20 (NiCr) deposited by HVOF and detonation spray processes, Surface and Coatings Technology, 200 (2006) 2642-2652.
[20] Y. Liu, T.E. Fischer, A. Dent, Comparison of HVOF and plasma-sprayed alumina/titania coatings—microstructure, mechanical properties and abrasion behavior, Surface and Coatings Technology, 167 (2003) 68-76.
[21] S. Wayne, S. Sampath, Structure/property relationships in sintered and thermally sprayed WC-Co, J Therm Spray Techn, 1 (1992) 307-315.
[22] R.M.P. Rodriguez, R.S. Paredes, S.H. Wido, A. Calixto, Comparison of aluminum coatings deposited by flame spray and by electric arc spray, Surface and Coatings Technology, 202 (2007) 172-179.
[23] J. Kawakita, S. Kuroda, T. Fukushima, T. Kodama, Development of dense corrosion resistant coatings by an improved HVOF spraying process, Science and Technology of Advanced Materials, 4 (2003) 281-289.
[24] J. Kawakita, S. Kuroda, T. Fukushima, T. Kodama, Corrosion resistance of HVOF sprayed HastelloyC nickel base alloy in seawater, Corrosion science, 45 (2003) 2819-2835.
[25] T. Hanson, G. Settles, Particle temperature and velocity effects on the porosity and oxidation of an HVOF corrosion-control coating, J Therm Spray Techn, 12 (2003) 403-415.
[26] D. Zhang, S. Harris, D. McCartney, Microstructure formation and corrosion behaviour in HVOF-sprayed Inconel 625 coatings, Materials Science and Engineering: A, 344 (2003) 45-56.
[27] R. McGrann, D. Greving, J. Shadley, E. Rybicki, T. Kruecke, B. Bodger, The effect of coating residual stress on the fatigue life of thermal spray-coated steel and aluminum, Surface and Coatings Technology, 108 (1998) 59-64.
[28] A. Savarimuthu, H. Taber, I. Megat, J. Shadley, E. Rybicki, W. Cornell, W. Emery, D. Somerville, J. Nuse, Sliding wear behavior of tungsten carbide thermal spray coatings for replacement of chromium electroplate in aircraft applications, J Therm Spray Techn, 10 (2001) 502-510.
[29] J.R. Davis, Handbook of thermal spray technology, ASM international2004.
[30] R. Schwetzke, H. Kreye, Microstructure and properties of tungsten carbide coatings sprayed with various high-velocity oxygen fuel spray systems, J Therm Spray Techn, 8 (1999) 433-439.
[31] A. Vaidya, V. Srinivasan, T. Streibl, M. Friis, W. Chi, S. Sampath, Process maps for plasma spraying of yttria-stabilized zirconia: An integrated approach to design, optimization and reliability, Materials Science and Engineering: A, 497 (2008) 239-253.
[32] S. Sampath, V. Srinivasan, A. Valarezo, A. Vaidya, T. Streibl, Sensing, control, and in situ measurement of coating properties: an integrated approach toward establishing process-property correlations, J Therm Spray Techn, 18 (2009) 243-255.

[33] G. Taguchi, Introduction to quality engineering: designing quality into products and processes, 1986.
[34] J. Matejicek, S. Sampath, In situ measurement of residual stresses and elastic moduli in thermal sprayed coatings: Part 1: apparatus and analysis, Acta Mater, 51 (2003) 863-872.
[35] G. Dwivedi, T. Nakamura, S. Sampath, Determination of Thermal Spray Coating Property with Curvature Measurements, J Therm Spray Techn, 22 (2013) 1337-1347.
[36] W.C. Oliver, G.M. Pharr, An improved technique for determining hardness and elastic modulus using load and displacement sensing indentation experiments, Journal of materials research, 7 (1992) 1564-1583.
[37] S. Usmani, S. Sampath, D.L. Houck, D. Lee, Effect of carbide grain size on the sliding and abrasive wear behavior of thermally sprayed WC-Co coatings, Tribology transactions, 40 (1997) 470-478.
[38] J. Guilemany, J. De Paco, J. Miguel, J. Nutting, Characterization of the W2C Phase Formed During the High Velocity Oxygen Fuel Spraying of a WC+ 12 pct Co Powder, Metallurgical and Materials Transactions A, 30 (1999) 1913-1921.
[39] B. Kear, G. Skandan, R. Sadangi, Factors controlling decarburization in HVOF sprayed nano-WC/Co hardcoatings, Scripta Materialia, 44 (2001) 1703-1707.
[40] C.-J. Li, H. Yang, H. Li, Effect of gas conditions on HVOF flame and properties of WC-Co coatings, Materials and manufacturing processes, 14 (1999) 383-395.
[41] W. Zhang, S. Sampath, A universal method for representation of in-flight particle characteristics in thermal spray processes, J Therm Spray Techn, 18 (2009) 23-34.
[42] S. Sampath, X. Jiang, J. Matejicek, L. Prchlik, A. Kulkarni, A. Vaidya, Role of thermal spray processing method on the microstructure, residual stress and properties of coatings: an integrated study for Ni–5 wt.% Al bond coats, Materials Science and Engineering: A, 364 (2004) 216-231.
[43] C.-J. Li, G.-C. Ji, Y.-Y. Wang, K. Sonoya, Dominant effect of carbide rebounding on the carbon loss during high velocity oxy-fuel spraying of Cr 3 C 2–NiCr, Thin Solid Films, 419 (2002) 137-143.
[44] T. Sahraoui, N.-E. Fenineche, G. Montavon, C. Coddet, Structure and wear behaviour of HVOF sprayed Cr 3 C 2–NiCr and WC–Co coatings, Materials & design, 24 (2003) 309-313.
[45] S. Wirojanupatump, P. Shipway, D. McCartney, The influence of HVOF powder feedstock characteristics on the abrasive wear behaviour of Cr x C y–NiCr coatings, Wear, 249 (2001) 829-837.
[46] J. Matejicek, S. Sampath, Intrinsic residual stresses in single splats produced by thermal spray processes, Acta Mater, 49 (2001) 1993-1999.
[47] S. Sampath, X. Jiang, J. Matejicek, A. Leger, A. Vardelle, Substrate temperature effects on splat formation, microstructure development and properties of plasma sprayed coatings Part I: Case study for partially stabilized zirconia, Materials Science and Engineering: A, 272 (1999) 181-188.
[48] S. Kuroda, T. Dendo, S. Kitahara, Quenching stress in plasma sprayed coatings and its correlation with the deposit microstructure, Journal of Thermal Spray Technology, 4 (1995) 75-84.
[49] D. Zois, T. Wentz, R. Dey, S. Sampath, C. Weyant, Simplified model for description of HVOF NiCr coating properties through experimental design and diagnostic measurements, J Therm Spray Techn, 22 (2013) 299-315.

[50] A. Kumar, J. Boy, R. Zatorski, L. Stephenson, Thermal spray and weld repair alloys for the repair of cavitation damage in turbines and pumps: a technical note, J Therm Spray Techn, 14 (2005) 177-182.
[51] J. Santa, L. Espitia, J. Blanco, S. Romo, A. Toro, Slurry and cavitation erosion resistance of thermal spray coatings, Wear, 267 (2009) 160-167.
[52] M. Thorpe, H. Richter, A pragmatic analysis and comparison of HVOF processes, J Therm Spray Techn, 1 (1992) 161-170.
[53] R.C. Dykhuizen, M.F. Smith, D.L. Gilmore, R.A. Neiser, X. Jiang, S. Sampath, Impact of high velocity cold spray particles, J Therm Spray Techn, 8 (1999) 559-564.
[54] A. Verstak, V. Baranovski, Activated combustion HVAF coatings for protection against wear and high temperature corrosion, Thermal Spray 2003: Advancing the Science and Applying the Technology, DOI (2003) 5-8.
[55] W.B. Choi, L. Li, V. Luzin, R. Neiser, T. Gnaupel-Herold, H.J. Prask, S. Sampath, A. Gouldstone, Integrated characterization of cold sprayed aluminum coatings, Acta Mater, 55 (2007) 857-866.
[56] S. Kuroda, M. Watanabe, K. Kim, H. Katanoda, Current status and future prospects of warm spray technology, J Therm Spray Techn, 20 (2011) 653-676.
[57] J. Kawakita, T. Fukushima, S. Kuroda, T. Kodama, Corrosion behaviour of HVOF sprayed SUS316L stainless steel in seawater, Corrosion science, 44 (2002) 2561-2581.
[58] P.D. Eason, J.A. Fewkes, S.C. Kennett, T.J. Eden, K. Tello, M.J. Kaufman, M. Tiryakioğlu, On the characterization of bulk copper produced by cold gas dynamic spray processing in as fabricated and annealed conditions, Materials Science and Engineering: A, 528 (2011) 8174-8178.
[59] M.B. Beardsley, J.L. Sebright, Structurally Integrated Coatings for Wear and Corrosion, 2008, pp. Medium: ED; Size: 10.14Mb, 129 pages.
[60] C. Weyant, S. Sampath, Engineered Thermal Spray Coatings for Bridge Repair and Reclamation, Adv Mater Process, 169 (2011) 64-65.
[61] M. Jackson, J. Rairden, J. Smith, R. Smith, Production of metallurgical structures by rapid solidification plasma deposition, JOM, 33 (1981) 23-27.
[62] K. Murakami, H. Asako, T. Okamoto, Y. Miyamoto, Microstructure and mechanical properties of rapidly solidified deposited layers of Fe・ C・ Cr alloys produced by low pressure plasma spraying, Materials Science and Engineering: A, 123 (1990) 261-270.
[63] R. Tiwari, S. Sampath, B. Gudmundsson, G. Halada, C. Clayton, H. Herman, Microstructure and tensile properties of L1< sub> 2</sub>—Type Ni・ Cr・ Al alloy prepared by vacuum plasma spray forming, Scripta metallurgica et materialia, 33 (1995) 1159-1162.
[64] A. Valarezo, W.B. Choi, W.G. Chi, A. Gouldstone, S. Sampath, Process Control and Characterization of NiCr Coatings by HVOF-DJ2700 System: A Process Map Approach, J Therm Spray Techn, 19 (2010) 852-865.
[65] G. Dwivedi, T. Wentz, S. Sampath, T. Nakamura, Assessing Process and Coating Reliability Through Monitoring of Process and Design Relevant Coating Properties, J Therm Spray Techn, 19 (2010) 695-712.
[66] W.B. Choi, L. Prchlik, S. Sampath, A. Gouldstone, Indentation of Metallic and Cermet Thermal Spray Coatings, J Therm Spray Techn, 18 (2009) 58-64.
[67] S. Sampath, H. Herman, Rapid solidification and microstructure development during plasma spray deposition, J Therm Spray Techn, 5 (1996) 445-456.

[68] P. Paris, F. Erdogan, A critical analysis of crack propagation laws, Journal of Fluids Engineering, 85 (1963) 528-533.
[69] S. Kikuchi, Y. Nakahara, J. Komotori, Fatigue properties of gas nitrided austenitic stainless steel pre-treated with fine particle peening, International Journal of Fatigue, 32 (2010) 403-410.
[70] M. Torres, H. Voorwald, An evaluation of shot peening, residual stress and stress relaxation on the fatigue life of AISI 4340 steel, Int J Fatigue, 24 (2002) 877-886.
[71] J. Komotori, M. Shimizu, Y. Misaka, K. Kawasaki, Fatigue strength and fracture mechanism of steel modified by super-rapid induction heating and quenching, International journal of fatigue, 23 (2001) 225-230.
[72] S. Hassani-Gangaraj, A. Moridi, M. Guagliano, A. Ghidini, M. Boniardi, The effect of nitriding, severe shot peening and their combination on the fatigue behavior and micro-structure of a low-alloy steel, International Journal of Fatigue, 62 (2014) 67-76.
[73] G. Hammersley, L.A. Hackel, F. Harris, Surface prestressing to improve fatigue strength of components by laser shot peening, Optics and Lasers in Engineering, 34 (2000) 327-337.
[74] G. Farrahi, J. Lebrijn, D. Couratin, Effect of shot peening on residual stress and fatigue life of a spring steel, Fatigue & Fracture of Engineering Materials & Structures, 18 (1995) 211-220.
[75] T. Varis, T. Suhonen, A. Ghabchi, A. Valarezo, S. Sampath, X. Liu, S.-P. Hannula, Formation Mechanisms, Structure, and Properties of HVOF-Sprayed WC-CoCr Coatings: An Approach Toward Process Maps, Journal of Thermal Spray Technology, 23 (2014) 1009-1018.
[76] R. Menini, N.B. Salah, R. Nciri, Stripping methods studies for HVOF WC-10Co-4Cr coating removal, Journal of materials engineering and performance, 13 (2004) 185-194.
[77] B.D. Sartwell, K.O. Legg, J. Schell, J. Sauer, P. Natishan, Validation of HVOF WC/Co thermal spray coatings as a replacement for hard chrome plating on aircraft landing gear, DTIC Document, 2004.
[78] W.S. Owen, M. Grujicic, Strain aging of austenitic Hadfield manganese steel, Acta Mater, 47 (1998) 111-126.
[79] F.C. Campbell, Elements of metallurgy and engineering alloys, ASM International2008.
[80] Y. Tsui, T. Clyne, An analytical model for predicting residual stresses in progressively deposited coatings Part 2: Cylindrical geometry, Thin Solid Films, 306 (1997) 34-51.
[81] S. Suresh, Y. Sugimura, E. Tschegg, The growth of a fatigue crack approaching a perpendicularly-oriented, bimaterial interface, Scripta metallurgica et materialia, 27 (1992) 1189-1194.
[82] G. Campoli, M. Borleffs, S.A. Yavari, R. Wauthle, H. Weinans, A.A. Zadpoor, Mechanical properties of open-cell metallic biomaterials manufactured using additive manufacturing, Materials & Design, 49 (2013) 957-965.
[83] G. Bolelli, V. Cannillo, L. Lusvarghi, R. Rosa, A. Valarezo, W.B. Choi, R. Dey, C. Weyant, S. Sampath, Functionally graded WC–Co/NiAl HVOF coatings for damage tolerance, wear and corrosion protection, Surface and Coatings Technology, 206 (2012) 2585-2601.

10 Appendix

10.1 Extended Micrographs of Coatings from 3.3.1

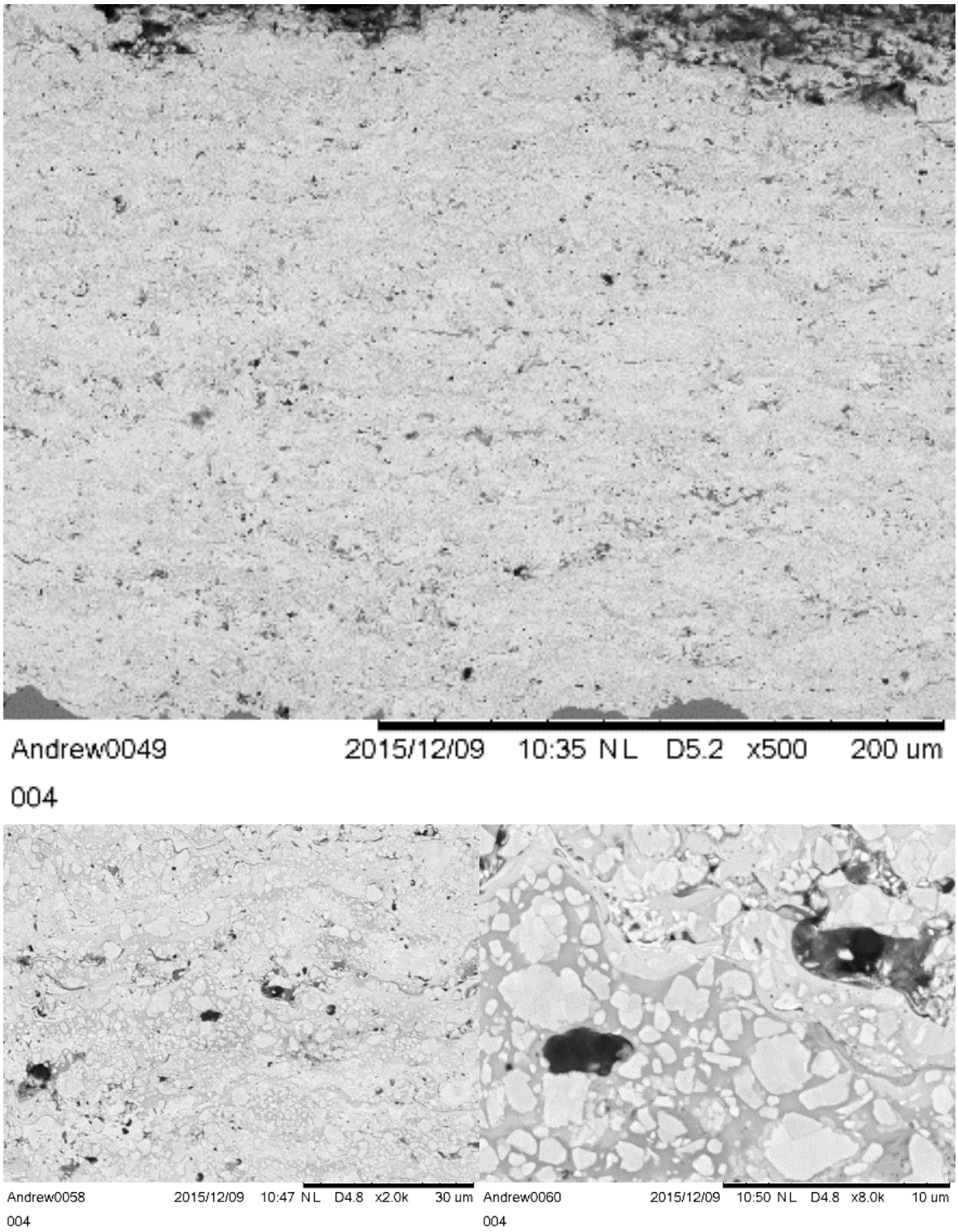

Figure 10-1 Coating D1

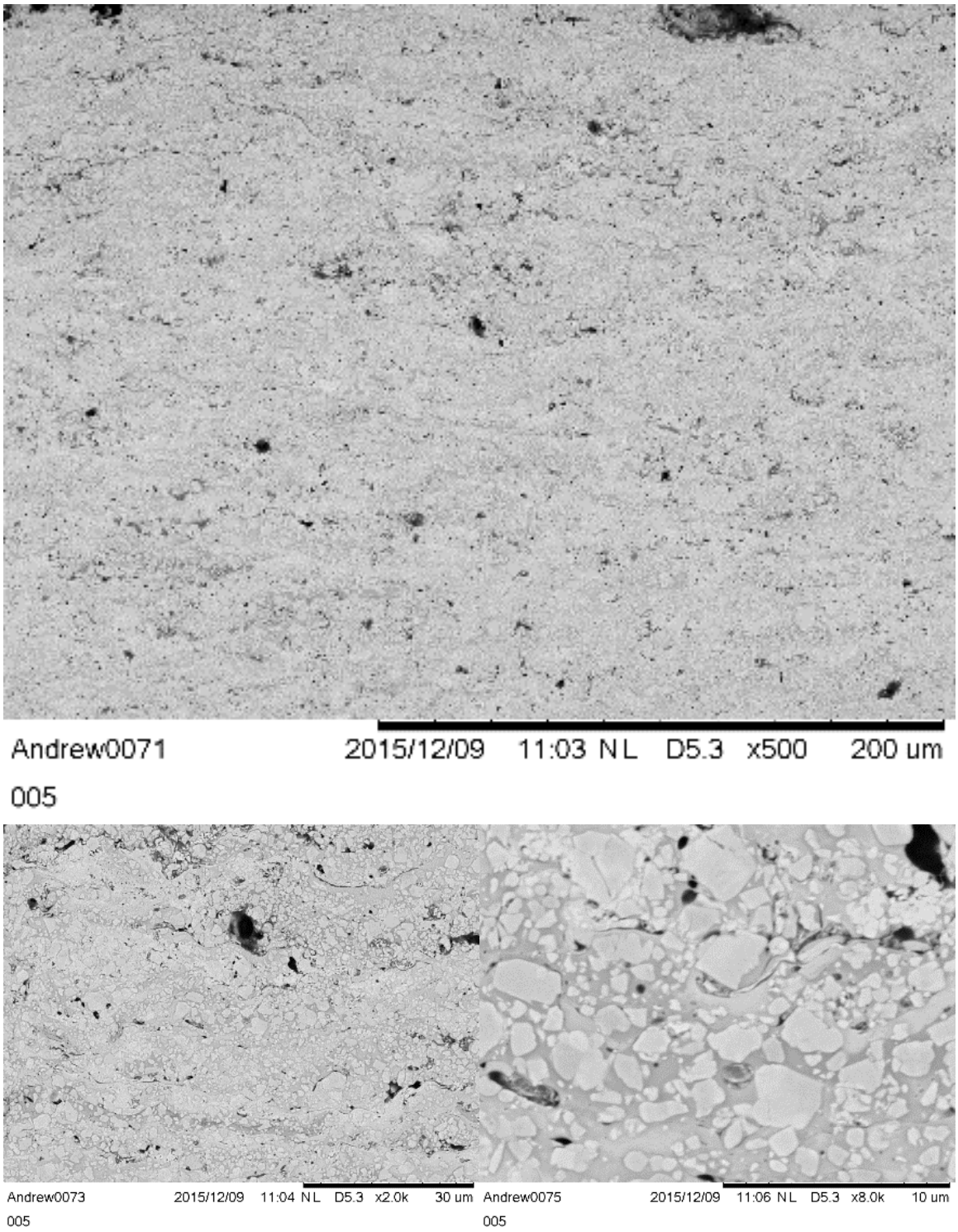

Figure 10-2 Coating D2

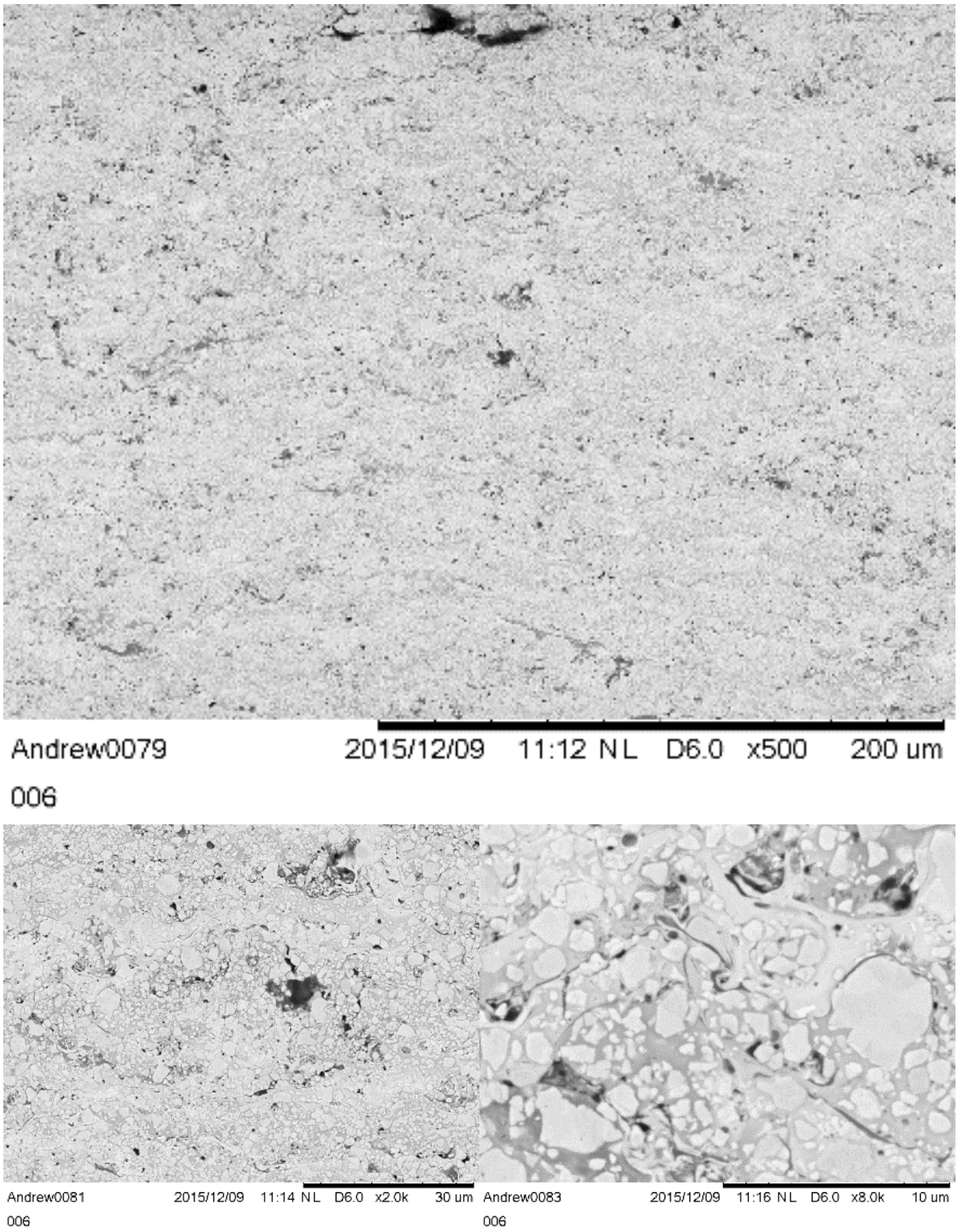

Figure 10-3 Coating D3

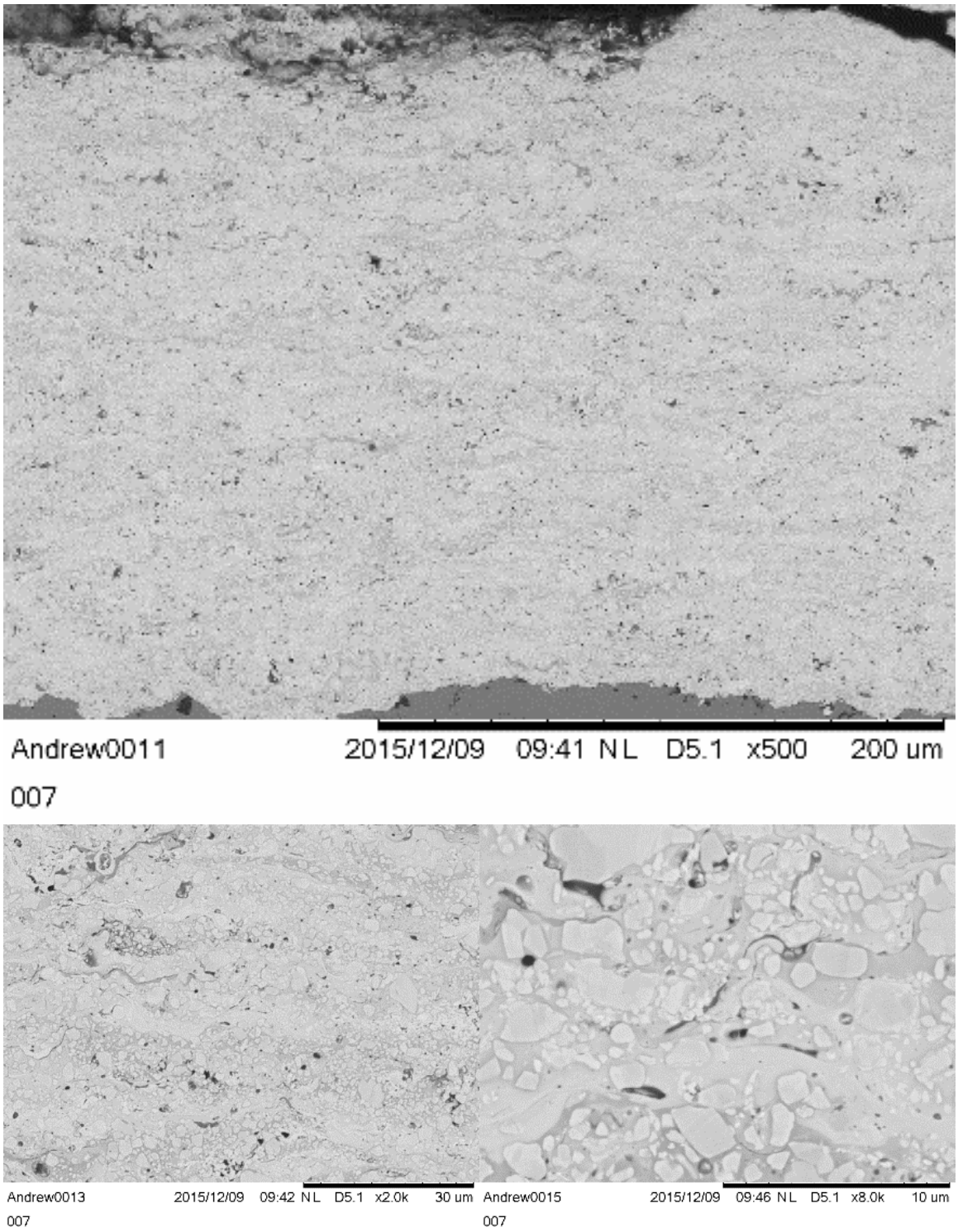

Figure 10-4 Coating D4

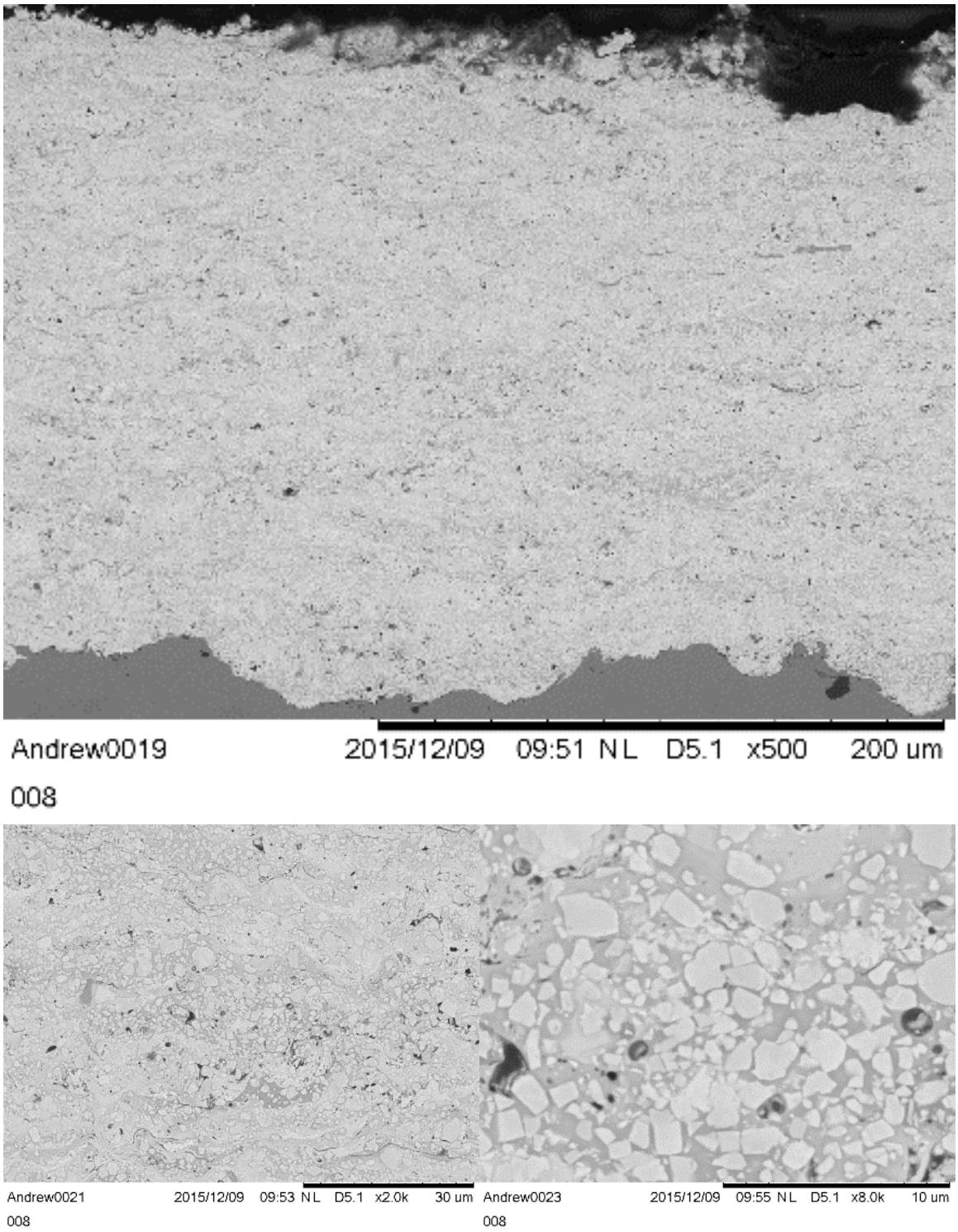

Figure 10-5 Coating D5

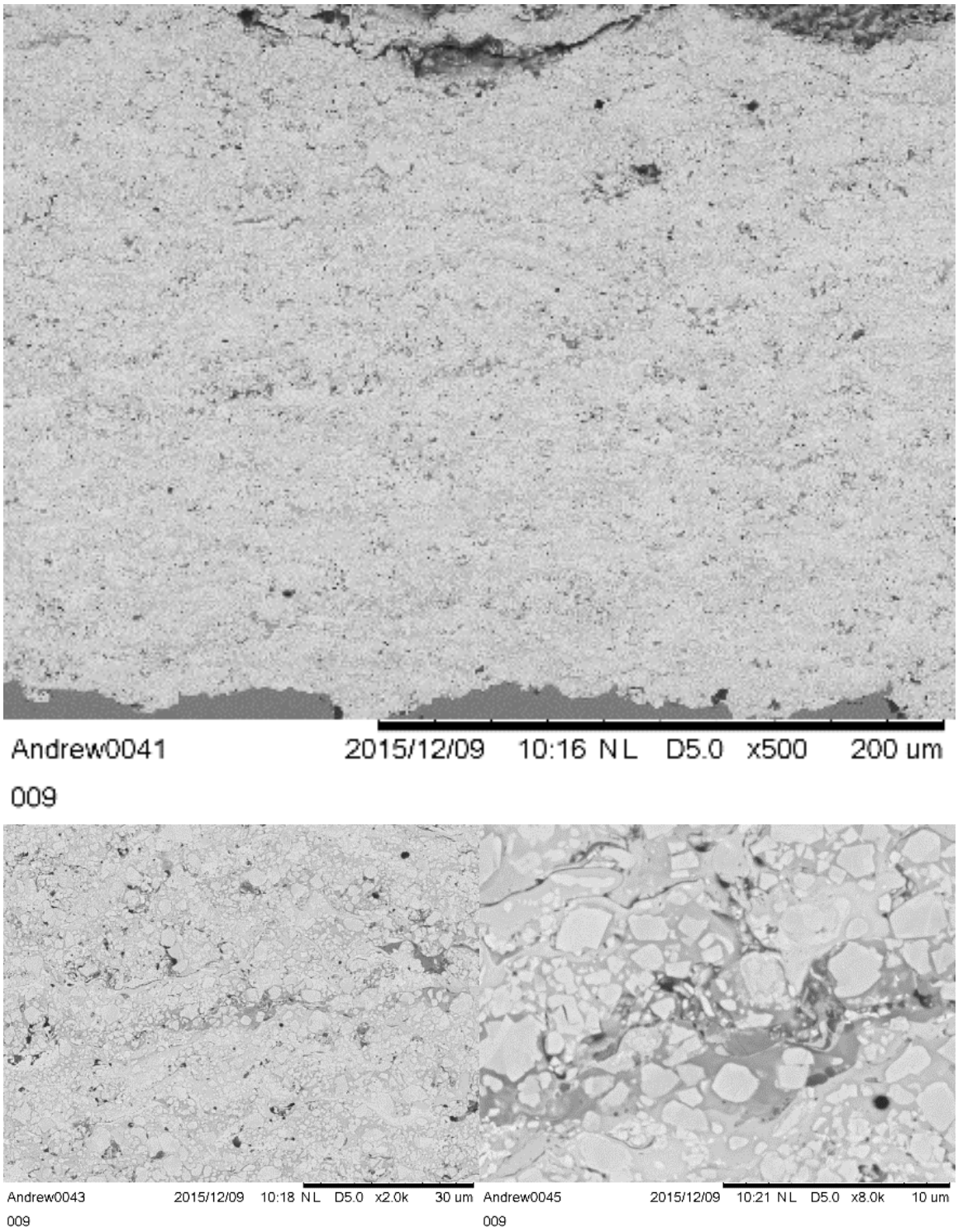

Figure 10-6 Coating D6

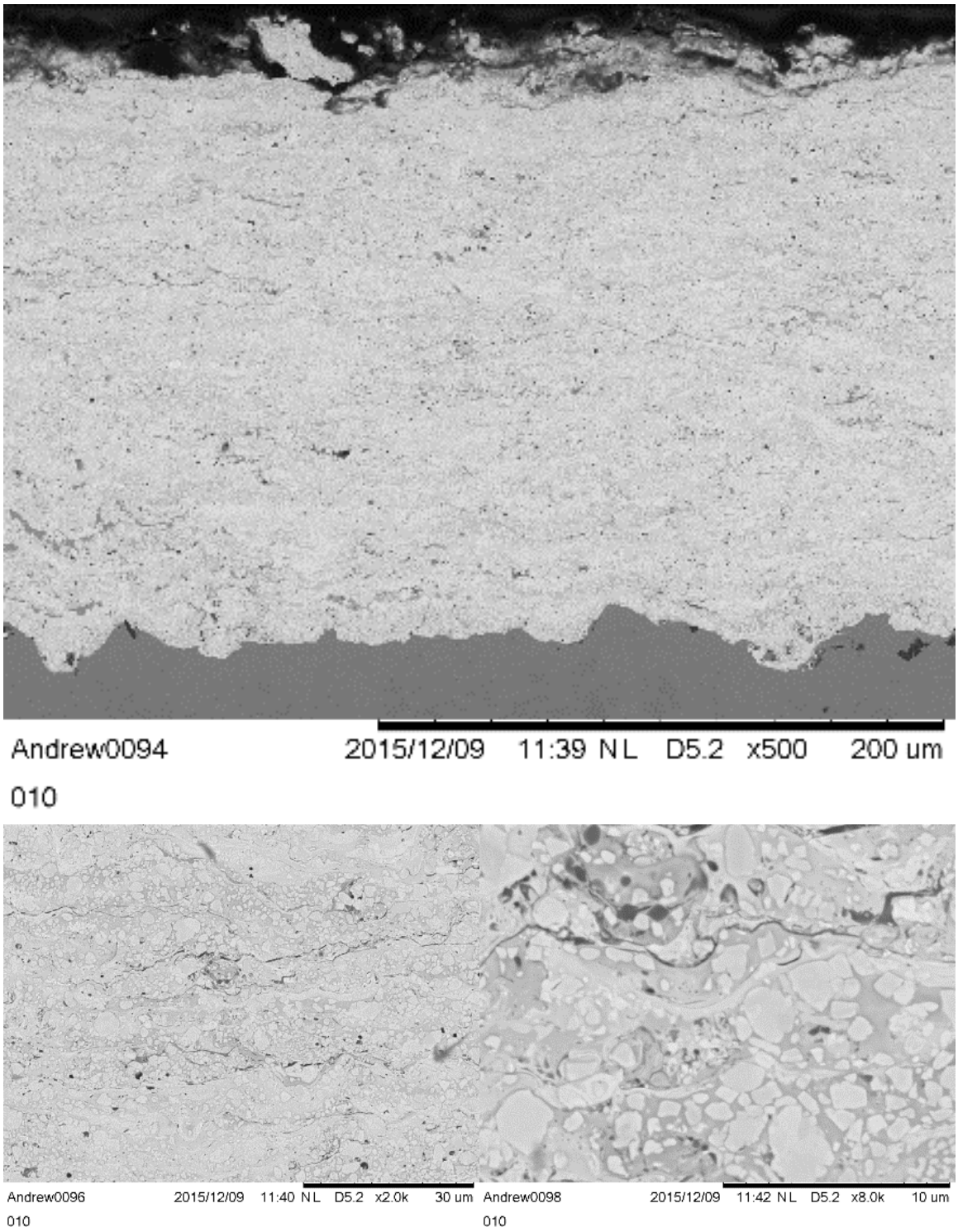

Figure 10-7 Coating D7

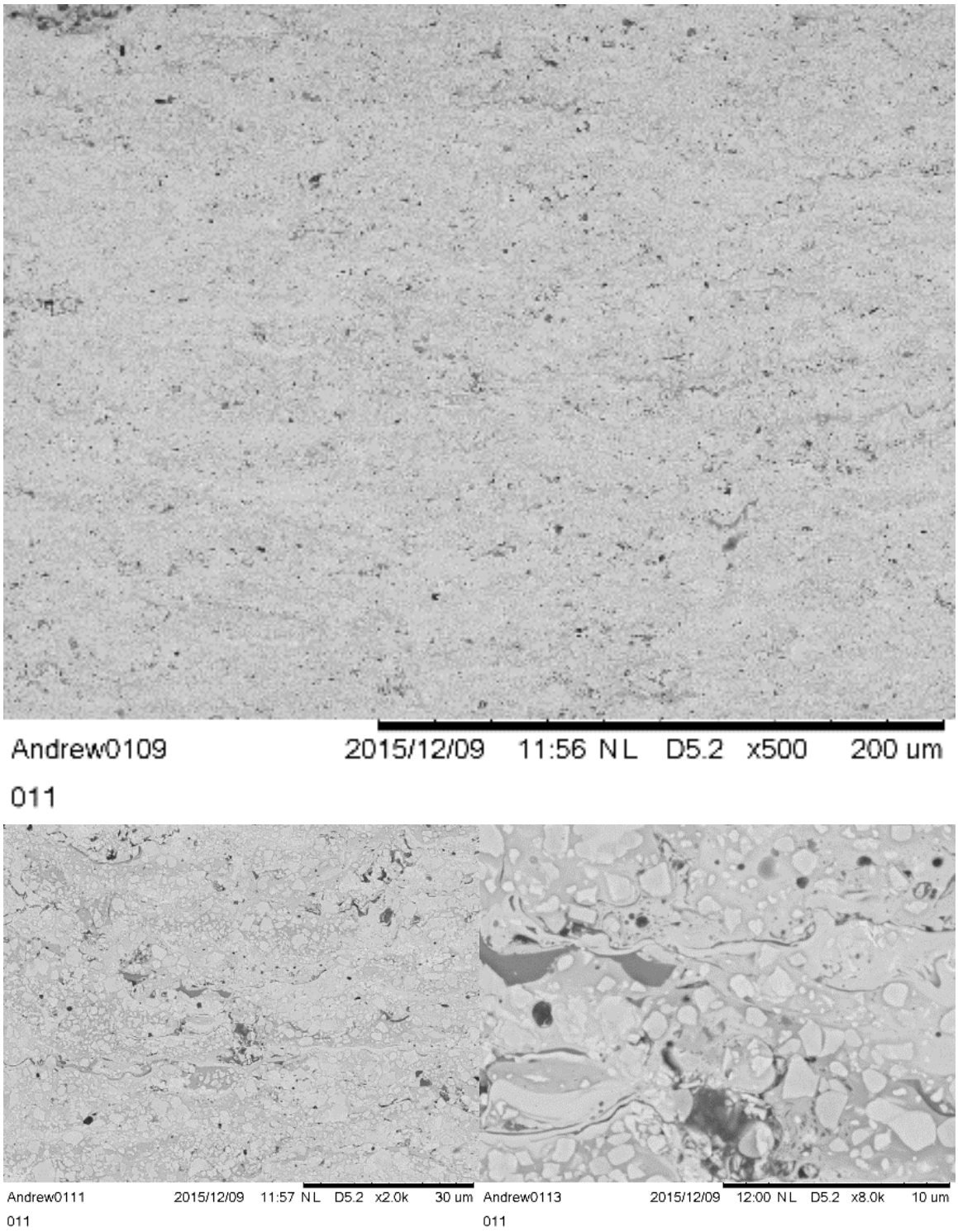

Figure 10-8 Coating D8

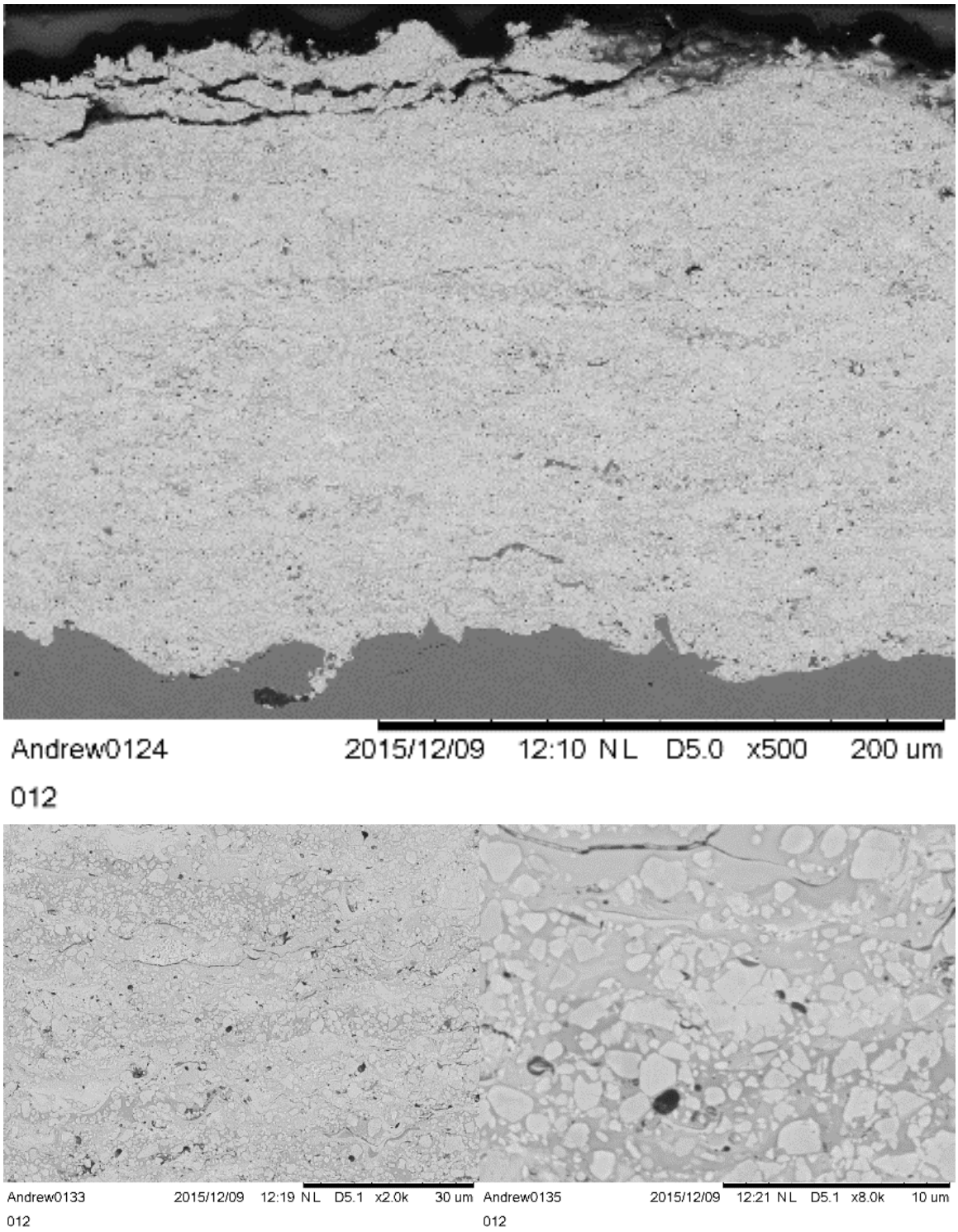

Figure 10-9 Coating D9

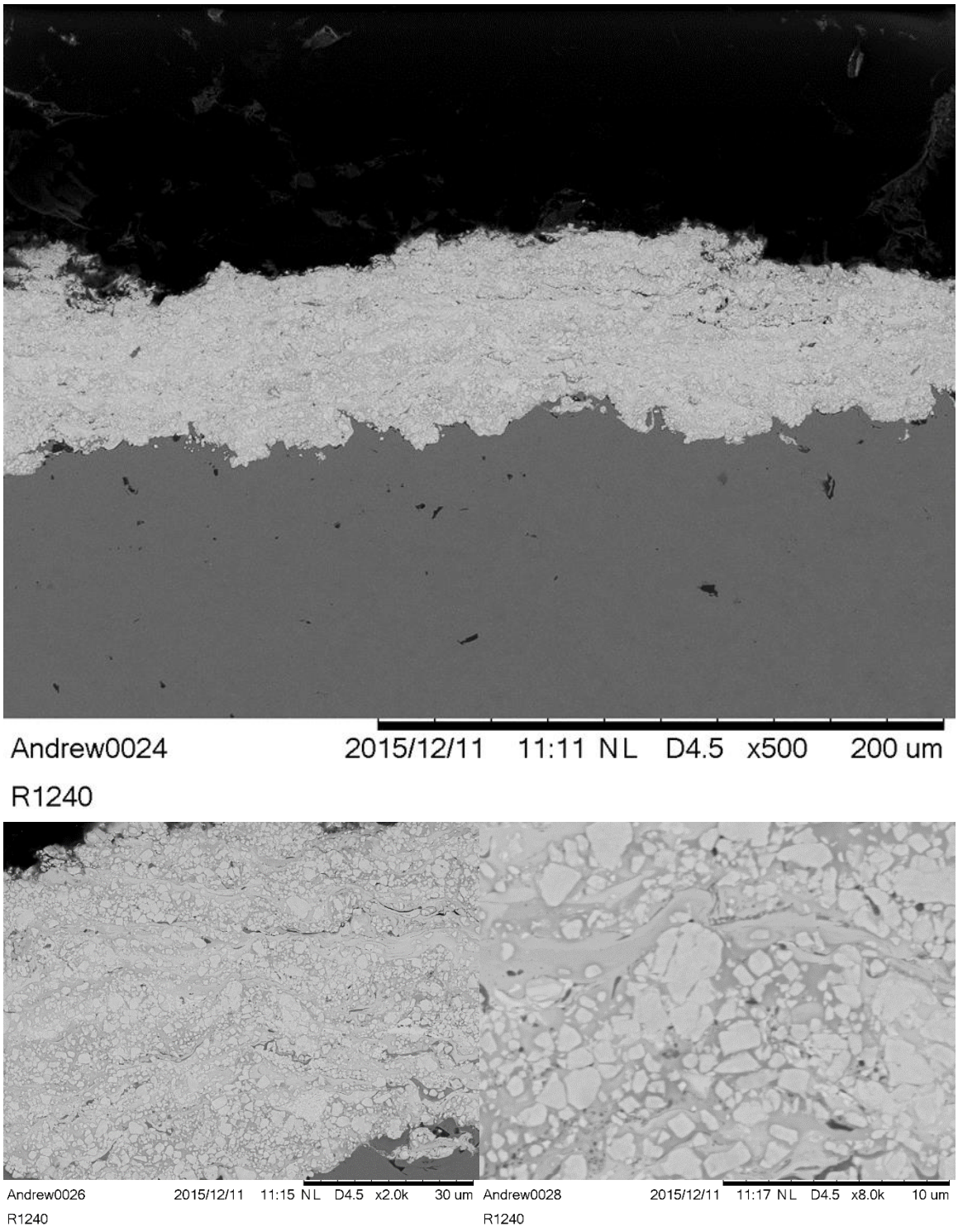

Figure 10-10 Coating J1

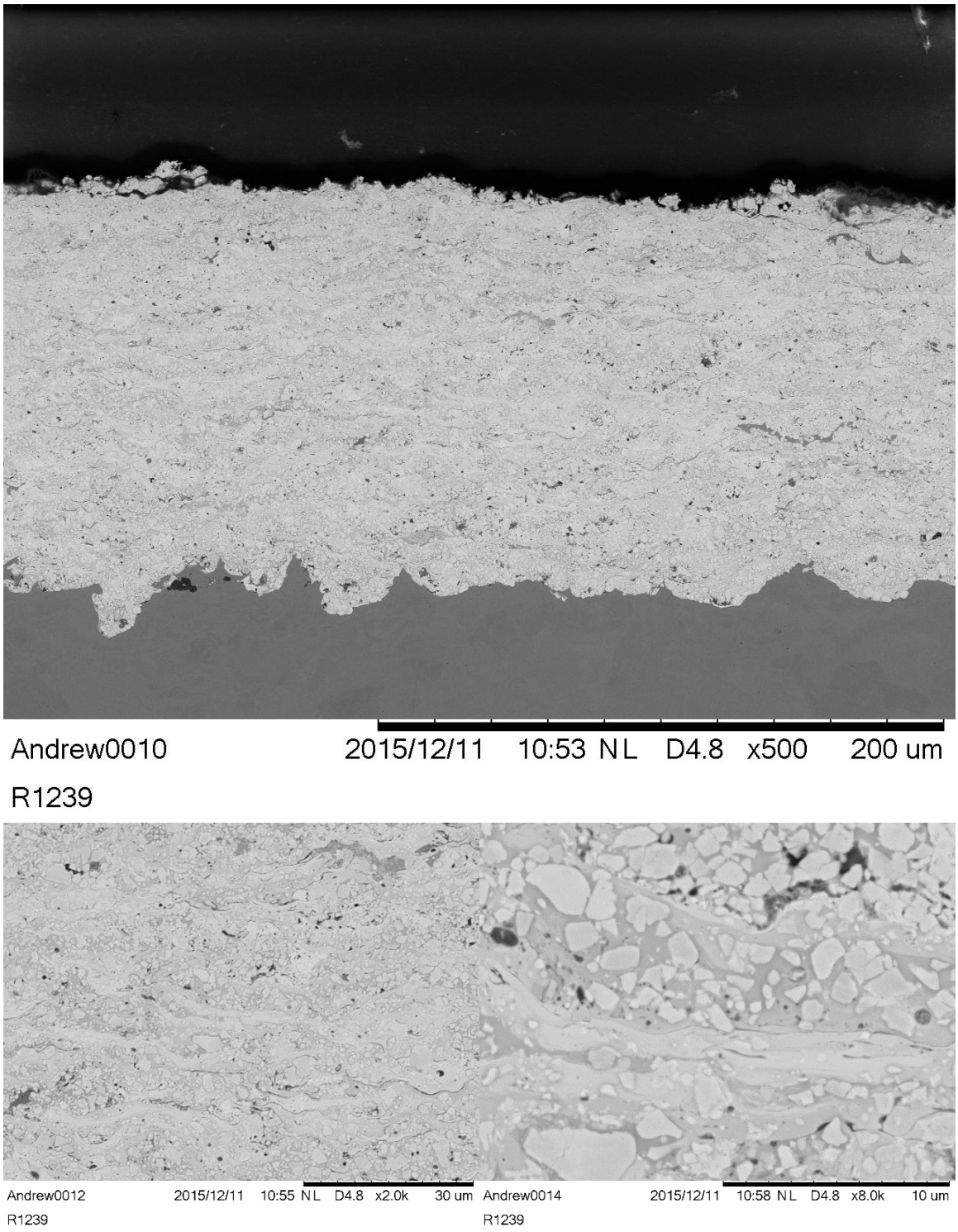

Figure 10-11 Coating J2

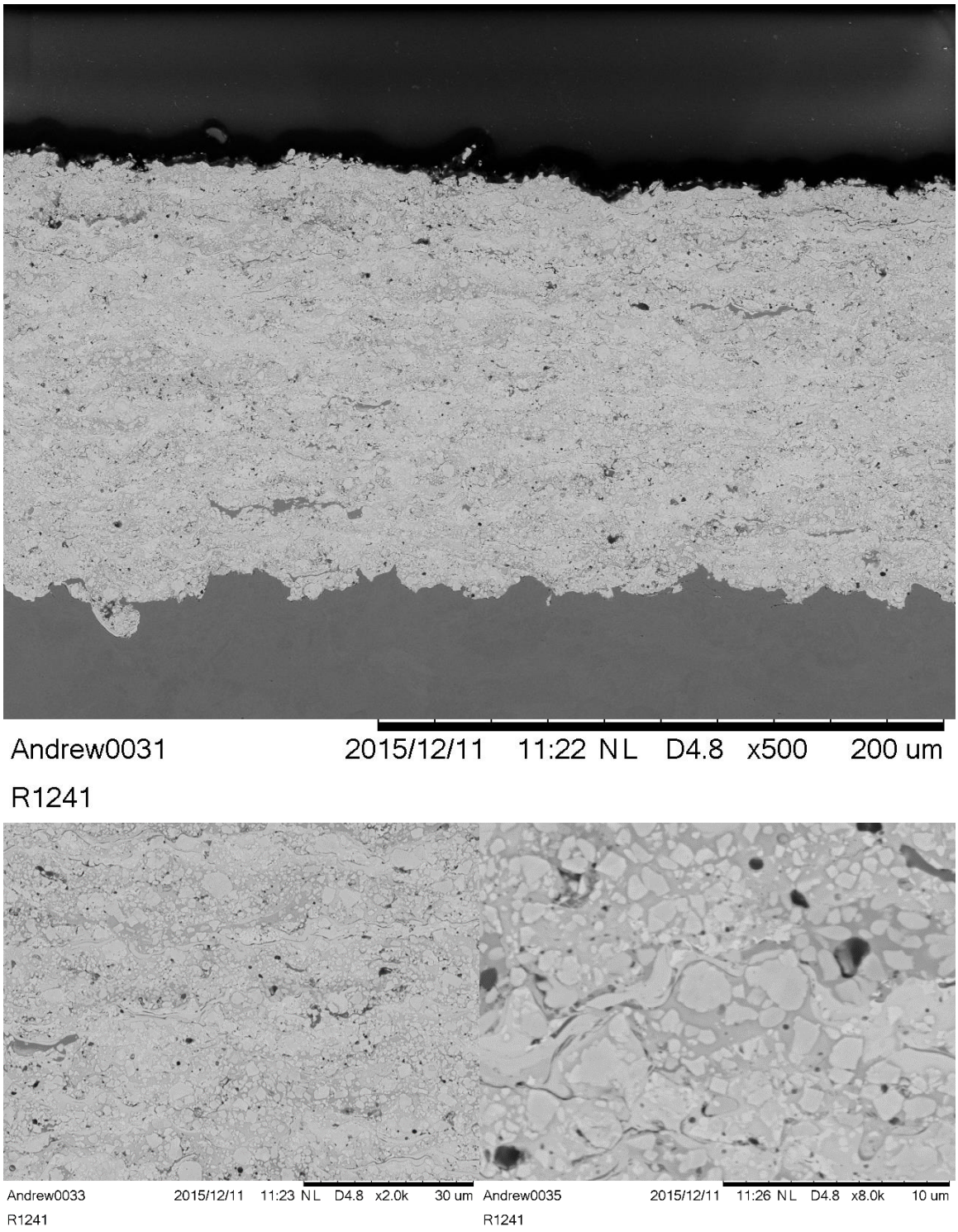

Figure 10-12 Coating J3

10.2 Stress Calculation from Beam Curvature Measurements

10.2.1 Formulas

As described in Section 3.2.4, the use of beam curvature measurement for calculation of coating residual stress was used for large portions of this work. The following is a demonstration of using curvature data measured from an in-situ measurement device to derive the deposition, thermal, residual, and evolving stress.

The Stoney formula, shown in Figure 10-13, is the basis for translation curvature to coating stress. It uses the change in curvature, modulus thickness and modulus, and the coating thickness. When incorporating the coating thickness and modulus into the stress computation, the Brenner-Senderoff formula in Figure 10-13 can be used for more accurate coating stress calculation

(a) *Stoney Formula*

$$\sigma_q = \frac{E'_S t_S^2}{6\Delta R \Delta t_D}$$

(b) *Brenner-Senderoff Formula*

$$\sigma_q = \frac{E'_S t_S (t_S + \beta^{5/4}\Delta t_D)}{6\Delta R \Delta t_D};\ \beta = \frac{E'_D}{E'_S}$$

Figure 10-13 (a) Stoney Formula and (b) Brenner-Senderoff Formula for coating stress measurements from beam curvature

The difference between the calculated values of the residual stress based on these two formula will depend on the thickness of the coating and substrate, as well as the in-plane moduli of the coating and the substrate. A ratio of the value of Brenner-Senderoff stress to Stoney stress is shown in Figure 10-14, indicating that as the coating to substrate thickness ratio and coating to substrate in-plane modulus increases, the differences in values between the two stress methods

increases. In general, a coating thickness of less than 10% of the substrate is used for stress calculations, keeping the error difference between the methods low

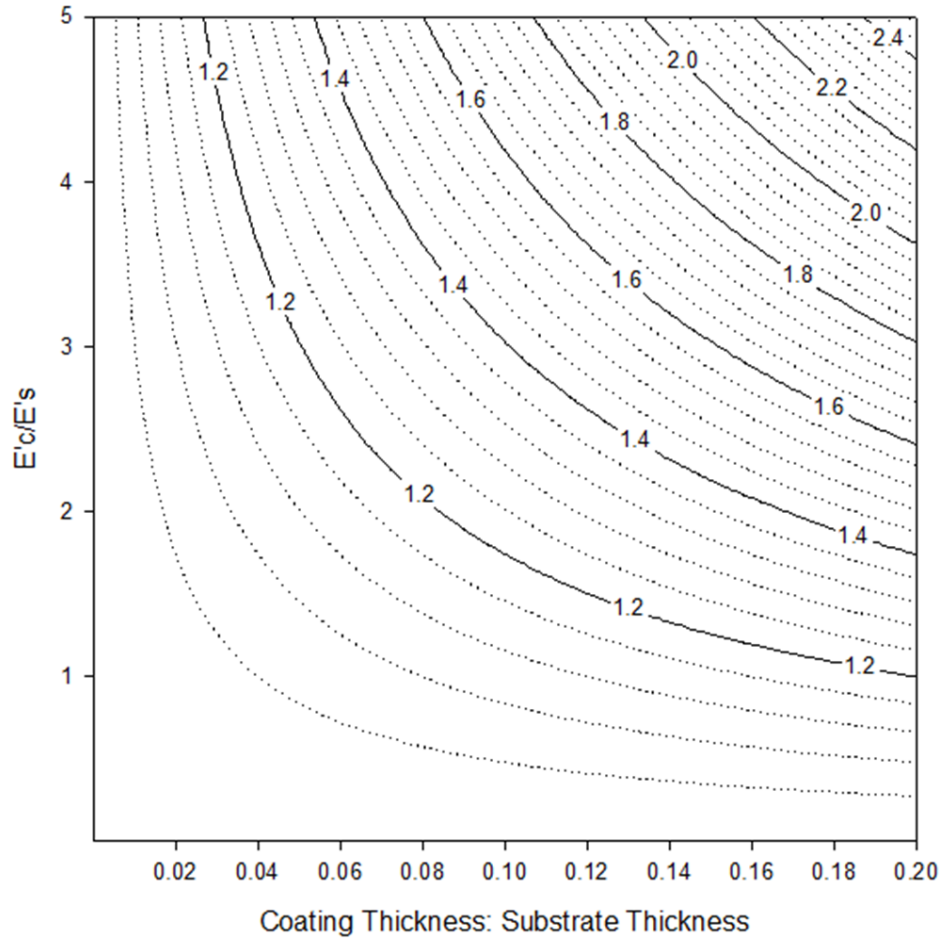

Figure 10-14 Ratio of Stoney Formula to Brenner-Senderoff Formula values of coating residual stress based on coating to substrate thickness ratio and coating to substrate in-plane modulus ratio

10.2.2 Data Example

A typical data output of curvature vs. temperature is shown in Figure 10-15, with the different regions of pre-heat, deposition, and cooling highlighted. The undulations in the curvature data is due to the pass by pass deposition as the torch rasters past the surface.

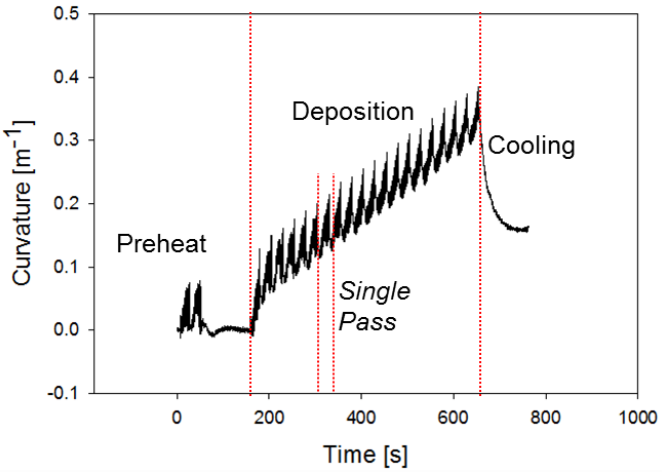

Figure 10-15 Typical curvature data measured by an in-situ beam curvature device, with preheating, deposition, and cooling captured. The undulations from a single coating pass is indicated.

Zooming in on a portion of the data, as shown in Figure 10-16, the individual coating strokes on the panel can be seen, as the spikes in curvature shown the deflection of the beam from the force of the plume. Pause time in-between the coating passes are also seen, where the curvature changes from the short period of cooling and where the difference in substrate and coating thermal expansion.

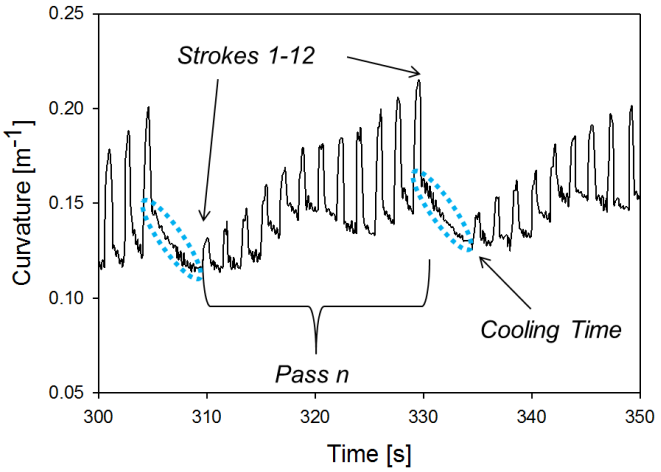

Figure 10-16 Highlighted curvature data of a single coating pass comprised of multiple restring strokes and cooling time in between the next coating pass

To determine the Deposition stress, the curvature measurements at the beginning of spraying and the end of spraying are used, as shown in Figure 10-17, along with the respective coating and substrate thickness. Thickness of the substrate is measured prior to coating deposition, followed by a measurement of the substrate with the coating in order to determine the thickness of the coating. Thermal stress is calculated in a similar manner, with the difference in curvature between the end of cooling and the end of spraying used with the coating and substrate dimensions

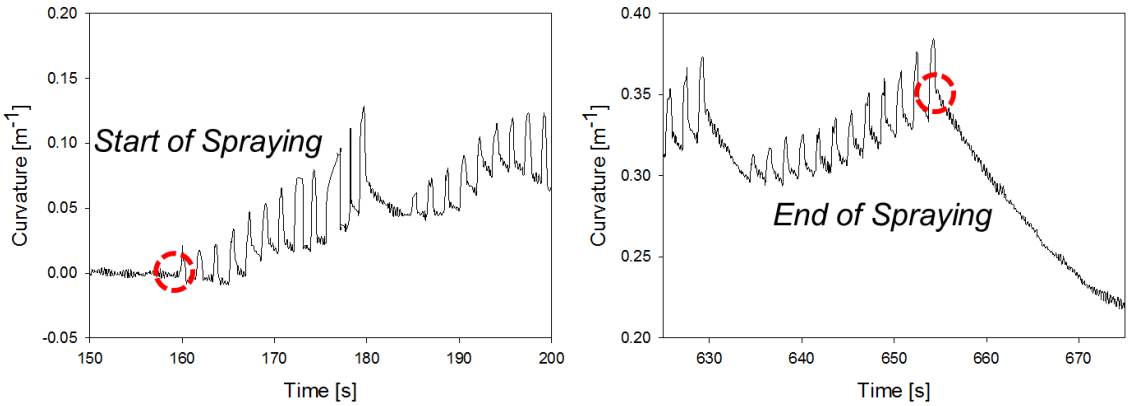

Figure 10-17 Curvature data with start of spraying and end of spraying points highlighted

Measurement of the Evolving stress is a slight adaptation of the Stoney formula, where instead of the total curvature change with the coating thickness used to calculate deposition stress, the steady state slope of curvature change with continuous coating thickness addition is used. In order to calculate Evolving stress, two curvature points that represent the linear chance in curvature with time are chosen, as shown in Figure 10-18. The first few coatings passes are excluded from this measurement to ensure a steady state deposition temperature has been reached and that no first pass effects are considered for Evolving stress. The amount of curvature change accrued between these two selected curvature points has a corresponding time. This time of curvature accumulation is then related to the amount of coating thickness added during that time by using the time of coating deposition and total coating thickness.

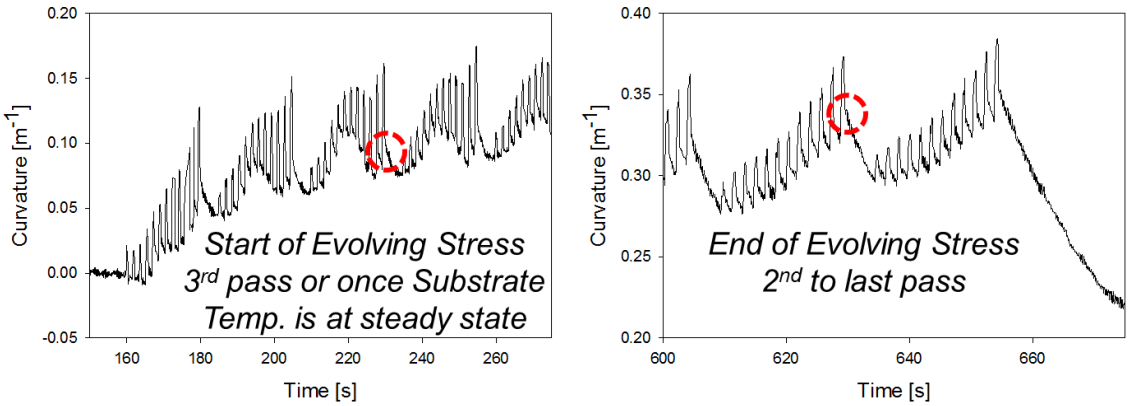

Figure 10-18 Curvature data indicating the points typically used for calculation of the evolving stress